BEILSTEIN JOURNAL OF NANOTECHNOLOGY

Chemical thin coating methods for functional nanomaterials

Edited by Mariona Coll, Julien Bachmann and David C. Cameron

Imprint

Beilstein Journal of Nanotechnology
www.bjnano.org
ISSN 2190-4286
Email: journals-support@beilstein-institut.de

The *Beilstein Journal of Nanotechnology* is published by the Beilstein-Institut zur Förderung der Chemischen Wissenschaften.

Beilstein-Institut zur Förderung der Chemischen Wissenschaften
Trakehner Straße 7–9
60487 Frankfurt am Main
Germany
www.beilstein-institut.de

BEILSTEIN JOURNAL OF NANOTECHNOLOGY

Block copolymers for designing nanostructured porous coatings

Roberto Nisticò

Review

Open Access

Address:
Department of Applied Science and Technology DISAT, Polytechnic of Torino, C.so Duca degli Abruzzi 24, 10129 Torino, Italy

Email:
Roberto Nisticò - roberto.nistico@polito.it

Keywords:
block copolymers; coatings; materials science; porous materials; self-assembly

Beilstein J. Nanotechnol. **2018,** *9,* 2332–2344.
doi:10.3762/bjnano.9.218

Received: 10 May 2018
Accepted: 08 August 2018
Published: 29 August 2018

This article is part of the thematic issue "Chemical thin coating methods for functional nanomaterials".

Guest Editor: J. Bachmann

Abstract

Highly ordered porous coatings find applications in many fields, such as nanotechnology, microfluidics and nanofluidics, membrane separation, and sensing. In recent years, there has been great interest regarding the synthesis of isoporous and well-ordered (in)organic coatings for the production of highly selective functional membranes. Among the different strategies that have been proposed to date for preparing these porous thin coatings, one simple route involves the use of self-assembled amphiphilic block copolymers either as the porogen (acting as sacrificial templating agents for the production of inorganic architectures) or as a source of the porogen (by self-assembly for the production of polymeric substrates). Therefore, an extended discussion around the exploitation of block copolymers is proposed here in this review, using polystyrene-*block*-polyethylene oxide (PS-*b*-PEO) as the model substrate, and critical points are highlighted.

Review

Introduction

Porous materials have received much attention because they can be successfully applied in many fields, such as nanotechnology, membrane separation, microfluidics and nanofluidics, sensing, catalysis, and biomedicine [1-5]. The manufacture of well-ordered devices at the nanometer level requires detailed control in terms of structural organization, thus introducing the concept of "matter manipulation" at the nanometer scale [6,7]. According to the literature, several methods have been proposed for the production of highly ordered porous nanostructured materials and/or coatings, which can be classified into one of the two classical routes: the bottom-up or the top-down approach [8-10]. In particular, a "top-down" approach relies on the exploitation of externally controlled parameters to build up a nanostructured architecture starting from larger dimensions

[11]. Conversely, a "bottom-up" approach involves the growth of (sub)nanometer components (i.e., colloids, (macro)molecules, or even atoms) to produce complex nanoarchitectures [12].

The fabrication of well-ordered nanostructured materials has developed considerably in recent years, thus becoming an immensely attractive (and multidisciplinary) field of research [13-20]. In particular, nanoscopic-ordered porous architectures in the form of thin films have received great attention in the field of membrane science and micro/nanofluidics, due to the high selectivity introduced without the loss of the mechanical properties (provided by the macroporous substrate) [21-25]. Interestingly, devices based on this technology have found commercial application in separation processes involving complex matrices, such as in the clarification of beverages (i.e., milk, beer, and juices) [26], or in the selective removal of bacteria in blood [27].

Porous polymeric coatings possess the advantages of high surface area materials with a well-defined porosity [28,29], easy processability (i.e., to form molded monoliths or thin films) [30-32], and the possibility of using different synthetic routes to facilitate the incorporation of multiple chemical functionalities into the porous framework or at the pore surface [33]. The self-assembly of block copolymers is an exceptional strategy for inducing well-ordered and regular porosity in polymers [6,32]. Block copolymers (BCs) are macromolecules consisting of two (or more) immiscible homopolymer chains covalently linked together. Mesoscale nanostructures can be obtained due to the thermodynamic incompatibility of the blocks, which induce microphase separation via self-assembly, in order to minimize the contact energy between the incompatible segments forming the BCs [34]. BCs can have two different roles in the preparation of nanostructured porous materials: either as templating agents [4,6,35] or as origin of the porous framework (exploiting their self-assembly capability) [36,37]. In particular, by varying the block copolymer parameters (mostly, molecular weight, and the different blocks volume fraction) and the formulation (i.e., solvent(s) volume), it is possible to modulate the surface layer organization at the level of a few tens of nanometers.

The following paragraphs describe how well-ordered (in)organic porous coatings and membranes are obtained due to the action of BCs either as templating agents or as the source of the porogen by self-assembly. In order to guide researchers in the field of highly organized porous coatings, a detailed discussion of both approaches is presented here. In this context, different BCs are available on the market (or are eventually synthesizable), opening an infinite number of possibilities. Some properties belong to BCs (considered as a general category), whereas others are strictly correlated to the blocks forming the polymeric chains (e.g., residual functionalities, reactivity). Since the scientific literature describing the properties of BCs is extremely vast, this review will only consider (and analyze in detail) the works and the technical discussion relevant for this review. Moreover, for simplicity, only the scientific literature describing polystyrene-*block*-polyethylene oxide (PS-*b*-PEO) systems is here considered, since the knowledge gained from the PS-*b*-PEO systems can be more generally applied (and mostly valid for the other subfamilies of BCs). Additionally, among the different BCs, PS-*b*-PEO systems are very attractive due to the presence of some particular functionalities forming the two blocks (namely, the hydroxy end groups from the PEO moieties), which make this class of BCs exploitable for further functionalization reactions [38].

Therefore, with the aim of highlighting the peculiar properties of BCs, PS-*b*-PEO systems are critically discussed in this review, with a particular emphasis on their capability of growing well-ordered nanostructured porous architectures and coatings, exploitable for designing smart membranes and other devices for next future advanced applications.

Block copolymer self-assembly: theory and application

The self-assembly of BCs represents an exceptional strategy for inducing well-ordered and regular porosity in polymeric structures. As already mentioned in the Introduction, BCs are macromolecules made of two (or more) blocks (i.e., series of monomeric units) of homopolymer chains, thermodynamically incompatible, linked together by covalent bonds. According to the self-consistent mean field (or SCMF) theory [39], it is possible to predict the nanoscopic domain structure (i.e., spherical, cylindrical, double gyroid, and lamellar) for an AB diblock copolymer (as reported in Figure 1A) [40-42]. As indicated in Figure 1B, by increasing the volume fraction, *f,* of one of the blocks, the microdomain arrangement changed from closely packed spheres (CPSs), to body centered cubic spheres (Q^{229}), to hexagonally packed cylinders (H), to bicontinuous gyroid (Q^{230}, which becomes unstable at high values of segregation power χN) and lamellae (L).

The principal driving factors governing the self-assembly of BC melts is the immiscibility of the two blocks (quantified by the Flory–Huggins interaction parameter χ) that drives the system to segregate as the temperature decreases (inversely proportional), giving an order–disorder transition at a certain value of χN [43]. In detail, the Flory–Huggins model relies on the thermodynamics of polymer solutions by considering the Gibbs free energy for mixing polymer with solvents. According to the Flory–Huggins theory, to calculate the Flory–Huggins interac-

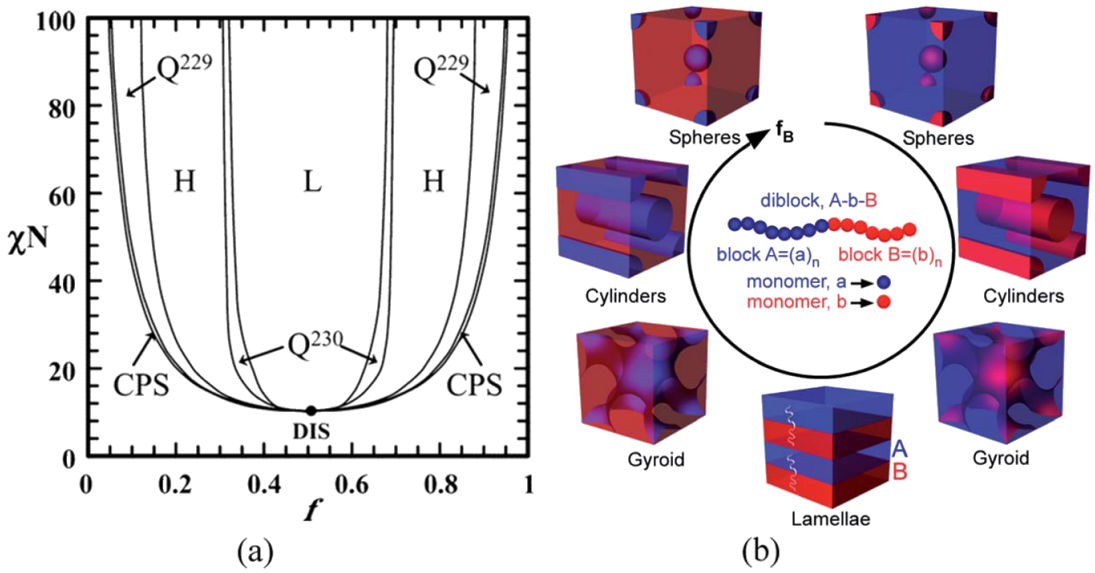

Figure 1: a) Phase diagram of diblock copolymer predicted by SCMF theory. Reprinted with permission from [41], copyright 2006 American Chemical Society. b) Various microdomain organization patterns of a linear AB diblock copolymers. Reprinted with permission from [42], copyright 2014 The Royal Society of Chemistry. *f*: volume fraction of one block; χ: Flory–Huggins interaction parameter; N: degree of polymerization; L: lamellae; H: hexagonally packed cylinders; Q^{230}: double-gyroid phase; Q^{229}: body centered spheres; CPS: closed-packed spheres; and DIS: disordered.

tion parameter, it must be considered that, in a binary system, both polymer and solvent are randomly distributed in the volume, and the heat of mixing is proportional to the volume fraction of polymer segments in the volume. Hence, the free energy minimization during microphase separation favors the formation of various thermodynamically stable structures on the nanometer length scale [44]. However, microphase separation can also be influenced by the presence of a more complex formulation due to the addition of a lower molecular weight component (such as additives and homopolymers) as well as a block-selective solvent [43,45].

Table 1 reports a survey of the principal BCs used for obtaining ordered porous architectures [45-79]. In general, all microdomain arrangements predicted by the SCMF theory, except CPSs, have been experimentally verified for many different BCs. The CPS phase, which is located between the disordered state (DIS) and Q^{229} phase, has not been observed experimentally for neat BCs formulations, but it has been verified for several BCs/solvent mixtures [49,80] and/or BCs/homopolymer formulations [81,82]. The microdomain arrangement is affected by heating, since BCs can exhibit phase mixing upon heating, due to the increase in the translational (or combinatorial) entropy and subsequent decrease of the phases interaction area. It can also exhibit phase separation as a result of the thermal expansion coefficients and/or directional enthalpy (or entropy) changes, as shown in [83]. Furthermore, crystallinity is also an important parameter that can influence the domain orientation. As reported by Register and co-workers [84], there are three different levels of orientation: i) the orientation of the polymer chains within the lamella crystals, ii) the orientation of the lamella crystals within the domain structure of the block copolymer, and iii) the domain structure itself. Additionally, it is also possible to rationalize the crystallization behavior in BCs considering the degree of miscibility of the components. This suggests that the microphase separation morphology is also affected by the composition of the blocks forming the BCs. Semicrystalline BCs give two different crystallization modes: break-out crystallization and confined crystallization (the last one typical when the crystalline block is the minor component); for a detailed discussion, please refer to [85]. In this context, BCs containing crystalline blocks (such as PE and PEO domains) show two different chain-folding orientations that give different domain-structure orientation: perpendicular folding, whose domains are perpendicularly oriented with respect to the lamellar layer, and parallel folding, with domains parallel with respect to the lamellar layer [86]. Perpendicular folding occurs when a low molecular weight BC crystallizes from a disordered phase (or from a poorly segregated phase). With increasing molecular weight, the interfacial area per block junction increases, inducing parallel folding (the most thermodynamically stable form) [87]. The removal of the sacrificial component (SC) to obtain the final polymeric porous material can be performed using various etching procedures, such as plasma oxidization [53], electron beam curing, as well as laser and/or selective decomposition (as reported in Table 1).

Table 1: Block copolymers (BCs), sacrificial components (SC), and the microstructures of the porous polymeric architectures.

BCs[a]	SC	etching conditions	microstructure	ref.
1,2-PB-*b*-PDMS	PDMS	tetrabutylammonium fluoride in THF	H	[46]
P2VP-*b*-PI, PI h.	PI	ozonolysis	Q^{230}	[47,48]
P3DDT-*b*-PLA	PLA	NaOH	H	[49]
(P3HT-NH_3^+)-*b*-(PS-SO_3^-)	PS-SO_3^-	acetate, triethylamine	n.d.	[50]
PFS-*b*-PLA	PLA	NaOH	H, Q^{230}	[51,52]
PI-*b*-PS, PI h., PS h.	PS h.	hexane	Q^{230}	[53]
PFS-*b*-PMMA	PMMA	UV radiation	Q^{230}	[54]
PE-*b*-PEP, PE h., PEP h.	PEP h.	THF	Q^{230}	[55]
PE-*b*-PS	PS	fuming HNO_3	H, Q^{230}	[56,57]
PLA-*b*-P(N-S)	PLA	NaOH	H	[58]
PS-*b*-PEO	PEO	HI or heating	H, Q^{230}	[59-63]
PS-*b*-PEO, resorcinol	resorcinol	2-propanol	H, Q^{230}	[45,64]
PS-*b*-PLA	PLA	NaOH or HI	H, Q^{230}	[65-69]
PS-*b*-PDMS	PS	O_2 plasma treatment	H	[70]
PS-*b*-PMMA	PMMA	UV radiation	H, Q^{230}	[71-74]
PS-*b*-PMMA, PMMA h.	PMMA h.	CH_3COOH	H	[75,76]
PSTPA-*b*-PLA	PLA	NaOH	H	[77]
PS(BCB)-*b*-PMMA	PMMA	UV radiation	H	[78]
PS(BCB)-*b*-PLA	PLA	NaOH	H	[79]

[a]h.: homopolymer; 1,2-PB: 1,2-poly(butadiene); P2VP: poly(2-vinylpyridine); P3DDT: poly(3-dodecylthiophene); P3HT-NH_3^+: aniline chain-end-functionalized poly(3-hexylthiophene); PDMS: poly(dimethylsiloxane); PE, poly(ethylene); PEO: poly(ethylene oxide); PEP: poly(ethylene-*alt*-propylene); PFS: poly(ferrocenylsilane); PI: poly(isoprene); PLA: poly(lactic acid); PMMA: poly(methyl methacrylate), P(N-S): poly(norbornenylethylstyrene-*s*-styrene); PS: poly(styrene); PS(BCB): poly(styrene-*r*-benzocyclobutene); PS-SO_3^-: sulfonic acid chain-end-functionalized poly(styrene); PSTPA: poly(styrene) containing triphenylamine side group.

Hozumi and co-workers [74] investigated the removal of poly(methyl methacrylate) (PMMA) domains in a PS-*b*-PMMA copolymer film by using 172 nm vacuum-ultraviolet (VUV) light. In this case, the selective etching of activated oxygen molecules generated by the VUV radiation towards the two blocks (PS and PMMA) allowed for the preferential decomposition of PMMA and the consequent formation of a PS nanoporous network. The modulation of the irradiation time and pressure caused chemical and physical modifications of the PS nanostructures, since the complete removal of PMMA phase produces a hydrophobic PS surface whereas an irradiation at a pressure of 103 Pa caused the partial decomposition of the PS matrix with the modification of the material pore size and structure.

By focusing on PS-*b*-PEO copolymers, Mao et al. [59] demonstrated that the chemical etching of the minority component leads to the formation of a well-ordered nanoporous system by selective removal of the PEO domains by simple ether cleavage by washing with aqueous hydrogen iodine. This strong acid was selected for its specific debonding reactivity toward the aliphatic ether functionalities forming the PEO chains [88]. Furthermore, they tried also to obtain a monolithic nanoporous material with nanochannels of ≈10 nm width [61]. Unfortunately, the extremely harsh conditions due to the aqueous hydrogen iodine make this solution difficult to apply in thin films or coatings. In the work of Zhang and co-workers [60], a specific PS-*b*-PEO copolymer containing a cleavable juncture (namely, triphenylmethyl (trityl) ether) between the two blocks PS and PEO was prepared. This solution guarantees that acids under mild conditions can easily cleave the linkage between the blocks without affecting the block's self-organization.

Based on almost the same principle, nanoporous thin films with well-ordered cylindrical pores were obtained by preparing metallo-supramolecular block copolymers (where the two different polymeric blocks are linked via metal–ligand complexes) [63]. In this particular case, the approach consists of firstly, the self-assembly of the metallo-supramolecular block copolymer, forming a well-ordered thin film, and secondly, the opening of the metallo-complex via redox reaction, extracting the PEO moieties. In this study, the metallo-complex selected is Ru(II)-terpyridine bis-complex. By washing the film with a Ce(IV)-containing acid solution, the Ru(II) complex between the blocks is oxidized into Ru(III) that is able to form only a monocomplex with the terpyridine ligands, thus breaking one metallo-organic bond. The aqueous environment favored the extraction of the freely accessible, soluble PEO and Ru-PEO moieties,

leaving both PS and Ru-PS moieties to form the nanoporous polymeric matrix.

It has been demonstrated that by controlling the annealing procedure and the humidity, it is possible to control the orientation of the PEO cylindrical domains within the PS thin film [89,90]. In particular, at high humidity conditions, it has been found that PEO cylindrical domains are vertically (perpendicular) oriented with respect to the thin film surface, whereas at low humidity conditions, the PEO domains are horizontally (parallel) oriented [90].

As reported previously [90], the order achieved in thin films made by PS-*b*-PEO copolymers depends only on either the solvent casting or the solvent vapor annealing conditions, and not the substrate. Furthermore, the presence of the solvent in these polymeric systems enhances the disorder degree within the polymeric chains since it mediates also nonfavorable interactions within the polymeric chains, working as plasticizers (affecting also the glass transition temperature value). When the evaporation phenomenon takes place at the film surface, microphase separation occurs and long-range lateral order is reached (as depicted in Figure 2). This way, a difference in terms of orientation is generated between the surface (i.e., low content of solvent, ordered system) and the bulk (i.e., high content of solvent, disordered system) of the polymeric film. However, as the solvent evaporates, the ordering front propagates through the films, thus extending the ordered microdomain growth following the solvent gradient direction (namely, perpendicular to the surface).

Since PEO is water soluble, it can be easily removed by simply heating and washing with water. In the work of Glassner et al. [62], they reported the synthesis of PS-*b*-PEO copolymers by coupling the reversible addition fragmentation chain transfer (RAFT) polymerization and the hetero Diels–Alder cycloaddition followed by subsequent retro-hetero Diels–Alder mechanisms by a heating/washing procedure. In this study, diblock copolymers are drop cast onto silicon wafers as substrates from a diluted chloroform solution. The SEM images in Figure 3 report the morphology of PS-*b*-PEO films after heating at 90 °C and washing with water. The formation of pores due to the removal of PEO domains is clearly demonstrated. Additionally, by increasing the amount of PEO moieties within the block copolymers (and/or consequently reducing the PS ones) a marked intensification in porosity is observed within the entire thickness of the film (thus suggesting that this phenomenon is not surface-limited).

In general, there are different methods for controlling the final morphology in the self-assembled BC coating. Some of these methods require the use of solvents, such as in the work of Karunakaran et al. [91] where the possibility of producing isoporous PS-*b*-PEO-based membranes by separating layers using water at room temperature as coagulant was reported. In this study, the PS-*b*-PEO BC membranes were obtained by a phase-inversion process starting from a solution of a DMAc/THF/sulfolane solvent mixture and by immersing the casting films in deionized water at room temperature. By comparison with analogous PS-*b*-P4VP membranes, the results obtained for PS-*b*-PEO membranes evidenced that the pore dimensions of

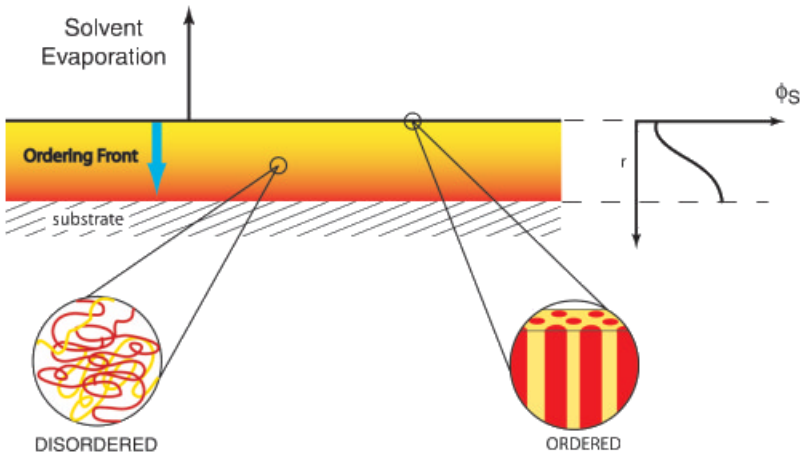

Figure 2: Schematic representation of the solvent evaporation in a thin film made by block copolymer. At the surface, the concentration of the solvent is low and the copolymer undergoes a well-ordered microphase separation. A gradient in the concentration of the solvent (as a function of the film thickness, *r*) is established perpendicular to the surface. In the bulk, the concentration of the solvent is high, thus block copolymer chains forming the interior part of the film are disordered. As the solvent evaporates, an ordered front propagates through the film thickness, producing a high vertically ordered cylindrical microdomain orientation. Reprinted with permission from [90], copyright 2004 Wiley-VCH.

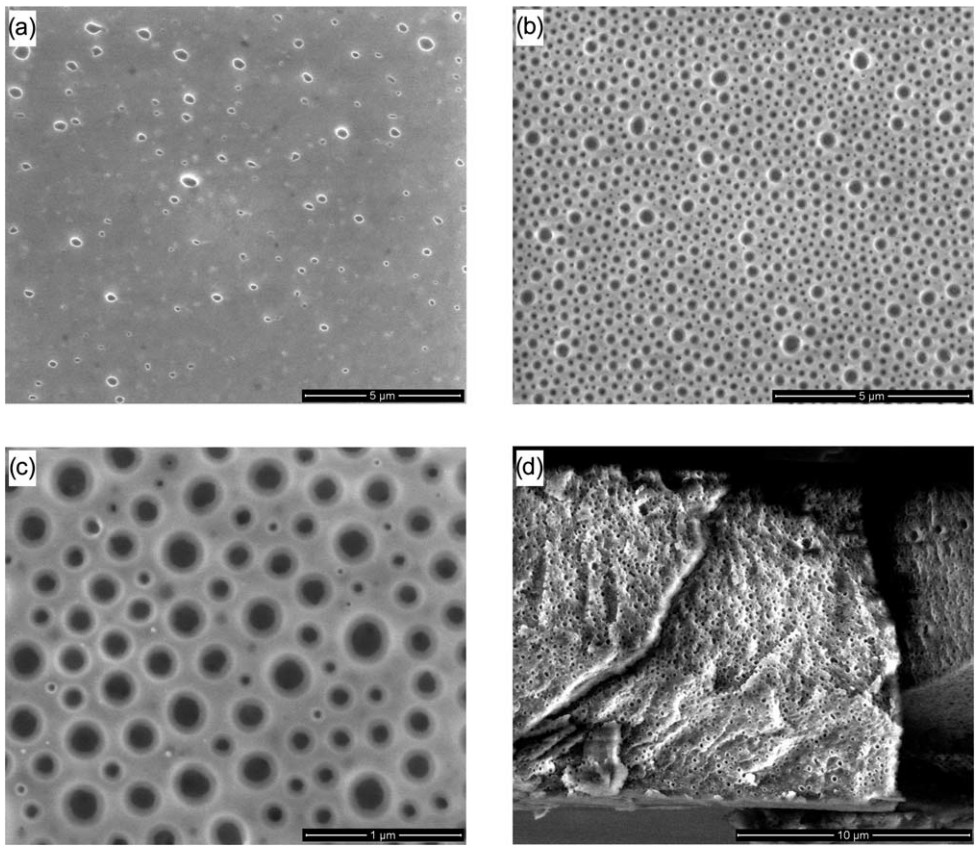

Figure 3: SEM micrographs of PS-*b*-PEO films after heating at 90 °C and washing with water. a) PS-*b*-PEO (18.5-*b*-5.0 kg mol^{-1}). b) PS-*b*-PEO (10.6-*b*-5.0 kg mol^{-1}) at low magnification. c) PS-*b*-PEO (10.6-*b*-5.0 kg mol^{-1}) at high magnification. d) Freeze fracture cross section PS-*b*-PEO (10.6-*b*-5.0 kg mol^{-1}). Reprinted with permission from [62], copyright 2011 The Royal Society of Chemistry.

the PS-*b*-PEO membranes are not affected by the pH change (in contrary to PS-*b*-P4VP). Additionally, since the membranes with PEO moieties present hydroxy end groups, the pore size can be tailored by further functionalization of the hydroxy functionality, thus making PS-*b*-PEO membranes attractive for several applications.

Other methods require the introduction of swelling agents (i.e., agents for increasing the microdomain dimensions) [92] as well as additives able to affect the microdomain orientation or act as a sacrificial component [64,93]. The inclusion of a homopolymer in the formulation is also a possible route to introduce particular effects on domain orientation and stability. As reported by Zhu et al. [93], PS-*b*-PEO BCs can be blended with PS homopolymers of different molecular weights to obtain a high molecular weight PS homopolymer with "hard confinement", whereas the low molecular weight one led to "soft confinement". Thus the thermodynamic stability of the PEO domains can be modulated in a controlled fashion.

In a previous study [64], solutions containing PS-*b*-PEO block copolymers were spin-coated onto a macroporous substrate (namely, silicon microsieves with pores of 5 µm width). Since the goal was to obtain a perpendicular cylindrical morphology, a possible technical solution is the addition of small molecules (or salts) able to stabilize a preferentially interaction with one of the blocks, through the formation of hydrogen bonding between the small organic molecules and one of the copolymer blocks. This way, it is possible to favor the normal orientation of the cylindrical nanodomains [94]. In this paper, resorcinol is selected as the orienting molecule to direct the orientation of the ethylene oxide cylindrical domains in PS-*b*-PEO copolymers. UV light irradiation was used to crosslink the PS matrix and photodegrade the PEO domains. Afterwards, several washing techniques were tested to selectively remove the resorcinol together with the PEO moieties (selective cleavage), where 2-propanol was determined to be the best solvent. As reported in Figure 4, the nanoporous thin membrane (i.e., pore size ≈20 nm) adheres to the macroporous substrate without any discontinuities. As reported in Figure 4d, the desired vertical alignment of the nanoporous system is maintained, even inside the substrate macropore. Additionally, transport studies were also performed, selecting two different target molecules. Size-selective sensitivity was confirmed, thus suggesting the possible

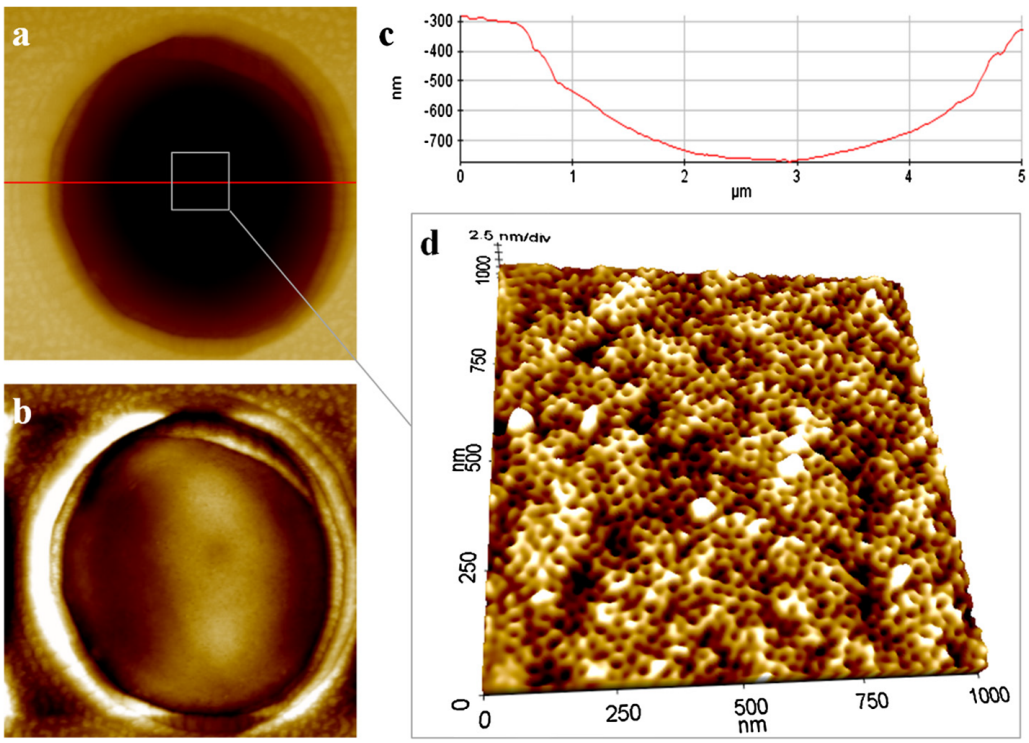

Figure 4: a) Atomic force microscopy (AFM) images of a composite nanoporous membrane: detail of the Si microsieve with the nanoporous polymeric membrane on top. b) Corrected AFM image showing the coverage of the Si macropore by the polymeric membrane. c) AFM profile corresponding to the horizontal line in a). d) 3D AFM image showing the morphology of the nanoporous layer within the macropore. Reprinted with permission from [64], copyright 2014 Elsevier.

application of these coatings in membrane technology for increasing the controlled transition of chemicals in separation processes.

Block copolymers and templating: theory and application

Amphiphilic BCs (such as PS-*b*-PEO) are a subcategory of copolymers which can self-organize to form supramolecular aggregates with specific shapes, such as: spherical, rod (or short cylindrical), hexagonally packed rod micelles, reverse micelles as well as worm-like structures, lamellar sheets, and vesicles (Figure 5). As mentioned previously, the thermodynamic incompatibility between the blocks forming the polymer chains is the driving force behind the formation of such nanostructures [4,35]. In this context, this peculiar characteristic can be coupled with sol–gel processes to produce well-ordered oxidic architectures [95,96].

The sol–gel process involves various chemical reactions such as hydrolysis, condensation, and consequently, polymerization involving the monomers (for inorganic systems, either metal alkoxides or metal chlorides) that evolves forming a colloidal solution (sol) and subsequently a stable network (gel) of polymerized particles. The byproducts of these polycondensation reactions are water and alcohol, depending on the precursor selected. Even if the principles behind the sol–gel reaction are very simple, several parameters can influence the resulting architecture of the designed material, such as the type of catalyst (i.e., acid or base), temperature conditions and atmosphere, reaction medium (i.e., either water or other non-aqueous solvents), and so on. For a detailed discussion concerning the principles behind sol–gel chemistry, please refer to [4].

In order to enhance the structural control in oxidic systems (and in particular by modulating the porosity organization), one possibility is to exploit the templating action of amphiphilic BC supramolecular structures working as structural directing agents (SDAs) [97,98]. This way, the final material corresponds to the negative replica of the SDA. There are two principal templating methods: hard templating (or nanocasting) and soft templating [97]. Hard templating involves an exotemplating approach, where the precursor solidifies within the solid SDA. In soft-templating, an endotemplating approach is used where the precursor starts to solidify around the porogens (which remain in the liquid state).

Regarding the hard-templating route, the preparation of titanium structures on block copolymer films has been recently re-

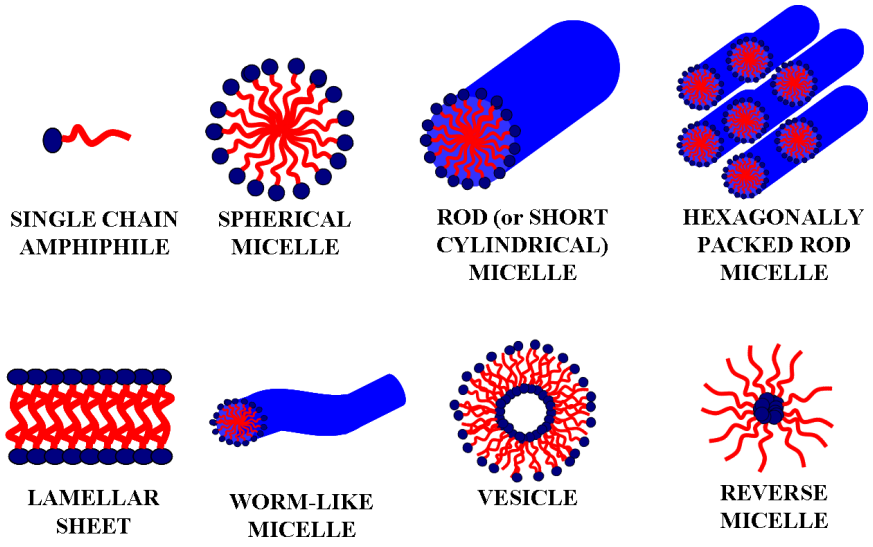

Figure 5: Schematic representation of different micellar architectures. Hydrophilic polar heads are indicated in blue, and hydrophobic non-polar tails are drawn in red. Reprinted from [22] ("Selective porous gates made from colloidal silica nanoparticles"); source published under Creative Commons Attribution 2.0 license, https://creativecommons.org/licenses/by/2.0/; copyright the authors.

ported, where the titanium assembly is driven by the microphase separation of the PS-*b*-PEO layer underneath [99]. When the titanium coating procedure is performed by electron beam evaporation onto a previously self-assembled PS-*b*-PEO substrate, Ti preferentially deposits and diffuses inside the PS matrix, thus leaving the PEO domains visible (and forming a porous structure). Analogous results were also obtained for cobalt onto PS-*b*-PEO [100].

Concerning the soft-templating route, usually the most diffuse porogens used are surfactants: small molecules characterized by having both polar (head) and apolar (tail) parts linked together by chemical bonds [101]. Analogous to surfactants, even amphiphilic block copolymers (such as the PS-*b*-PEO ones) can be used as templating agents [4].

As reported by Yu and co-workers [102], PS-*b*-PEO copolymers were used for the production of mesoporous silica films where a cubic close-packed spherical system was obtained by solvent evaporation induced self-assembly (EISA) process. Different pore sizes can be obtained by changing the block length in the soft templates. By coupling the spin-coating deposition technique with the soft-templating approach, mesoporous silica coatings were obtained using PS-*b*-PEO block copolymers as SDAs [103]. In this study, by modulating the starting composition (in particular, the hydrophilic/hydrophobic solvent ratio), a transition from stacked spherical pores to worm-like structures to spherical dense particles was reached due to the minimization of the surface free energy [104]. Analogously as for silica, even titania can be produced with closed spherical pores within the oxidic structures by using high molecular weight PS-*b*-PEO copolymers (as shown in Figure 6) [105].

Organic–inorganic PS-*b*-PEO/TiO_2 hybrid nanostructured coatings can also be produced by spin-coating deposition followed by calcination in order to obtain a nanostructured titania layer [106]. The thermal degradation of the organic polymeric template was successfully achieved without causing a collapse of the titania nanoarchitecture. The driving force behind these systems is the polar affinity between titania and the PEO domains (this is another advantage of this class of BCs, namely PS-*b*-PEO). By changing the titania precursor (i.e., TTIP) and the BC volume ratio, it was possible to drive the self-organization of the PEO domains, and consequently, the titania nanostructure. AFM images reported in this study show that after thermal treatment, a mesoporous titania coating is obtained where the spherical pore systems correspond to the PS spherical domains in the hybrid film before calcination. Depending on the formulation parameters and following the same procedure, even titania worm-like structures were obtained.

In this context, the exploitation of such functional porous coatings is very appealing from the membrane technology viewpoint by direct deposition onto a macroporous substrate (whose role is to guarantee the necessary mechanical resistance), thus forming functional filtering systems [107]. Among the different porous systems, a distinction can be realized between screen filters (well-ordered vertically aligned pore sieves, see

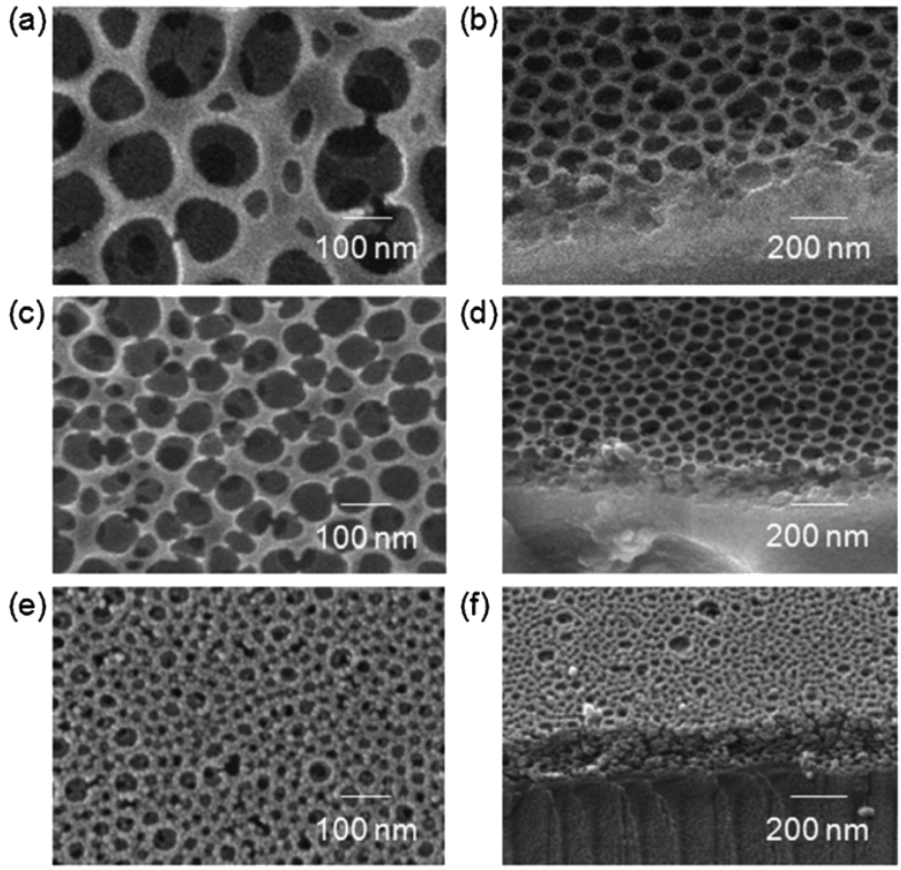

Figure 6: Top-view (left) and tilted 60° (right) SEM micrographs of PS_{962}-*b*-PEO_{3409} (a, b), PS_{563}-*b*-PEO_{1614} (c, d) and PS_{385}-*b*-PEO_{1205} (e, f) soft-templated titania films. Reproduced with permission from [105], copyright 2011 The Royal Society of Chemistry.

Figure 7A) and depth filters (disordered tortuous pore systems, see Figure 7B). The main difference between these two systems is the principle behind the sieving method: screen-filter separation is based on size exclusion, whereas depth-filter separation is based also on the interactions between the material forming the functional membrane and the target molecule being separated/isolated.

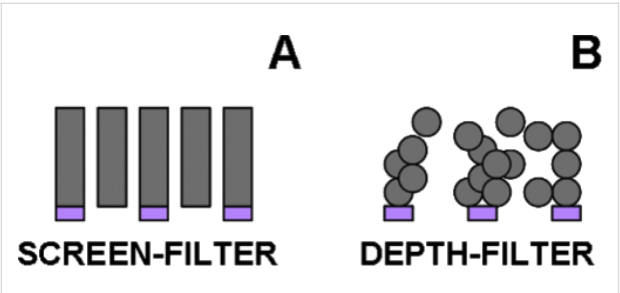

Figure 7: Schematic cross section of a screen filter (A) and a depth filter (B). Reprinted with permission from [4], copyright 2017 Elsevier.

In our recent study [22], colloidal silica nanoparticles (produced by using PS-*b*-PEO block copolymers as templates) are deposited via spin-coating onto a macroporous silicon-based substrate, forming a depth-filtering system (i.e., interparticle voids of 15–200 nm). In order to evaluate the selectivity of this porous membrane, two cationic (macro)molecules were selected as target probes: methylene blue (a dye of 0.5 nm in width) and the protein RNAse (3.8 nm), respectively. The results evidenced that the diffusion of the protein is more restricted as compared to the dye, suggesting a steric selectivity of the depth-filtering system analyzed. In addition, by applying an external electrical stimulus, the migration of both probes was registered with an increasing transport rate of the two chemical species.

Critical considerations

Membrane-mediated processes are widely considered one of the most promising solutions to be exploited for industrial separation and microfluidic dosing operations [108-110]. Currently, the integration of BCs (with their particular self-organizing capacity) is playing an increasing role in the development of nanoscale-controlled porous systems [4,111]. In this review, several case studies have been presented, highlighting the potential exploitation of PS-*b*-PEO amphiphilic block copolymers for designing both oxidic and polymeric nanoporous mem-

branes. For the sake of comparison, the choice of the best technical solution strongly depends on the matrix properties forming the advanced functional coatings.

BC-based polymeric nanoporous coatings guarantee both high morphological flexibility and a very narrow pore size distribution [112]. Additionally, such polymeric membranes are good candidates for the selective separation of (bio)molecules and microorganisms [75] as well as in water purification treatment due to their high selectivity, permeability, fouling resistance and mechanical strength. Eventually, further functionalizing can enhance the BC selectivity/affinity toward a particular target probe. Unfortunately, these advantages are partially annulled by a few drawbacks related to the production of these starting BCs (i.e., high cost, economic concern) and the organic solvents (which are sometimes not ecologically friendly) necessary for guiding the self-assembly (i.e., environmental concern).

On the other hand, the BC-templated porous inorganic coatings present several advantages and disadvantages depending on the templating technique selected. Soft templating, in particular, is the more versatile technique as it allows very complex morphologies to be obtained, which are almost impossible to obtain using nontemplated sol–gel processes [113]. Besides this fundamental advantage, for both templating methods, the principal critical step is the removal of the porogen without losing the designed nanostructure organization [4]. In general, this procedure is a very complex route that requires either strong acids/bases or selective organic solvent washing (not easy to handle or environmentally friendly), or thermal treatments (which risks the formation of carbonaceous residues entrapped within the inorganic porous architecture) [114]. Concerning hard templating, the structural compatibility between the SDA and the material precursor should be considered in a way that avoids undesirable voids or cracks induced by the solid templates [115].

Furthermore, the continuous development of novel functional substrates with highly controlled porosity is an increasing field of research that involves worldwide experts from both academia and industry. According to the works summarized in this review, the highly ordered nanostructures obtainable by exploiting the peculiar properties of BCs have found ample use in membrane technology, even if there are still economic and environmental concerns that need to be overcome. Among the different types of BCs, this review focused on the main results obtained for PS-*b*-PEO in particular. Due to the functionalities forming the two blocks, PS-*b*-PEO is a very attractive material for the production of (in)organic porous coatings and thin films to be exploited in membrane science and in dosing of chemicals. Additionally, the hydroxy end-functional groups forming the PEO domains constitute an interesting intermediate step for further functionalization, thus opening up even more application possibilities.

Conclusion

In this manuscript, the fabrication of well-ordered nanostructured porous coatings by means of block copolymers was reviewed. The most recent advances were summarized in order to provide a simple toolbox to follow for the preparation of (in)organic isoporous thin coatings exploitable for the development of novel well-ordered devices for membrane science and microfluidics applications. The interesting properties of amphiphilic block copolymers (taking PS-*b*-PEO as a model BC) in terms of self-assembly and templating action were highlighted, encouraging their use in important fields of research, such as in sensing, dosing, and separation processes. In this context, it is important to point out that membranes already find commercial application in many separation processes of complex matrices, such as in the clarification of beverages (i.e., milk, beer, and juices), the remediation of polluted water, or in the selective removal of bacteria and viruses from bloods. The main advantage of this technique is that membrane technology is a simple, robust, and well-consolidated technique that guarantees high performance and easy scale up, as compared to other more fascinating (albeit still at the laboratory scale) approaches, such as the use of magnetic adsorbing materials [116] or advanced oxidized processes [117,118]. On the other hand, future research should be focused on overcoming the economic and environmental concerns related to the exploitation of these block copolymers for designing nanostructured materials/coatings. To the best of our knowledge, there is no single, feasible technical solution available. The integration of consolidated processes with novel and more sustainable solutions could be a path forward, but the discussion is still open.

Acknowledgements

Polytechnic of Torino is gratefully acknowledged for funding the project Starting Grant RTD (project number: 54_RSG17NIR01). The author would like to thank Dr. Dominique Scalarone (University of Torino, Italy) for fruitful and nice discussions on the topic presented.

ORCID® iDs

Roberto Nisticò - https://orcid.org/0000-0001-8986-5542

References

1. Su, B.-L.; Sanchez, C.; Yang, X.-Y. *Hierarchically Structured Porous Materials: From Nanoscience to Catalysis, Separation, Optics, Energy, and Life Science;* Wiley-VCH Verlag GmbH & Co. KGaA: Weinheim, Germany, 2012.
2. Lu, A.-H.; Schüth, F. *Adv. Mater.* **2006,** *18,* 1793–1805. doi:10.1002/adma.200600148

3. Lee, J.; Kim, J.; Hyeon, T. *Adv. Mater.* **2006,** *18,* 2073–2094. doi:10.1002/adma.200501576
4. Nisticò, R.; Scalarone, D.; Magnacca, G. *Microporous Mesoporous Mater.* **2017,** *248,* 18–29. doi:10.1016/j.micromeso.2017.04.017
5. Liu, Q.; Tang, Z.; Ou, B.; Liu, L.; Zhou, Z.; Shen, S.; Duan, Y. *Mater. Chem. Phys.* **2014,** *144,* 213–225. doi:10.1016/j.matchemphys.2014.01.013
6. Lazzari, M.; López-Quintela, M. A. *Adv. Mater.* **2003,** *15,* 1583–1594. doi:10.1002/adma.200300382
7. Bagheri, S.; Hir, Z. A. M.; Yousefi, A. T.; Hamid, S. B. A. *Microporous Mesoporous Mater.* **2015,** *218,* 206–222. doi:10.1016/j.micromeso.2015.05.028
8. Biswas, A.; Bayer, I. S.; Biris, A. S.; Wang, T.; Dervishi, E.; Faupel, F. *Adv. Colloid Interface Sci.* **2012,** *170,* 2–27. doi:10.1016/j.cis.2011.11.001
9. Ozin, G. A.; Hou, K.; Lotsch, B. V.; Cademartiri, L.; Puzzo, D. P.; Scotognella, F.; Ghadimi, A.; Thomson, J. *Mater. Today* **2009,** *12,* 12–23. doi:10.1016/S1369-7021(09)70156-7
10. Liu, T.; Burger, C.; Chu, B. *Prog. Polym. Sci.* **2003,** *28,* 5–26. doi:10.1016/S0079-6700(02)00077-1
11. Gates, B. D.; Qiaobing, X.; Stewart, M.; Ryan, D.; Willson, C. G.; Whitesides, G. M. *Chem. Rev.* **2005,** *105,* 1171–1196. doi:10.1021/cr030076o
12. Apolinário, A.; Quitério, P.; Sousa, C. T.; Proença, M. P.; Azevedo, J.; Susano, M.; Moraes, S.; Lopes, P.; Ventura, J.; Araújo, J. P. *J. Phys.: Conf. Ser.* **2014,** *534,* No. 012001. doi:10.1088/1742-6596/534/1/012001
13. Pierre, A. C.; Pajonk, G. M. *Chem. Rev.* **2002,** *102,* 4243–4266. doi:10.1021/cr0101306
14. Gallego, E. M.; Paris, C.; Díaz-Rey, M. R.; Martínez-Armero, M. E.; Martínez-Triguero, J.; Martínez, C.; Moliner, M.; Corma, A. *Chem. Sci.* **2017,** *8,* 8138–8149. doi:10.1039/C7SC02858J
15. Wan, Y.; Yang, H.; Zhao, D. Y. *Acc. Chem. Res.* **2006,** *39,* 423–432. doi:10.1021/ar050091a
16. Kumar, P.; Pournara, A.; Kim, K.-H.; Bansal, V.; Rapti, S.; Manos, M. J. *Prog. Mater. Sci.* **2017,** *86,* 25–74. doi:10.1016/j.pmatsci.2017.01.002
17. Nisticò, R.; Tabasso, S.; Magnacca, G.; Jordan, T.; Shalom, M.; Fechler, N. *Langmuir* **2017,** *33,* 5213–5222. doi:10.1021/acs.langmuir.7b00142
18. Hentze, H.-P.; Antonietti, M. *Rev. Mol. Biotechnol.* **2002,** *90,* 27–53. doi:10.1016/S1389-0352(01)00046-0
19. Meseck, G. R.; Terpstra, A. S.; MacLachlan, M. J. *Curr. Opin. Colloid Interface Sci.* **2017,** *29,* 9–20. doi:10.1016/j.cocis.2017.01.003
20. Nisticò, R.; Magnacca, G.; Antonietti, M.; Fechler, N. *Z. Anorg. Allg. Chem.* **2014,** *640,* 582–587. doi:10.1002/zaac.201300526
21. Boffa, V.; ten Elshof, J. E.; Blank, D. H. A. *Microporous Mesoporous Mater.* **2007,** *100,* 173–182. doi:10.1016/j.micromeso.2006.10.035
22. Nisticò, R.; Avetta, P.; Calza, P.; Fabbri, D.; Magnacca, G.; Scalarone, D. *Beilstein J. Nanotechnol.* **2015,** *6,* 2105–2112. doi:10.3762/bjnano.6.215
23. Jin, J.; Wakayama, Y.; Peng, X.; Ichinose, I. *Nat. Mater.* **2007,** *6,* 686–691. doi:10.1038/nmat1980
24. Garcia Juez, R.; Boffa, V.; Blank, D. H. A.; ten Elshof, J. E. *J. Membr. Sci.* **2008,** *323,* 347–351. doi:10.1016/j.memsci.2008.06.043
25. König, K.; Boffa, V.; Buchbjerg, B.; Farsi, A.; Christensen, M. L.; Magnacca, G.; Yue, Y. *J. Membr. Sci.* **2014,** *472,* 232–240. doi:10.1016/j.memsci.2014.08.058
26. Brans, G.; Schroën, C. G. P. H.; van der Sman, R. G. M.; Boom, R. M. *J. Membr. Sci.* **2004,** *243,* 263–272. doi:10.1016/j.memsci.2004.06.029
27. Schmuhl, R.; Sekulic, J.; Roy Chowdhury, S.; van Rijn, C. J. M.; Keizer, K.; van den Berg, A.; ten Elshof, J. E.; Blank, D. H. A. *Adv. Mater.* **2004,** *16,* 900–904. doi:10.1002/adma.200306660
28. Ben, T.; Ren, H.; Ma, S.; Cao, D.; Lan, J.; Jing, X.; Wang, W.; Xu, J.; Deng, F.; Simmons, J. M.; Qiu, S.; Zhu, G. *Angew. Chem., Int. Ed.* **2009,** *48,* 9457–9460. doi:10.1002/anie.200904637
29. El-Kaderi, H. M.; Hunt, J. R.; Mendoza-Cortés, J. L.; Côté, A. P.; Taylor, R. E.; O'Keeffe, M.; Yaghi, O. M. *Science* **2007,** *316,* 268–272. doi:10.1126/science.1139915
30. Beiler, B.; Vincze, Á.; Svec, F.; Sáfrány, Á. *Polymer* **2007,** *48,* 3033–3040. doi:10.1016/j.polymer.2007.04.002
31. Rose, M.; Klein, N.; Senkovska, I.; Schrage, C.; Wollmann, P.; Böhlmann, W.; Böhringer, B.; Fichtner, S.; Kaskel, S. *J. Mater. Chem.* **2011,** *21,* 711–716. doi:10.1039/C0JM02998J
32. Olson, D. A.; Chen, L.; Hillmyer, M. A. *Chem. Mater.* **2008,** *20,* 869–890. doi:10.1021/cm702239k
33. Du, N.; Robertson, G. P.; Song, J.; Pinnau, I.; Thomas, S.; Guiver, M. D. *Macromolecules* **2008,** *41,* 9656–9662. doi:10.1021/ma801858d
34. Kim, J. K.; Yang, S. Y.; Lee, Y.; Kim, Y. *Prog. Polym. Sci.* **2010,** *35,* 1325–1349. doi:10.1016/j.progpolymsci.2010.06.002
35. Riess, G. *Prog. Polym. Sci.* **2003,** *28,* 1107–1170. doi:10.1016/S0079-6700(03)00015-7
36. Darling, S. B. *Prog. Polym. Sci.* **2007,** *32,* 1152–1204. doi:10.1016/j.progpolymsci.2007.05.004
37. Albert, J. N. L.; Epps, T. H., III. *Mater. Today* **2010,** *13,* 24–33. doi:10.1016/S1369-7021(10)70106-1
38. Hou, S.; Zheng, J.; Zhang, S.; Li, S. *Polymer* **2015,** *77,* 48–54. doi:10.1016/j.polymer.2015.09.024
39. Matsen, M. W.; Bates, F. S. *Macromolecules* **1996,** *29,* 1091–1098. doi:10.1021/ma951138i
40. Tseng, Y.-C.; Darling, S. B. *Polymer* **2010,** *2,* 470–489. doi:10.3390/polym2040470
41. Cochran, E. W.; Garcia-Cervera, C. J.; Fredrickson, G. H. *Macromolecules* **2006,** *39,* 2449–2451. doi:10.1021/ma0527707
42. Hu, H.; Gopinadhan, M.; Osuji, C. O. *Soft Matter* **2014,** *22,* 3867–3889. doi:10.1039/C3SM52607K
43. Huang, C.-I.; Lodge, T. P. *Macromolecules* **1998,** *31,* 3556–3565. doi:10.1021/ma980007p
44. Nandan, B.; Hsu, J.-Y.; Chen, H.-L. *Polym. Rev. (Philadelphia, PA, U. S.)* **2006,** *46,* 143–172. doi:10.1080/15321790600646802
45. Tata, J.; Scalarone, D.; Lazzari, M.; Chiantore, O. *Eur. Polym. J.* **2009,** *45,* 2520–2528. doi:10.1016/j.eurpolymj.2009.06.006
46. Guo, F.; Andreasen, J. W.; Vigild, M. E.; Ndoni, S. *Macromolecules* **2007,** *40,* 3669–3675. doi:10.1021/ma062947c
47. Okumura, A.; Nishikawa, Y.; Hashimoto, T. *Polymer* **2006,** *47,* 7805–7812. doi:10.1016/j.polymer.2006.08.043
48. Hashimoto, T.; Nishikawa, Y.; Tsutsumi, K. *Macromolecules* **2007,** *40,* 1066–1072. doi:10.1021/ma061739h
49. Boudouris, B. W.; Frisbie, C. D.; Hillmyer, M. A. *Macromolecules* **2008,** *41,* 67–75. doi:10.1021/ma071626d
50. Takahashi, A.; Rho, Y.; Higashihara, T.; Ahn, B.; Ree, M.; Ueda, M. *Macromolecules* **2010,** *43,* 4843–4852. doi:10.1021/ma100957q

51. Crossland, E. J. W.; Kamperman, M.; Nedelcu, M.; Ducati, C.; Wiesner, U.; Smilgies, D.-M.; Toombes, G. E. S.; Hillmyer, M. A.; Ludwigs, S.; Steiner, U.; Snaith, H. J. *Nano Lett.* **2009,** *9,* 2807–2812. doi:10.1021/nl803174p
52. Crossland, E. J. W.; Ludwigs, S.; Hillmyer, M. A.; Steiner, U. *Soft Matter* **2007,** *3,* 94–98. doi:10.1039/B609780D
53. Zhou, N.; Bates, F. S.; Lodge, T. P. *Nano Lett.* **2006,** *6,* 2354–2357. doi:10.1021/nl061765t
54. Fu, G.-D.; Yuan, Z.; Kang, E.-T.; Neoh, K.-G.; Lai, D. M.; Huan, A. C. H. *Adv. Funct. Mater.* **2005,** *15,* 315–322. doi:10.1002/adfm.200400138
55. Jones, B. H.; Lodge, T. P. *Chem. Mater.* **2010,** *22,* 1279–1281. doi:10.1021/cm903408x
56. Uehara, H.; Kakiage, M.; Sekiya, M.; Sakuma, D.; Yamonobe, T.; Takano, N.; Barraud, A.; Meurville, E.; Ryser, P. *ACS Nano* **2009,** *3,* 924–932. doi:10.1021/nn8008728
57. Uehara, H.; Yoshida, T.; Kakiage, M.; Yamanobe, T.; Komoto, T.; Nomura, K.; Nakajima, K.; Matsuda, M. *Macromolecules* **2006,** *39,* 3971–3974. doi:10.1021/ma0601316
58. Chen, L.; Hillmyer, M. A. *Macromolecules* **2009,** *42,* 4237–4243. doi:10.1021/ma900389n
59. Mao, H.; Hillmyer, M. A. *Macromolecules* **2005,** *38,* 4038–4039. doi:10.1021/ma050008z
60. Zhang, M.; Yang, L.; Yurt, S.; Misner, M. J.; Chen, J.-T.; Coughlin, E. B.; Venkataraman, D.; Russell, T. P. *Adv. Mater.* **2007,** *19,* 1571–1576. doi:10.1002/adma.200602461
61. Mao, H.; Hillmyer, M. A. *Soft Matter* **2006,** *2,* 57–59. doi:10.1039/B513958A
62. Glassner, M.; Blinco, J. P.; Barner-Kowollik, C. *Polym. Chem.* **2011,** *2,* 83–87. doi:10.1039/C0PY00267D
63. Fustin, C.-A.; Lohmeijer, B. G. G.; Duwez, A.-S.; Jonas, A. M.; Schubert, U. S.; Gohy, J.-F. *Adv. Mater.* **2005,** *17,* 1162–1165. doi:10.1002/adma.200402073
64. Iannarelli, L.; Nisticò, R.; Avetta, P.; Lazzari, M.; Magnacca, G.; Calza, P.; Fabbri, D.; Scalarone, D. *Eur. Polym. J.* **2015,** *62,* 108–115. doi:10.1016/j.eurpolymj.2014.11.019
65. Phillip, W. A.; O'Neill, B.; Rodwogin, M.; Hillmyer, M. A.; Cussler, E. L. *ACS Appl. Mater. Interfaces* **2010,** *2,* 847–853. doi:10.1021/am900882t
66. Tseng, W.-H.; Chen, C.-K.; Chiang, Y.-W.; Ho, R.-M.; Akasaka, S.; Hasegawa, H. *J. Am. Chem. Soc.* **2009,** *131,* 1356–1357. doi:10.1021/ja808092v
67. Lo, K.-H.; Tseng, W.-H.; Ho, R.-M. *Macromolecules* **2007,** *40,* 2621–2624. doi:10.1021/ma0628580
68. Olayo-Valles, R.; Guo, S.; Lund, M. S.; Leighton, C.; Hillmyer, M. A. *Macromolecules* **2005,** *38,* 10101–10108. doi:10.1021/ma0509006
69. Grande, D.; Penelle, J.; Davidson, P.; Beurroies, I.; Denoyel, R. *Microporous Mesoporous Mater.* **2011,** *140,* 34–39. doi:10.1016/j.micromeso.2010.10.007
70. Chao, C.-C.; Wang, T.-C.; Ho, R.-M.; Georgopanos, P.; Avgeropoulos, A.; Thomas, E. L. *ACS Nano* **2010,** *4,* 2088–2094. doi:10.1021/nn901370g
71. Yang, S. Y.; Park, J.; Yoon, J.; Ree, M.; Jang, S. K.; Kim, J. K. *Adv. Funct. Mater.* **2008,** *18,* 1371–1377. doi:10.1002/adfm.200700832
72. Melde, B. J.; Burkett, S. L.; Xu, T.; Goldbach, J. T.; Russell, T. P.; Hawker, C. J. *Chem. Mater.* **2005,** *17,* 4743–4749. doi:10.1021/cm051407b
73. Joo, W.; Park, M. S.; Kim, J. K. *Langmuir* **2006,** *22,* 7960–7963. doi:10.1021/la061441k
74. Hozumi, A.; Asakura, S.; Fuwa, A.; Shirahata, N. *J. Colloid Interface Sci.* **2005,** *285,* 875–878. doi:10.1016/j.jcis.2004.12.017
75. Yang, S. Y.; Ryu, I.; Kim, H. Y.; Kim, J. K.; Jang, S. K.; Russell, T. P. *Adv. Mater.* **2006,** *18,* 709–712. doi:10.1002/adma.200501500
76. Yang, S. Y.; Yang, J.-A.; Kim, E.-S.; Jeon, G.; Oh, E. J.; Choi, K. Y.; Hahn, S. K.; Kim, J. K. *ACS Nano* **2010,** *4,* 3817–3822. doi:10.1021/nn100464u
77. Crossland, E. J. W.; Cunha, P.; Scroggins, S.; Moratti, S.; Yurchenko, O.; Steiner, U.; Hillmyer, M. A.; Ludwigs, S. *ACS Nano* **2010,** *4,* 962–966. doi:10.1021/nn901447a
78. Drockenmuller, E.; Li, L. Y. T.; Ryu, D. Y.; Harth, E.; Russell, T. P.; Kim, H.-C.; Hawker, C. J. *J. Polym. Sci., Part A: Polym. Chem.* **2005,** *43,* 1028–1037. doi:10.1002/pola.20553
79. Leiston-Belanger, J. M.; Russell, T. P.; Drockenmuller, E.; Hawker, C. J. *Macromolecules* **2005,** *38,* 7676–7683. doi:10.1021/ma0507847
80. Lodge, T. P.; Pudil, B.; Hanley, K. J. *Macromolecules* **2002,** *35,* 4707–4717. doi:10.1021/ma0200975
81. Park, M. J.; Bang, J.; Harada, T.; Char, K.; Lodge, T. P. *Macromolecules* **2004,** *37,* 9064–9075. doi:10.1021/ma049285g
82. Huang, Y.-Y.; Chen, H.-L.; Hashimoto, T. *Macromolecules* **2003,** *36,* 764–770. doi:10.1021/ma0204305
83. Russell, T. P.; Karis, T. E.; Gallot, Y.; Mayes, A. M. *Nature* **1994,** *368,* 729–731. doi:10.1038/368729a0
84. Loo, Y.-L.; Register, R. A.; Ryan, A. J. *Macromolecules* **2002,** *35,* 2365–2374. doi:10.1021/ma011824j
85. He, W.-N.; Xu, J.-T. *Prog. Polym. Sci.* **2012,** *37,* 1350–1400. doi:10.1016/j.progpolymsci.2012.05.002
86. Patterson, D.; Robard, A. *Macromolecules* **1978,** *11,* 690–695. doi:10.1021/ma60064a015
87. Hamley, I. W. *The Physics of Block Copolymers;* Oxford University Press: Oxford, UK, 1998.
88. Burwell, R. L., Jr. *Chem. Rev.* **1954,** *54,* 615–685. doi:10.1021/cr60170a003
89. Kim, S. H.; Misner, M. J.; Russell, T. P. *Adv. Mater.* **2008,** *20,* 4851–4856. doi:10.1002/adma.200701206
90. Kim, S. H.; Misner, M. J.; Xu, T.; Kimura, M.; Russell, T. P. *Adv. Mater.* **2004,** *16,* 226–231. doi:10.1002/adma.200304906
91. Karunakaran, M.; Nunes, S. P.; Qiu, X.; Yu, H.; Peinemann, K.-V. *J. Membr. Sci.* **2014,** *453,* 471–477. doi:10.1016/j.memsci.2013.11.015
92. Wang, Y.; Tong, L.; Steinhart, M. *ACS Nano* **2011,** *5,* 1928–1938. doi:10.1021/nn1029444
93. Zhu, L.; Mimnaugh, B. R.; Ge, Q.; Quirk, R. P.; Cheng, S. Z. D.; Thomas, E. L.; Lotz, B.; Hsiao, B. S.; Yeh, F.; Liu, L. *Polymer* **2001,** *42,* 9121–9131. doi:10.1016/S0032-3861(01)00394-9
94. Sidorenko, A.; Tokarev, I.; Minko, S.; Stamm, M. *J. Am. Chem. Soc.* **2003,** *125,* 12211–12216. doi:10.1021/ja036085w
95. Ciriminna, R.; Fidalgo, A.; Pandarus, V.; Béland, V.; Ilharco, L. M.; Pagliaro, M. *Chem. Rev.* **2013,** *113,* 6592–6620. doi:10.1021/cr300399c
96. Brinker, C. J.; Scherer, G. W. *Sol-gel Science: the Physics and Chemistry of Sol-gel Processing;* Academic Press: San Diego, CA, 1990.
97. Schüth, F. *Angew. Chem., Int. Ed.* **2003,** *42,* 3604–3622. doi:10.1002/anie.200300593
98. Lofgreen, J. E.; Ozin, G. A. *Chem. Soc. Rev.* **2014,** *43,* 911–933. doi:10.1039/C3CS60276A

99. Kreuzer, M.; Simão, C.; Diaz, A.; Sotomayor Torres, C. M. *Polymer* **2016,** *105,* 195–202. doi:10.1016/j.polymer.2016.10.009
100. Metwalli, E.; Körstgens, V.; Schlage, K.; Meier, R.; Kaune, G.; Buffet, A.; Couet, S.; Roth, S. V.; Röhlsberger, R.; Müller-Buschbaum, P. *Langmuir* **2013,** *29,* 6331–6340. doi:10.1021/la400741b
101. Chen, F.; Huang, L.; Li, Q. *Chem. Mater.* **1997,** *9,* 2685–2686. doi:10.1021/cm9703942
102. Yu, K.; Smarsly, B.; Brinker, C. J. *Adv. Funct. Mater.* **2003,** *13,* 47–52. doi:10.1002/adfm.200390005
103. Nisticò, R.; Scalarone, D.; Magnacca, G. *Microporous Mesoporous Mater.* **2014,** *190,* 208–214. doi:10.1016/j.micromeso.2014.02.012
104. Nisticò, R.; Magnacca, G.; Jadhav, S. A.; Scalarone, D. *Beilstein J. Nanotechnol.* **2016,** *7,* 1454–1460. doi:10.3762/bjnano.7.137
105. Chandra, D.; Ohji, T.; Kato, K.; Kimura, T. *Phys. Chem. Chem. Phys.* **2011,** *13,* 12529–12535. doi:10.1039/C1CP21060B
106. Scalarone, D.; Tata, J.; Caldera, F.; Lazzari, M.; Chiantore, O. *Mater. Chem. Phys.* **2011,** *128,* 166–171. doi:10.1016/j.matchemphys.2011.02.053
107. Pevzner, S.; Regev, O.; Yerushalmi-Rozen, R. *Curr. Opin. Colloid Interface Sci.* **1999,** *4,* 420–427. doi:10.1016/S1359-0294(00)00018-2
108. Castel, C.; Favre, E. *J. Membr. Sci.* **2018,** *548,* 345–357. doi:10.1016/j.memsci.2017.11.035
109. Goh, P. S.; Matsuura, T.; Ismail, A. F.; Hilai, N. *Desalination* **2016,** *391,* 43–60. doi:10.1016/j.desal.2015.12.016
110. Lafleur, J. P.; Jönsson, A.; Senkbeil, S.; Kutter, J. P. *Biosens. Bioelectron.* **2016,** *76,* 213–233. doi:10.1016/j.bios.2015.08.003
111. Hamley, I. W. *Prog. Polym. Sci.* **2009,** *34,* 1161–1210. doi:10.1016/j.progpolymsci.2009.06.003
112. Samaddar, P.; Deep, A.; Kim, K.-H. *Chem. Eng. J.* **2018,** *342,* 71–89. doi:10.1016/j.cej.2018.01.062
113. Van Gough, D.; Juhl, A. T.; Braun, P. V. *Mater. Today* **2009,** *12,* 28–35. doi:10.1016/S1369-7021(09)70178-6
114. Lee, J.; Orilall, M. C.; Warren, S. C.; Kamperman, M.; DiSalvo, F. J.; Wiesner, U. *Nat. Mater.* **2008,** *7,* 222–228. doi:10.1038/nmat2111
115. Lu, A.-H.; Zhao, D.; Wan, Y. *Nanocasting: a Versatile Strategy for Creating Nanostructured Porous Materials*. *RSC Nanoscience and Nanotechnology N°11;* RSC Publishing: Cambridge (UK), 2010.
116. Nisticò, R. *Res. Chem. Intermed.* **2017,** *43,* 6911–6949. doi:10.1007/s11164-017-3029-x
117. Sillanpää, M.; Chaker Ncibi, M.; Matilainen, A. *J. Environ. Manage.* **2018,** *208,* 56–76. doi:10.1016/j.jenvman.2017.12.009
118. Palma, D.; Bianco Prevot, A.; Celi, L.; Martin, M.; Fabbri, D.; Magnacca, G.; Chierotti, M. R.; Nisticò, R. *Catalysts* **2018,** *8,* No. 197. doi:10.3390/catal8050197

License and Terms

BEILSTEIN JOURNAL OF NANOTECHNOLOGY

Nanoporous water oxidation electrodes with a low loading of laser-deposited Ru/C exhibit enhanced corrosion stability

Sandra Haschke[1], Dmitrii Pankin[2], Vladimir Mikhailovskii[3], Maïssa K. S. Barr[1], Adriana Both-Engel[1], Alina Manshina[4] and Julien Bachmann[*1,4]

Full Research Paper

Open Access

Address:
[1]Friedrich-Alexander University Erlangen-Nürnberg, Department of Chemistry and Pharmacy, Chair of Chemistry of thin film materials, Egerlandstrasse 3a, 91058 Erlangen, Germany, [2]Saint-Petersburg State University, Center for Optical and Laser Materials Research, Uljanovskaya 5, 198504 St. Petersburg, Russia, [3]Saint-Petersburg State University, Interdisciplinary Resource Center for Nanotechnology, Uljanovskaya 1, 198504 St. Petersburg, Russia and [4]Saint-Petersburg State University, Institute of Chemistry, Universitetskii pr. 26, 198504 St. Petersburg, Russia

Email:
Julien Bachmann* - julien.bachmann@fau.de

* Corresponding author

Keywords:
electrochemistry; nanostructures; noble metals; ruthenium catalyst; water splitting

Beilstein J. Nanotechnol. **2019,** *10,* 157–167.
doi:10.3762/bjnano.10.15

Received: 13 June 2018
Accepted: 19 December 2018
Published: 11 January 2019

This article is part of the thematic issue "Chemical thin coating methods for functional nanomaterials".

Associate Editor: P. Leiderer

Abstract

For the oxidation of water to dioxygen, oxide-covered ruthenium metal is known as the most efficient catalyst, however, with limited stability. Herein, we present a strategy for incorporating a Ru/C composite onto a novel nanoporous electrode surface with low noble metal loading and improved stability. The Ru/C is coated on the pore walls of anodic alumina templates in a one-step laser-induced deposition method from $Ru_3(CO)_{12}$ solutions. Scanning electron microscopy proves the presence of a continuous Ru/C layer along the inner pore walls. The amorphous material consists of metallic Ru incorporated in a carbonaceous C matrix as shown by X-ray diffraction combined with Raman and X-ray photoelectron spectroscopies. These porous electrodes reveal enhanced stability during water oxidation as compared to planar samples at pH 4. Finally, their electrocatalytic performance depends on the geometric parameters and is optimized with 13 µm pore length, which yields 2.6 mA cm^{-2}, or 49 A g^{-1}, at $\eta = 0.20$ V.

Introduction

The replacement of fossil fuels as the dominant global source of power by renewable energy sources has been and still is one of the major scientific and technological challenges faced by mankind. Among conceivable alternative energy sources, solar energy is the most suitable candidate due to its highest abundance on the global scale. Solar energy application on a large scale, however, necessitates its storage [1-4]. Here, nature provides the blueprint for the production of solar fuels by rearranging the chemical bonds of water to dihydrogen and dioxygen [1,5]. For the realization of artificial water splitting,

catalysts are required for the rate-limiting half reaction, the dioxygen evolution, which must be driven at low overpotential (for maximizing conversion efficiency) [2]. The most active catalyst materials for this transformation are metallic iridium and ruthenium particles, the surface of which consists of the corresponding oxide (Figure 1) [6,7]. Of the two, ruthenium (as its ruthenium(IV) oxide at the surface) not only proves to be the more efficient catalyst but is also the more abundant, and thus, the more cost-effective material [8].

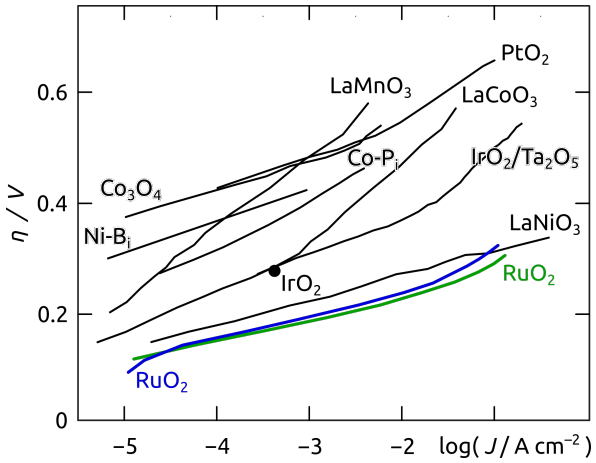

Figure 1: Selected oxygen evolution activities for planar state-of-the-art electrode materials (adapted from a review by Cook et al.) [9]. The overpotential η is shown here as a function of the logarithm of the current density J. The catalytic performance of ruthenium oxide in concentrated acidic and basic conditions is highlighted in green and blue, respectively.

However, its practical application is limited by its significant dissolution (corrosion) at high anodic potential over the whole pH range (Figure 2) [10-12]. One strategy to address this limitation has involved mixing metallic Ru (or its oxides) with other solids (such as Ir [13-18], Ta [19], or Pt [20], TiO_2 [21], Ni and Co [22]). Another approach entails increasing the specific surface area, which allows one to generate current at lower overpotential, for example by supporting RuO_2 nanoparticles on siliceous mesoporous materials [23-26], with mesoporous RuO_2 [27], or with RuO_2 supported on Sb-doped SnO_2 nanoparticles [18,28]. A carbonaceous support has also been used, with the advantages of chemical durability and electrical conductivity, as demonstrated in the context of alcohol dehydrogenation [29,30]. Such a support, however, has not been applied to the water oxidation reaction so far.

In this paper, we address this goal with the synthesis of metal/carbon composites via the laser-induced deposition method already described for carbon-encapsulated Ag/Au nanoparticles (AgAu/C) [31-33]. This practically appealing one-step technique bases on the photo-induced decomposition of a dissolved organometallic complex and the subsequent self-organization into hybrid metal/carbon nanostructures with controlled composition and morphology [32]. With the appropriate choice of laser wavelength and solvent, which both need to be adjusted to the absorption behavior of the organometallic complex, metal/carbon composites (M/C) can be generated in a straightforward manner onto the surface of any substrate with 2D or 3D architecture [34].

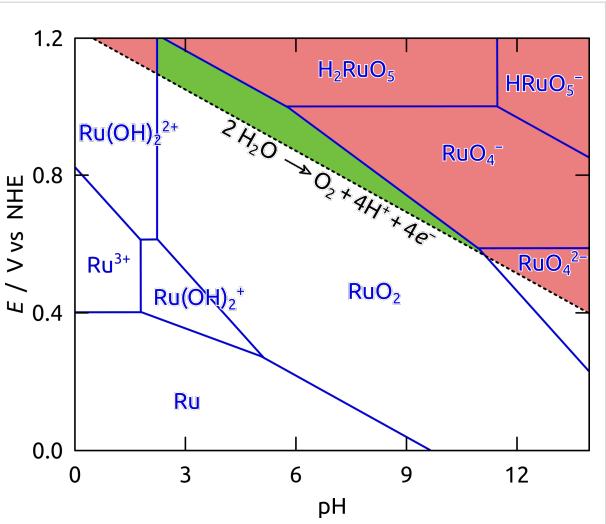

Figure 2: Pourbaix diagram for ruthenium in the presence of water (adapted from the Atlas of Eh-pH diagrams, Intercomparison of thermodynamic databases, Geological Survey of Japan Open File Report No.419) [12]. The limited thermodynamic stability of Ru is illustrated for positive potentials E in the range of $0 \le pH \le 14$ (blue lines) with the corresponding pH-dependent equilibrium potential for the water oxidation reaction (black dotted line). Regions of predominant thermodynamic stability and dissolution of the solid in water oxidation conditions are color-coded in green and red, respectively.

We first establish a novel laser-induced deposition method for Ru/C on planar substrates from commercially available triruthenium dodecacarbonyl ($Ru_3(CO)_{12}$). We then transfer the successful deposition method to the functionalization of highly ordered nanostructured anodic alumina templates [35-39] (Note: as our system is based on pores of diameter >50 nm, it is macroporous according to the IUPAC definition; we will use the more general wording “nanoporous” and “nanotubular” in the rest of the paper). These novel metal/carbon nanostructures are characterized regarding their morphology and phase composition. Finally, the electrocatalytic water oxidation performance of planar and nanostructured Ru/C electrodes is studied at pH 4. The focus lies on (1) the optimization of the nanoporous geometry (variation of the pore length) towards obtaining reasonable current densities at low overpotential, (2) the minimization of corrosion via minimized overpotential and nanoparticle morphology, and (3) the minimization of noble metal loading.

These efforts result in a very high activity (current per mass of noble metal) for electrocatalytic water oxidation.

Results and Discussion

Laser-induced deposition of planar hybrid Ru/C films

According to previous studies on the one-step laser-induced deposition method of AuAg/C composite, the choice of organometallic precursor, solvent, irradiation wavelength, and time crucially affect the quantity and quality of the coating [31,33,40]. For Ru/C deposition, we chose triruthenium dodecacarbonyl, $Ru_3(CO)_{12}$, as a 1 mg/mL 1,2-dichloroethane solution irradiated within its absorption band at 325 nm [41,42].

As planar substrates, microscope cover glasses provided with approx. 700 nm of heat-treated indium tin oxide (ITO, which serves as the electrical contact in subsequent electrochemical measurements) are placed for laser-induced coating on a microcuvette filled with the precursor solution. An unfocused He-Cd laser beam irradiates the substrate/solution interface from the substrate side for 30 min (Figure 3a,b).

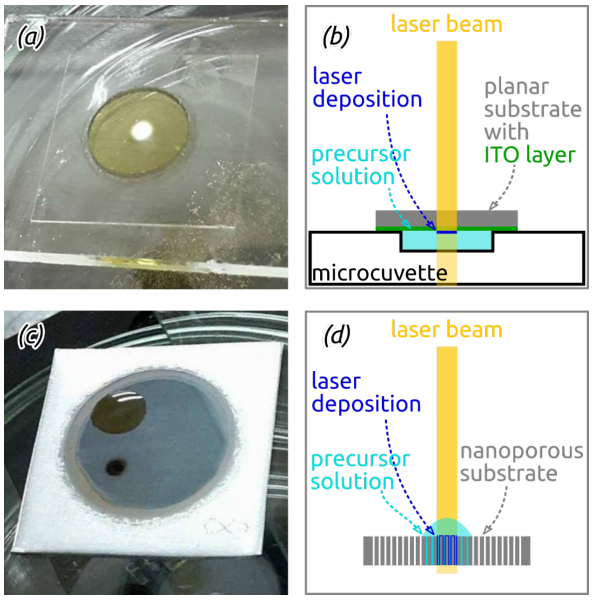

Figure 3: Photographs and schematic drawings of laser-induced chemical liquid deposition geometry on planar (a,b) and nanostructured samples (c,d) from $Ru_3(CO)_{12}$ solutions.

Scanning electron micrographs of a sample prove the successful deposition of a continuous albeit somewhat rough thin (≤20 nm) film (Figure 4a,b). Furthermore, energy-dispersive X-ray (EDX) analysis confirms the presence of Ru and C in the deposited film (see Figure S1 in Supporting Information File 1). This is the first demonstration of Ru/C hybrid material generated by laser-induced deposition. Furthermore, this represents the first use of a commercially available precursor in this method, which simplifies the procedure and renders it widely available.

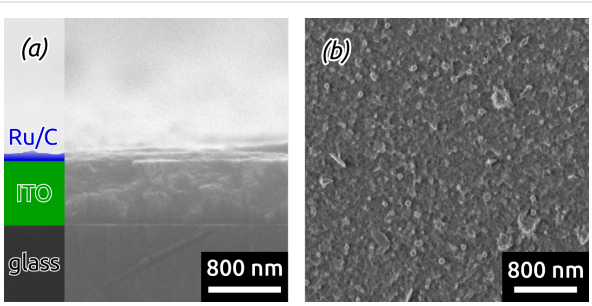

Figure 4: SEM images of planar samples coated with laser-induced Ru/C films in cross-section (a) and top-view (b). Laser-irradiation of $Ru_3(CO)_{12}$ solutions results in continuous and rough thin films deposited on ITO.

Laser-induced deposition on nanoporous substrates

This successful Ru/C laser deposition can now be transferred to anodic alumina templates featuring ordered arrays of parallel and cylindrical nanopores. The full preparation procedure is delineated in Figure 5. In the anodization conditions used here, the pitch P and diameter D are set to approx. 425 nm and 370 nm, respectively. This value of D is the maximum possible given a set P. It maximizes the specific surface area and thereby the electrocatalytic current density reachable [43]. The pore length is varied in the range of $11 \leq L \leq 24$ µm. In contrast to planar substrates, the laser beam must be directed to the solution/substrate interface after traversing the solution (Figure 3c,d).

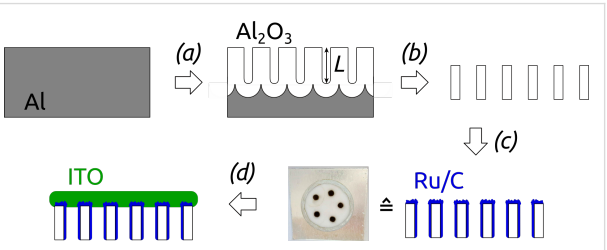

Figure 5: Preparation of nanostructured Ru/C electrodes. (a) Anodization of Al in 1 wt % H_3PO_4; this step defines the pore length L. (b) Removal of the Al substrate and Al_2O_3 barrier layer with simultaneous pore widening. (c) Laser-induced Ru/C decoration of the nanoporous Al_2O_3 surface. The photograph of the nanostructured surface after laser coating exhibits five well-defined dark deposition areas of 2 mm diameter on an anodic alumina substrate of 16 mm diameter. (d) Sputter-coating of the ITO backside contact.

In these conditions, deposition durations of 15 min are sufficient for the successful deposition of thin Ru/C coatings inside the Al_2O_3 pores (with additional material on the front sample

side, Figure 6a,d). In a last step, an ITO electrical contact is sputter-coated onto the front side of the sample. EDX spectroscopy reveals the presence of expected elements Al, O, P and In of the substrate and electrical contact, as well as Ru and C in the deposited layer (Figure 6c,d, Figure S2, Supporting Information File 1). The atomic ratios Ru/Al = 0.009 (±0.005) and C/Al = 0.137 (±0.031) (Table S1, Supporting Information File 1) demonstrate the low noble metal loading. These numbers can be expressed as 1.5 wt % Ru in our samples, or equivalently, 41 mg cm^{-3} (given the density of the Al_2O_3 framework) [44], or alternatively, as areal loadings, for example 53 µg cm^{-2} for a pore length of 13 µm. The volumetric value is comparable to state-of-the-art catalytic water oxidation systems based on supported RuO_x (40–50 mg cm^{-3} have been reported on siliceous supports) [23,24]. The areal loadings are as low as the lowest values found in the literature (amorphous RuO_2 with 49 µg cm^{-2} [45], mixed Ru–Pt catalyst with 15–35 µg cm^{-2} [20], and RuO_2 nanoparticles with 49 µg cm^{-2}) [46].

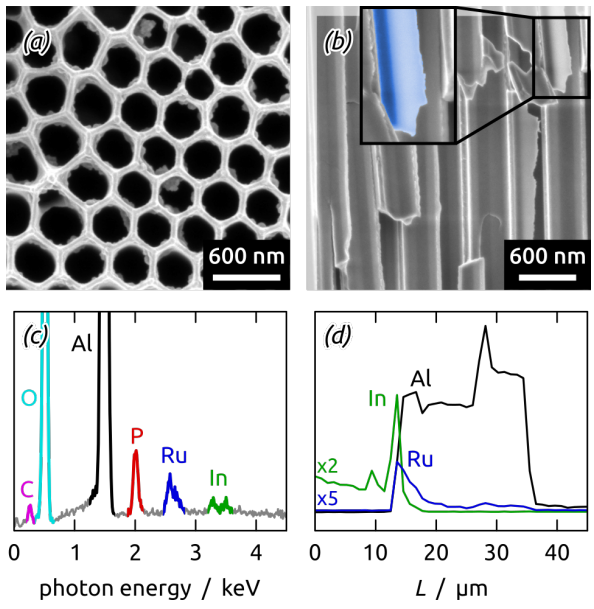

Figure 6: Scanning electron micrographs of a nanostructured Ru/C sample after all preparation steps in top view (a) and cross-section (b). EDX spectrum recorded over the whole sample length L = 24 µm (c). EDX profile taken along the cross-section (d). Laser-irradiation of $Ru_3(CO)_{12}$ solutions results in thin ruthenium containing coatings along the whole length of Al_2O_3 pores.

Chemical characterization of nanostructured Ru/C samples

The chemical and phase identity of the Ru/C material obtained by laser-induced deposition is delivered by a combination of X-ray diffraction, Raman spectroscopy and X-ray photoelectron spectroscopy. Firstly, the Ru/C layer is amorphous, since only crystalline Al peaks of the substrate are visible in the X-ray diffraction pattern (Figure S3, Supporting Information File 1).

The Raman spectra recorded on the Ru/C coated nanostructured sample (Figure 7a) can be divided into two distinct regions below 800 cm^{-1} and beyond it. In the low- frequency region, the broad peaks centered at 465 and 690 cm^{-1} can be attributed to hydrous ruthenium oxide ($RuO_2 \cdot nH_2O$) [47-51], whereby an overlap with Ru–C stretching modes cannot be excluded (see also the signal generated by the molecular precursor, Figure 7b). The 313 cm^{-1} peak originates from metallic Ru [52-55]. In the high-frequency region, the conspicuous maximum at ≈1600 cm^{-1} is due the stretching vibration of C=C bonds in aromatic or graphitic carbon. The peak at 1224 cm^{-1} corresponds to stretching vibrations of C–C and C–O single bonds (the 'disorder' peak usually found for graphitic material) [56-61]. Importantly, the absence of carbonyl stretching vibrations around 1950–2190 cm^{-1} rules out any remnants of molecular precursor $Ru_3(CO)_{12}$ (Figure 7b [52,62]).

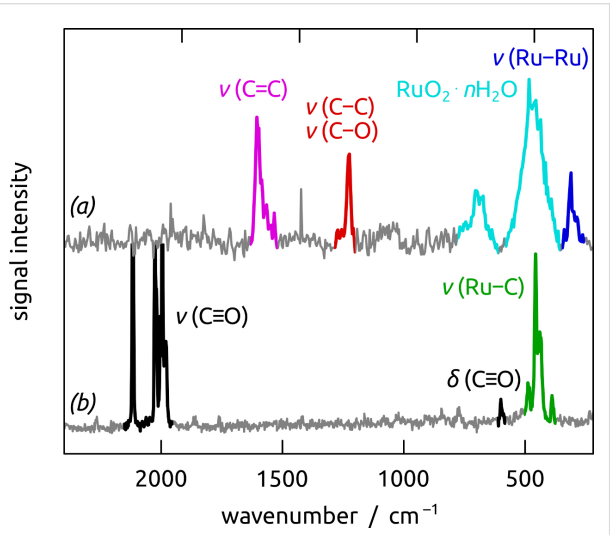

Figure 7: Raman spectra of a nanostructured template coated with Ru/C films, without ITO contact (a) and of the solid precursor $Ru_3(CO)_{12}$ (b).

X-ray photoelectron spectroscopy (XPS, Figure 8) is used to differentiate between the oxidation states of ruthenium at its surface and in its inner ("bulk"). The overview XPS spectrum of an as-prepared nanostructured sample features only Ru, O and C (Figure 8a) from the Ru/C layer, whereas the Al_2O_3 substrate is completely covered and reveals no Al signal. Deconvolution of the Ru 3d region, which is superimposed with C 1s (Figure 8b), reveals two doublets for two chemically different Ru environments. Their Ru $3d_{5/2}$ maxima are located at 281.1 eV and 281.8 eV, respectively, consistent with Ru(IV) oxide and Ru hydroxide [63-65]. Large carbon contributions are

additionally observable (partly O-bonded, Figure S4, Supporting Information File 1), which are due to the Ru/C layer and adventitious carbon. Argon ion sputtering results in a reduced carbon content (observable in both the C 1s and O 1s regions), as well as in a shift of the Ru 3d doublet of peaks to lower binding energies (Figure 8b and Figure S4, Supporting Information File 1). Thus, below the surface ruthenium is present in its metallic state (280.3 eV), whereas Ru(IV) oxide (281.1 eV) is still observable [63,66]. In conclusion, laser-induced deposition yields amorphous metallic Ru in close interaction with an amorphous carbonaceous C matrix, whereas the surface is completely oxidized, and in part hydrated.

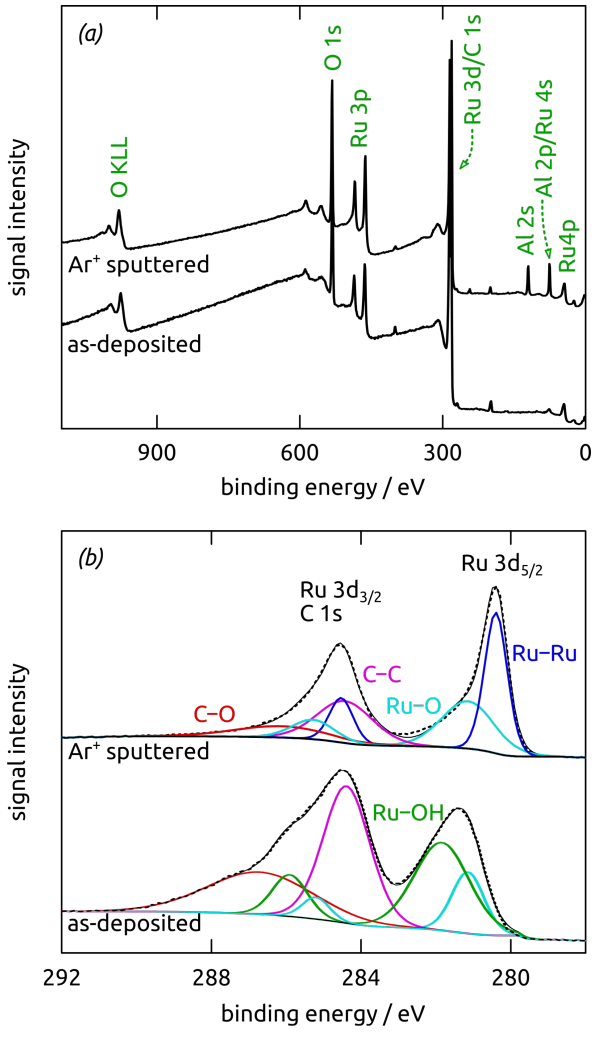

Figure 8: X-ray photoelectron spectra of a nanostructured Ru/C sample recorded as deposited and after Ar^+ sputtering. All spectra are shifted to a C 1s binding energy position of 284.4 eV. (a) Survey spectra showing the expected elements. (b) Ru 3d region, which is superimposed with the C 1s region, displays the Ru $3d_{5/2}$ and Ru $3d_{3/2}$ peaks. The experimental data are provided as dashed lines, the fit as solid black lines, and the individual deconvoluted peaks are color-coded.

Water oxidation at nanostructured Ru/C electrodes

We then applied our nanoporous Ru/C electrodes to the water oxidation reaction. Therefore, an approx. 1 µm thick ITO layer at one pore extremity serves as an electrical contact. We choose pH 4 (KH_2PO_4 buffer) for the investigations in order to secure the stability of the Al_2O_3 template, ITO and ruthenium (Figure 2). In cyclic voltammetry (Figure 9a), our nanotubular nt-Ru/C electrodes feature two broad oxidative peaks located around 0.0 V and +0.5 V vs the Ag/AgCl reference electrode. These peaks correspond to the oxidation of metallic Ru to Ru(II) and subsequently to Ru(IV) at the solid surface [10,67,68]. The oxygen evolution reaction starts beyond +0.8 V (E' = +0.79 V) vs Ag/AgCl at pH 4 whereas electro-corrosion to dissolved species (H_2RuO_5, RuO_4^-) begins at +0.95 V (Figure 2) [10,11]. These restrictions force us to never exceed +1.0 V applied potential. On the cathodic scan, only one reductive peak is present near 0.0 V, corresponding to the reduction of surface oxides to metallic Ru [68].

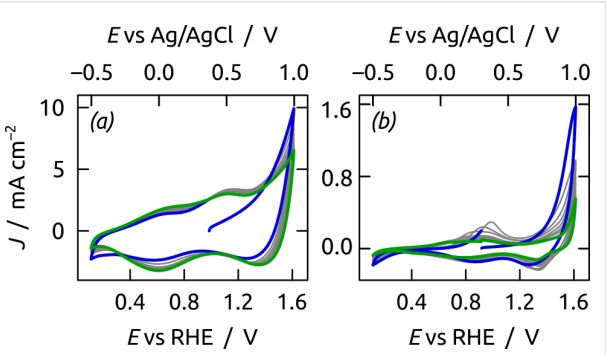

Figure 9: Cyclic voltammograms of Ru/C electrodes recorded in a KH_2PO_4 electrolyte at pH 4 (scan rate: 50 mV s^{-1}). The applied potential is presented versus the reversible hydrogen electrode (RHE) and Ag/AgCl reference electrode, respectively. Comparison of 10 successive cycles for a nanostructured (L = 13 µm) (a) and a planar Ru/C electrode (b). The first and last cycle are highlighted in blue and green, respectively. The current densities J are calculated from the experimental current intensity and the macroscopically exposed sample area.

The absence of surface oxidization current during the first CV cycle (blue curve in Figure 9a) indicates that the ruthenium catalyst as prepared is present as oxidized Ru(IV). This observation is consistent with the XPS analyses presented above. The consecutive cycles yield a rather constant hysteresis area, which indicates a low loss of material in electrochemical conditions. This relative stability of our nanoporous electrode stands in stark contrast to the planar Ru/C electrode (Figure 9b).

Firstly, the current density J (defined with respect to the experimentally accessible macroscopic sample area) starts out 6 times lower in the planar case than for the porous electrode. Secondly,

the loss of catalytic turnover of H_2O to O_2 visible at >0.9 V within 10 cycles is much more significant with the planar surface than with its porous counterpart. The area of the voltammetric hysteresis decreases concomitantly. These observations point to the rapid loss of noble metal catalyst from planar Ru/C surfaces.

The contrasting stability of planar and structured Ru/C electrodes can be tested further upon prolonged electrolysis. For this purpose, both types of electrodes were maintained at +0.90 V for 5 h (Figure 10). The water oxidation current density J on the planar Ru/C electrode declines to almost zero within about five minutes, whereas the nanostructured sample reaches a constant steady-state value J = 11.2 µA cm^{-2} after about three hours. This value is low, but is achieved at a very low overpotential, η = 0.11 V. We note that the integrated current (total charge passed over five hours) cannot be due solely to corrosion given the amount of carbon present. Thus, the application of the Ru/C laser deposition to nanoporous Al_2O_3 substrates yields a significant improvement of the catalyst stability in comparison to planar substrates. EDX analyses (Figures S1 and S2, Table S1, Supporting Information File 1) and cyclic voltammetry (Figure S5, Supporting Information File 1) performed after long-term bulk electrolyses support this statement.

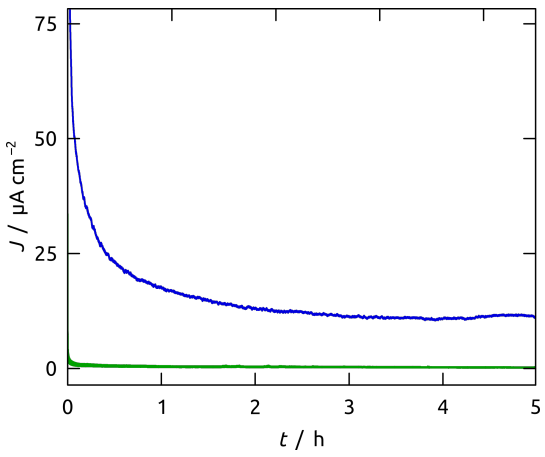

Figure 10: *J–t* curve of the same nanoporous (blue line) and planar (green line) electrode (as presented in Figure 7) during 5 h of steady-state electrolysis at +0.90 V vs Ag/AgCl.

Optimization of electrocatalytic performance

Our preparative procedure now allows us to adjust the geometric parameters of the nanoporous substrate in order to optimize the catalytic turnover of H_2O to O_2. Specifically, we will study the dependency of the current density J on the electrodes' geometric surface area via the variation of the pore length L (maintaining a constant pore diameter D). Figure 11 illustrates Tafel plots of Ru/C electrodes determined for pore lengths 11 ≤ L ≤ 24 µm measured within an applied overpotential range of 0.00 ≤ η ≤ 0.21 V (+0.79 ≤ E ≤ +1.00 V vs Ag/AgCl). All curves follow a similar trend and are located in close proximity of each other. However, the best performer is not the electrode type with the longest pores of L = 24 µm. Instead, those with 13 µm length yield the largest current densities at all overpotentials. They enable a water oxidation turnover that exceeds those of planar electrodes (L = 0 µm, Figure 11 inset) by approximately 1.5 decimal logarithmic units, or, equivalently, a factor 35.

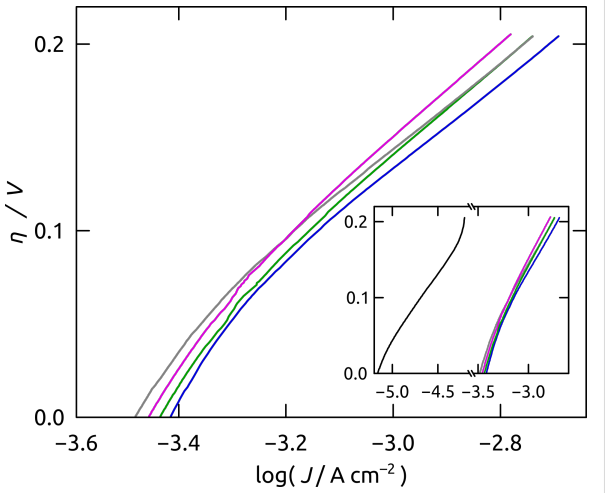

Figure 11: Tafel plots of nanoporous Ru/C electrodes of various lengths 11 ≤ L ≤ 24 µm in quasi-steady-state conditions. Tafel plots were obtained from linear sweep voltammetry (scan rate 5 mV s^{-1}) measured from +0.79 ≤ E ≤ +1.00 V vs Ag/AgCl (corresponding overpotentials 0.00 ≤ η ≤ 0.21 V). Average log J values for a minimum of 4 samples are presented for 11 µm (gray line), 13 µm (blue line), 18 µm (green line) and 24 µm (purple line). The inset compares all nanostructured electrodes with planar Ru/C electrodes (black line).

A clearer view of the length effect is provided by plots of *J–L* dependence at two distinct overpotentials, η = 0.10 V (mean values as green data points in Figure 12) and η = 0.20 V (blue data points). In both cases, pore elongation yields a rapid current density increase until a maximum is reached at 13 µm, followed by an activity loss for L > 13 µm. The current density loss is even more pronounced for η = 0.20 V than for 0.10 V, which can be attributed to transport limitation, since diffusion becomes more limiting at faster catalytic turnover. A similar observation was already made for Fe_2O_3-coated Al_2O_3 nanopores in the oxygen evolution reaction [69-71].

Conclusion

With this, we have established a novel type of nanostructured Ru/C composite electrode for the oxygen evolution reaction at pH 4 by laser-induced deposition. Laser irradiation of $Ru_3(CO)_{12}$ in 1,2-dichloroethane at 325 nm provides the first laser-induced coatings of hybrid Ru/C material on planar and

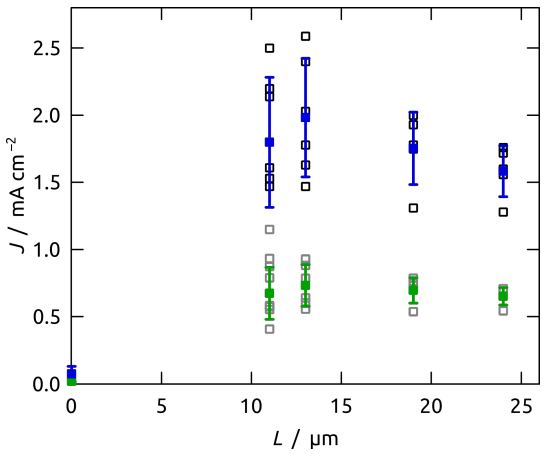

Figure 12: Current densities of Ru/C electrodes for water oxidation measured at pH 4 and at 0.10 V or 0.20 V applied overpotential. The current densities J are presented for individual samples in gray (η = 0.10 V) and black (η = 0.20 V), whereas the full green and blue squares correspond to the average values.

porous substrates. Along ordered cylindrical pores of high aspect ratio, the method yields thin and continuous films consisting of surface-oxidized metallic Ru incorporated in an amorphous carbonaceous carbon matrix.

This system applicable to the water oxidation reaction is advantageous with respect to the state of the art in several regards (Table 1) [14,18,20,28,45,46,72]:

1. Moderate current densities can be achieved at very low overpotential upon optimization of the nanoporous geometry. For example, pores of L = 13 µm deliver 2.6 mA cm^{-2} at η = 0.20 V. This value not only represents a 35-fold increase with respect to planar electrodes, it also is competitive with state-of-the-art ruthenium-based water oxidation electrodes (Table 1).
2. The nanoporous geometry, combined with the embedding of noble metal inside the carbonaceous matrix, stabilizes the electrocatalyst to the point that a steady state is reached upon continuous electrolysis. The current then stays stable for several hours. The comparison with the literature shows that only Kokoh et al. tested the long-term stability of their Ru-based electrocatalyst [14].
3. The fine dispersion of Ru in the conductive matrix and the high degree of geometric control afforded by the alumina support complement each other to optimize the contact between catalyst and electrolytic solution while minimizing transport effects. The noble metal loading can thereby be reduced to 53 µg cm^{-2}, and its activity optimized to 49 A g^{-1} (for L = 13 µm and η = 0.20 V), which is comparable to the best literature values (see Table 1 for a systematic comparison).
4. The metal/carbon composite is obtained in a single deposition step from a commercially available compound in an experimentally simple procedure.

The improved stability demonstrated here, the significant current densities, and the large activities obtained at low overpotential question the relative neglect of ruthenium in the water oxidation literature. This less costly metal could, given proper preparation procedures, advantageously replace iridium for some applications – most prominently electrical energy storage under nearly reversible conditions.

Experimental

Materials

Chemicals were purchased from Sigma-Aldrich, VWR, or Roth and used as received. Water was purified in a Millipore Direct-Q system for the application in electrolytes. As planar substrates, microscope cover glasses (borosilicate glass, 18 × 18 mm^2, 0.13–0.16 mm thickness) were purchased from

Table 1: Comparison of loadings ℓ, current densities J, and activities (specific currents $i_{sp} = J/\ell$) between selected literature precedents and the current results. At an overpotential of 0.2 V, our system reaches current densities comparable to the highest of the literature with Ru catalyst loadings comparable to the lowest in the literature. The activity is correspondingly maximal.

	ℓ µg cm^{-2}	$J_{\eta = 0.2\ V}$ mA cm^{-2}	$i_{sp,\ \eta = 0.2\ V}$ A g^{-1}	measurement conditions
this work	**53**	**2.6**	**49.1**	**5 mV s^{-1}**
Shao-Horn [46][a]	50	0.01	0.2	10 mV s^{-1}
Kokoh [14]	380	0.8	2.1	5 mV s^{-1}
Haverkamp [18]	160	1.0	6.3	20 mV s^{-1}
Mayrhofer [72]	370	5.0	13.5	10 mV s^{-1}
Strasser [20]	(14–35)	0.8	(23–56)	5 mV s^{-1}
Scott [28]	2000	232	116	/
Nakato [45]	49	7.5	154	5 mV s^{-1}

[a]The values reported in the Shao-Horn paper [46] are without internal resistance correction (to allow for a relevant comparison with other papers), at a slightly more elevated overpotential of η = 0.25 V.

Marienfeld-Superior. Aluminum plates (99.99%) for the anodization procedure were supplied by Smart-Membranes. The indium tin oxide sputter target (99.99%) was purchased from AEM.

Preparation of planar samples

For planar electrodes microscope cover glasses were ultrasonically cleaned with ethanol and water, then dried in a flow of nitrogen. In a next step, the slides were sputter-coated with approx. 700 nm of indium tin oxide (ITO) in radio frequency (RF) mode in a reactor from Torr International Inc. The conductive layer was subsequently annealed in N_2 atmosphere for 4 h at 400 °C in a high-temperature P330 furnace from Nabertherm. The planar substrates were then coated with Ru/C layers via laser-induced deposition. The precursor solution was prepared by ultrasonic dissolving of 1 mg of triruthenium dodecacarbonyl ($Ru_3(CO)_{12}$) in 1 mL of 1,2-dichloroethane ($C_2H_4Cl_2$) of analytical grade purity for 15–20 min. To remove the undissolved components, the solution was centrifuged with a SIGMA 2-16P centrifuge at 10000 rpm for 5 min. A microcuvette (d = 9 mm) was filled with the precursor solution and covered with the planar substrate with the ITO side facing the solution. Bubble formation in the solution was prevented via axial sliding of the substrate on the cuvette. An unfocused beam (ca. 2 mm in diameter) of a Plasma He-Cd laser (continuous wave (CW), λ = 325 nm, P = 10 mW) was directed to the substrate/solution interface from the side of glass for an irradiation duration of 30 min (Figure 3a,b). The maximum temperature in the laser focal spot does not exceed 27 °C as recorded with a Thermovision camera Ti32 from Fluke. After the deposition procedure the planar samples were washed in a flow of acetone and isopropanol.

Preparation of nanostructured samples

Nanostructured Ru/C electrodes were prepared in several steps as illustrated in Figure 5. A standard two-step anodization of aluminum (represented as (a) in Figure 5) delivered the nanoporous aluminum oxide membranes further used as templates [35]. Aluminum plates of 2.2 cm diameter were anodized in home-made two-electrode cells consisting of a PVC beaker with four circular openings at the bottom. They were therefore held between an O-ring and a thick copper plate operating as an electrical contact. Adequate cooling of the beaker was ensured via a cold plate connected to a closed-circuit cooler by Haake. The PVC beaker was filled with the electrolyte and closed with a lid equipped with a mechanical stirrer and silver wire mesh as counter-electrode. The whole setup was thermally insulated laterally. Electropolishing of the aluminum plates in a cooled perchloric acid/ethanol solution (1:3 v/v $HClO_4$/EtOH) for 5 min under +20 V represented the first process step. They were then rinsed, cooled and anodized under +195 V for 23 h at 0 °C in 1 wt % H_3PO_4. In the following, the anodized plates were exposed to a chromic acid solution (0.18 M CrO_3 in 6 wt % H_3PO_4) for 23 h at 45 °C for the removal of the disordered, porous Al_2O_3 generated. The second anodization was performed subsequently for 3, 4, 6 or 8 h at 0 °C in 1 wt % H_3PO_4 in order to vary the pore length. The next procedures (step (b) of Figure 5) included removing the metallic Al on the backside of the anodized Al_2O_3 with 0.7 M $CuCl_2$ solution in 10% HCl, followed by opening the Al_2O_3 barrier layer closing the pores with simultaneous isotropic pore widening in 10 wt % H_3PO_4 at 45 °C for 37 to 47 min. The laser-induced deposition of Ru/C coatings followed was adapted from the planar case (vide supra) (Figure 5 step (c)). 10 µL of the 1 mg/mL $Ru_3(CO)_{12}$ dichloroethane solution were dropped on the Al_2O_3 templates. The laser beam was directed to the solution/substrate interface from the side of the solution droplet (see Figure 3c,d) with an irradiation time of 15 min. As soon as the solution evaporated (approx. each 30 s) a new droplet was placed on the same spot. The nanostructured samples were then washed in a flow of acetone and isopropanol. Four to five depositions were performed on each substrate. In a last step, the electrical contact was generated by sputter-coating of approx. 1 µm ITO in RF mode on the sample side of laser deposition (step (d) in Figure 5).

Instrumental methods

Scanning electron micrographs were obtained on a Zeiss Merlin field-emission SEM with a field-emission cathode and standard In-lens SE and SE2 detectors. All measurements were performed in the chamber with a base pressure in the range of 10^{-7} mbar. The acceleration voltage was 10 to 1 keV with a beam current of 124–450 pA. Line averaging procedure was used for all images to reduce noise. Energy dispersive X-ray spectroscopy (EDX) was obtained on a JEOL JSM 6400 PC implemented with a LaB_6 cathode and silicon drift detector (SDD). All Raman spectra were collected at room temperature in a backscattering geometry using a Horiba Jobin-Yvon LabRam HR 800 Raman spectrometer equipped with an Olympus BX41 microscope. The spectra were obtained with 488 nm radiation from an Ar^+ gas laser and recorded in the 35–3290 cm^{-1} spectral range. The acquisition time was set to 500 s. The laser power was focused with a 100× objective on the sample and always kept at 5.4 µW. The spectra presented in this work are averaged from at least 5 measurements. The spectra were processed with LabSpec 5.78 including spike removal and baseline correction. The crystal structure was studied by powder X-ray diffraction measurements using a Bruker D8 Advance diffractometer in reflection mode and with Cu $K_{\alpha1}$ radiation (λ = 1.54056 Å) and LynxEye XE-T detector. Monochromatized Al K_α XPS spectra were acquired on a PHI Quantera II system with a base pressure of 10^{-9} mbar. Adventitious carbon was removed from the surface by 1 min, 2 kV Ar^+ ion

sputtering. To prevent charging a combination of electron and ion neutralization was employed. The Ru 3d and O 1s XPS core level spectra were analyzed using a fitting routine which decomposes each spectrum into individual mixed Gaussian–Lorentzian peaks using a Shirley background subtraction over the energy range of the fit. Finally, all spectra were shifted to give a C 1s binding energy position of 284.4 eV to correct for a slight overcompensation in the neutralization.

Electrochemical studies

Planar samples were laser-cut with a GCC LaserPro Spirit LS Laser into smaller areas of 1 cm^2, placed on small copper plates, whereby the electrical contact was established by double-sided conductive copper foil at the edges of the glass slide. In the case of nanostructured samples the individual deposition areas were laser-cut and subsequently glued with the ITO contact on small copper plates using double-sided conductive copper foil. A chemically resistant and electrically insulating polyimide (Kapton®) adhesive tape featuring a laser-cut circular window of 1.5 mm diameter was used to define the sample area exposed to the electrolyte. This macroscopically defined exposed sample area of 0.018 cm^2 is the value A used to define current densities ($J = I/A$) from the measured currents I. The samples were then adjusted into three-electrode electrochemical cells, exposing the defined sample area to a pH 4 phosphate electrolyte prepared from 0.1 M KH_2PO_4. The stability of the Al_2O_3 template and ITO backside contact in pH 4 conditions was verified with SEM after 20 h in the electrolyte. All electrochemical measurements including cyclic voltammetry (CV), linear sweep voltammetry (LSV) and steady-state electrolysis were performed from the open-circuit potential at room temperature using Gamry Interface 1000 potentiostats. The standard redox potential of the Ag/AgCl/KCl(sat.) reference electrode is shifted by +0.20 V relative to the normal hydrogen electrode (NHE). Cyclic and linear sweep voltammograms were measured at scan rates of 50 mV s^{-1} or 5 mV s^{-1}, respectively. Using the LSV data, Tafel plots were obtained for +0.79 V ≤ E ≤ +1.00 V vs Ag/AgCl (overpotentials 0.00 ≤ η ≤ 0.21 V). Steady-state electrolysis was measured for 5 h at +0.90 V. Additionally, a control experiment performed with a pure ITO contact on flat and nanostructured substrates demonstrated that the presence of ITO is irrelevant to the electrochemical performance.

Supporting Information

Supporting Information File 1

Additional experimental data.
[https://www.beilstein-journals.org/bjnano/content/supplementary/2190-4286-10-15-S1.pdf]

Acknowledgements

We thank A. Vasileva (Saint-Petersburg State University) for her support with laser deposition and Prof. K. Mayrhofer (Helmholtz Institute Erlangen-Nürnberg for Renewable Energy) for the use of the X-ray photoelectron spectrometer. This work was supported by the German Research Foundation (DFG) via the bridge funding of the excellence cluster "Engineering of Advanced Materials" (EXC315) and by the German Academic Exchange Service (DAAD) via the German-Russian Interdisciplinary Research Center (projects; C-2016b-2, C-21017a-2). The Raman measurements were performed at Research Park of Saint-Petersburg State University at Center for Optical and Laser Materials Research. The SEM micrographs were recorded at Saint-Petersburg State University Interdisciplinary Resource Center for Nanotechnology. Saint-Petersburg State University grant for equipment #12.40.1342.2017.

ORCID® iDs

Maïssa K. S. Barr - https://orcid.org/0000-0003-1587-2269
Alina Manshina - https://orcid.org/0000-0002-1053-6410
Julien Bachmann - https://orcid.org/0000-0001-6480-6212

References

1. Lewis, N. S.; Nocera, D. G. *Proc. Natl. Acad. Sci. U. S. A.* **2006,** *103,* 15729–15735. doi:10.1073/pnas.0603395103
2. Kanan, M. W.; Nocera, D. G. *Science* **2008,** *321,* 1072–1075. doi:10.1126/science.1162018
3. Panwar, N. L.; Kaushik, S. C.; Kothari, S. *Renewable Sustainable Energy Rev.* **2011,** *15,* 1513–1524. doi:10.1016/j.rser.2010.11.037
4. Sovacool, B. K. *Energy Res. Soc. Sci.* **2016,** *13,* 202–215. doi:10.1016/j.erss.2015.12.020
5. Nelson, N.; Ben-Shem, A. *Nat. Rev. Mol. Cell Biol.* **2004,** *5,* 971–982. doi:10.1038/nrm1525
6. Trasatti, S. *Electrochim. Acta* **1984,** *29,* 1503–1512. doi:10.1016/0013-4686(84)85004-5
7. Rasiyah, P.; Tseung, A. C. C. *J. Electrochem. Soc.* **1984,** *131,* 803–808. doi:10.1149/1.2115703
8. https://www.quandl.com/collections/markets/ (accessed Dec 11, 2017). Prices of noble metals.
9. Cook, T. R.; Dogutan, D. K.; Reece, S. Y.; Surendranath, Y.; Teets, T. S.; Nocera, D. G. *Chem. Rev.* **2010,** *110,* 6474–6502. doi:10.1021/cr100246c
10. Burke, L. D.; Mulcahy, J. K. *J. Electroanal. Chem. Interfacial Electrochem.* **1976,** *73,* 207–218. doi:10.1016/s0022-0728(76)80224-0
11. Michell, D.; Rand, D. A. J.; Woods, R. *J. Electroanal. Chem. Interfacial Electrochem.* **1978,** *89,* 11–27. doi:10.1016/s0022-0728(78)80027-8
12. Takeno, N. *Atlas of Eh-pH diagrams, Intercomparison of thermodynamic databases, Geological Survey of Japan Open File Report No.419;* National Institute of Advanced Industrial Science and Technology, Research Center for Deep Geological Environments: Tsukuba, Japan, 2005.

13. Kasian, O.; Geiger, S.; Stock, P.; Polymeros, G.; Breitbach, B.; Savan, A.; Ludwig, A.; Cherevko, S.; Mayrhofer, K. J. J. *J. Electrochem. Soc.* **2016,** *163,* F3099–F3104. doi:10.1149/2.0131611jes
14. Audichon, T.; Napporn, T. W.; Canaff, C.; Morais, C.; Comminges, C.; Kokoh, K. B. *J. Phys. Chem. C* **2016,** *120,* 2562–2573. doi:10.1021/acs.jpcc.5b11868
15. Cheng, J.; Zhang, H.; Chen, G.; Zhang, Y. *Electrochim. Acta* **2009,** *54,* 6250–6256. doi:10.1016/j.electacta.2009.05.090
16. Owe, L.-E.; Tsypkin, M.; Wallwork, K. S.; Haverkamp, R. G.; Sunde, S. *Electrochim. Acta* **2012,** *70,* 158–164. doi:10.1016/j.electacta.2012.03.041
17. Antolini, E. *ACS Catal.* **2014,** *4,* 1426–1440. doi:10.1021/cs4011875
18. Marshall, A. T.; Haverkamp, R. G. *Electrochim. Acta* **2010,** *55,* 1978–1984. doi:10.1016/j.electacta.2009.11.018
19. Yeo, R. S.; Orehotsky, J.; Visscher, W.; Srinivasan, S. *J. Electrochem. Soc.* **1981,** *128,* 1900–1904. doi:10.1149/1.2127761
20. Neyerlin, K. C.; Bugosh, G.; Forgie, R.; Liu, Z.; Strasser, P. *J. Electrochem. Soc.* **2009,** *156,* B363–B369. doi:10.1149/1.3049820
21. Näslund, L.-Å.; Sánchez-Sánchez, C. M.; Ingason, Á. S.; Bäckström, J.; Herrero, E.; Rosen, J.; Holmin, S. *J. Phys. Chem. C* **2013,** *117,* 6126–6135. doi:10.1021/jp308941g
22. Halck, N. B.; Petrykin, V.; Krtil, P.; Rossmeisl, J. *Phys. Chem. Chem. Phys.* **2014,** *16,* 13682–13688. doi:10.1039/c4cp00571f
23. Gustafson, K. P. J.; Shatskiy, A.; Verho, O.; Kärkäs, M. D.; Schluschass, B.; Tai, C.-W.; Åkermark, B.; Bäckvall, J.-E.; Johnston, E. V. *Catal. Sci. Technol.* **2017,** *7,* 293–299. doi:10.1039/c6cy02121b
24. Zhang, Y.; Ren, T. *Chem. Commun.* **2012,** *48,* 11005–11007. doi:10.1039/c2cc35272a
25. Mills, A.; Duckmanton, P. A.; Reglinski, J. *Chem. Commun.* **2010,** *46,* 2397–2398. doi:10.1039/b925784e
26. King, N. C.; Dickinson, C.; Zhou, W.; Bruce, D. W. *Dalton Trans.* **2005,** 1027–1032. doi:10.1039/b415288c
27. Iqbal, M. N.; Abdel-Magied, A. F.; Abdelhamid, H. N.; Olsén, P.; Shatskiy, A.; Zou, X.; Åkermark, B.; Kärkäs, M. D.; Johnston, E. V. *ACS Sustainable Chem. Eng.* **2017,** *5,* 9651–9656. doi:10.1021/acssuschemeng.7b02845
28. Wu, X.; Scott, K. *Int. J. Hydrogen Energy* **2011,** *36,* 5806–5810. doi:10.1016/j.ijhydene.2010.10.098
29. Spinacé, E. V.; Neto, A. O.; Linardi, M. *J. Power Sources* **2004,** *129,* 121–126. doi:10.1016/j.jpowsour.2003.11.056
30. Neto, A. O.; Dias, R. R.; Tusi, M. M.; Linardi, M.; Spinacé, E. V. *J. Power Sources* **2007,** *166,* 87–91. doi:10.1016/j.jpowsour.2006.12.088
31. Povolotskiy, A.; Povolotckaia, A.; Petrov, Y.; Manshina, A.; Tunik, S. *Appl. Phys. Lett.* **2013,** *103,* 113102. doi:10.1063/1.4820841
32. Manshina, A. A.; Grachova, E. V.; Povolotskiy, A. V.; Povolotckaia, A. V.; Petrov, Y. V.; Koshevoy, I. O.; Makarova, A. A.; Vyalikh, D. V.; Tunik, S. P. *Sci. Rep.* **2015,** *5,* 12027. doi:10.1038/srep12027
33. Schlicht, S.; Kireev, A.; Vasileva, A.; Grachova, E. V.; Tunik, S. P.; Manshina, A. A.; Bachmann, J. *Nanotechnology* **2017,** *28,* 065405. doi:10.1088/1361-6528/aa536a
34. Bashouti, M. Y.; Povolotckaia, A. V.; Povolotskiy, A. V.; Tunik, S. P.; Christiansen, S. H.; Leuchs, G.; Manshina, A. A. *RSC Adv.* **2016,** *6,* 75681–75685. doi:10.1039/c6ra16585k
35. Masuda, H.; Fukuda, K. *Science* **1995,** *268,* 1466–1468. doi:10.1126/science.268.5216.1466
36. Lee, W.; Park, S.-J. *Chem. Rev.* **2014,** *114,* 7487–7556. doi:10.1021/cr500002z
37. Santos, A.; Deen, M. J.; Marsal, L. F. *Nanotechnology* **2015,** *26,* 042001. doi:10.1088/0957-4484/26/4/042001
38. Santos, A.; Balderrama, V. S.; Alba, M.; Formentín, P.; Ferré-Borrull, J.; Pallarès, J.; Marsal, L. F. *Adv. Mater.* **2012,** *24,* 1050–1054. doi:10.1002/adma.201104490
39. Li, A.-P.; Müller, F.; Birner, A.; Nielsch, K.; Gösele, U. *Adv. Mater.* **1999,** *11,* 483–487. doi:10.1002/(sici)1521-4095(199904)11:6<483::aid-adma483>3.3.co;2-9
40. Manshina, A. A.; Povolotskiy, A. V.; Povolotskaya, A. V.; Ivanova, T. Y.; Koshevoy, I. O.; Tunik, S. P.; Suvanto, M.; Pakkanen, T. A. *Surf. Coat. Technol.* **2012,** *206,* 3454–3458. doi:10.1016/j.surfcoat.2012.02.010
41. Tyler, D. R.; Levenson, R. A.; Gray, H. B. *J. Am. Chem. Soc.* **1978,** *100,* 7888–7893. doi:10.1021/ja00493a017
42. Bag, A.; Ghorai, P. K. *RSC Adv.* **2015,** *5,* 31575–31583. doi:10.1039/c5ra01757b
43. Gemmer, J.; Hinrichsen, Y.; Abel, A.; Bachmann, J. *J. Catal.* **2012,** *290,* 220–224. doi:10.1016/j.jcat.2012.03.022
44. Abad, B.; Maiz, J.; Martin-Gonzalez, M. *J. Phys. Chem. C* **2016,** *120,* 5361–5370. doi:10.1021/acs.jpcc.6b00643
45. Tsuji, E.; Imanishi, A.; Fukui, K.-i.; Nakato, Y. *Electrochim. Acta* **2011,** *56,* 2009–2016. doi:10.1016/j.electacta.2010.11.062
46. Lee, Y.; Suntivich, J.; May, K. J.; Perry, E. E.; Shao-Horn, Y. *J. Phys. Chem. Lett.* **2012,** *3,* 399–404. doi:10.1021/jz2016507
47. Yang, H.; Yang, Y.; Zou, S. *J. Phys. Chem. B* **2006,** *110,* 17296–17301. doi:10.1021/jp063694s
48. Jo, H. C.; Kim, K. M.; Cheong, H.; Lee, S.-H.; Deb, S. K. *Electrochem. Solid-State Lett.* **2005,** *8,* E39–E41. doi:10.1149/1.1865673
49. Lee, S.-H.; Liu, P.; Seong, M. J.; Cheong, H. M.; Tracy, C. E.; Deb, S. K. *Electrochem. Solid-State Lett.* **2003,** *6,* A40–A42. doi:10.1149/1.1534731
50. Bhaskar, S.; Dobal, P. S.; Majumder, S. B.; Katiyar, R. S. *J. Appl. Phys.* **2001,** *89,* 2987–2992. doi:10.1063/1.1337588
51. Chan, H. Y. H.; Takoudis, C. G.; Weaver, M. J. *J. Catal.* **1997,** *172,* 336–345. doi:10.1006/jcat.1997.1841
52. Slebodnick, C.; Zhao, J.; Angel, R.; Hanson, B. E.; Song, Y.; Liu, Z.; Hemley, R. J. *Inorg. Chem.* **2004,** *43,* 5245–5252. doi:10.1021/ic049617y
53. Miskowski, V. M.; Loehr, T. M.; Gray, H. B. *Inorg. Chem.* **1987,** *26,* 1098–1108. doi:10.1021/ic00254a027
54. Chisholm, M. H.; Christou, G.; Folting, K.; Huffman, J. C.; James, C. A.; Samuels, J. A.; Wesemann, J. L.; Woodruff, W. H. *Inorg. Chem.* **1996,** *35,* 3643–3658. doi:10.1021/ic950860u
55. Fang, L.; Shen, X.; Chen, X.; Lombardi, J. R. *Chem. Phys. Lett.* **2000,** *332,* 299–302. doi:10.1016/s0009-2614(00)01260-4
56. Colthup, N. B. *J. Opt. Soc. Am.* **1950,** *40,* 397–400. doi:10.1364/josa.40.000397
57. *Course Notes on the Interpretation of Infrared and Raman Spectra;* Mayo, D. W.; Miller, F. A.; Hannah, R. W., Eds.; John Wiley & Sons, Inc.: Hoboken, NJ, U.S.A., 2004; pp 108–140. doi:10.1002/0471690082
58. Robinson, J. W. *Practical Handbook of Spectroscopy;* CRC Press Inc.: Boca Raton, FL, U.S.A., 1991.
59. Ferrari, A. C. *Solid State Commun.* **2007,** *143,* 47–57. doi:10.1016/j.ssc.2007.03.052

60. Ferrari, A. C.; Robertson, J. *Philos. Trans. R. Soc., A* **2004,** *362,* 2477–2512. doi:10.1098/rsta.2004.1452
61. Ferrari, A. C.; Robertson, J. *Phys. Rev. B: Condens. Matter Mater. Phys.* **2000,** *61,* 14095–14107. doi:10.1103/physrevb.61.14095
62. Quicksall, C. O.; Spiro, T. G. *Inorg. Chem.* **1968,** *7,* 2365–2369. doi:10.1021/ic50069a037
63. Moulder, J. F.; Stickle, W. F.; Sobol, P. E.; Bomben, K. D. Handbook of X-ray Photoelectron Spectroscopy. Perkin-Elmer Corporation Physical Electronics Division: Eden Prairie, MN, U.S.A., 1995; pp 10–115.
64. Morgan, D. J. *Surf. Interface Anal.* **2015,** *47,* 1072–1079. doi:10.1002/sia.5852
65. Wang, W.; Guo, S.; Lee, I.; Ahmed, K.; Zhong, J.; Favors, Z.; Zaera, F.; Ozkan, M.; Ozkan, C. S. *Sci. Rep.* **2014,** *4,* 4452. doi:10.1038/srep04452
66. Zhao, Y.; Zhang, J.; Song, J.; Li, J.; Liu, J.; Wu, T.; Zhang, P.; Han, B. *Green Chem.* **2011,** *13,* 2078–2082. doi:10.1039/c1gc15340d
67. Lezna, R. O.; De Tacconi, N. R.; Arvía, A. J. *J. Electroanal. Chem. Interfacial Electrochem.* **1983,** *151,* 193–207. doi:10.1016/s0022-0728(83)80433-1
68. Galizzioli, D.; Tantardini, F.; Trasatti, S. *J. Appl. Electrochem.* **1974,** *4,* 57–67. doi:10.1007/bf00615906
69. Haschke, S.; Wu, Y.; Bashouti, M.; Christiansen, S.; Bachmann, J. *ChemCatChem* **2015,** *7,* 2455–2459. doi:10.1002/cctc.201500623
70. Haschke, S.; Pankin, D.; Petrov, Y.; Bochmann, S.; Manshina, A.; Bachmann, J. *ChemSusChem* **2017,** *10,* 3644–3651. doi:10.1002/cssc.201701068
71. Schlicht, S.; Haschke, S.; Mikhailovskii, V.; Manshina, A.; Bachmann, J. *ChemElectroChem* **2018,** *5,* 1259–1264. doi:10.1002/celc.201800152
72. Cherevko, S.; Geiger, S.; Kasian, O.; Kulyk, N.; Grote, J.-P.; Savan, A.; Shrestha, B. R.; Merzlikin, S.; Breitbach, B.; Ludwig, A.; Mayrhofer, K. J. J. *Catal. Today* **2016,** *262,* 170–180. doi:10.1016/j.cattod.2015.08.014

License and Terms

BEILSTEIN JOURNAL OF NANOTECHNOLOGY

Uniform Sb_2S_3 optical coatings by chemical spray method

Jako S. Eensalu*, Atanas Katerski, Erki Kärber, Ilona Oja Acik, Arvo Mere and Malle Krunks*

Full Research Paper

Open Access

Address:
Laboratory of Thin Film Chemical Technologies, Department of Materials and Environmental Technology, Tallinn University of Technology, Ehitajate tee 5, Tallinn 19086, Estonia

Email:
Jako S. Eensalu* - jako.eensalu@taltech.ee; Malle Krunks* - malle.krunks@taltech.ee

* Corresponding author

Keywords:
antimony sulfide; thin films; ultrasonic spray; vacuum annealing; Volmer–Weber growth

Beilstein J. Nanotechnol. **2019,** *10,* 198–210.
doi:10.3762/bjnano.10.18

Received: 22 September 2018
Accepted: 04 December 2018
Published: 15 January 2019

This article is part of the thematic issue "Chemical thin coating methods for functional nanomaterials".

Guest Editor: J. Bachmann

Abstract

Antimony sulfide (Sb_2S_3), an environmentally benign material, has been prepared by various deposition methods for use as a solar absorber due to its direct band gap of ≈1.7 eV and high absorption coefficient in the visible light spectrum (1.8×10^5 cm^{-1} at 450 nm). Rapid, scalable, economically viable and controllable in-air growth of continuous, uniform, polycrystalline Sb_2S_3 absorber layers has not yet been accomplished. This could be achieved with chemical spray pyrolysis, a robust chemical method for deposition of thin films. We applied a two-stage process to produce continuous Sb_2S_3 optical coatings with uniform thickness. First, amorphous Sb_2S_3 layers, likely forming by 3D Volmer–Weber island growth through a molten phase reaction between $SbCl_3$ and $SC(NH_2)_2$, were deposited in air on a glass/ITO/TiO_2 substrate by ultrasonic spraying of methanolic Sb/S 1:3 molar ratio solution at 200–210 °C. Second, we produced polycrystalline uniform films of Sb_2S_3 (E_g 1.8 eV) with a post-deposition thermal treatment of amorphous Sb_2S_3 layers in vacuum at 170 °C, $<4 \times 10^{-6}$ Torr for 5 minutes. The effects of the deposition temperature, the precursor molar ratio and the thermal treatment temperature on the Sb_2S_3 layers were investigated using Raman spectroscopy, X-ray diffraction, scanning electron microscopy, energy dispersive X-ray spectroscopy and UV–vis–NIR spectroscopy. We demonstrated that Sb_2S_3 optical coatings with controllable structure, morphology and optical properties can be deposited by ultrasonic spray pyrolysis in air by tuning of the deposition temperature, the Sb/S precursor molar ratio in the spray solution, and the post-deposition treatment temperature.

Introduction

Antimony sulfide (Sb_2S_3) is an environmentally benign material. As Sb and S are abundant elements in the Earth's crust, enough raw materials can be supplied to manufacture large quantities of Sb_2S_3 in the long term. Sb_2S_3 can be applied as the inorganic absorber in solar cells due to its direct band gap of ≈1.7 eV [1,2].

Sb_2S_3, prepared by a chemical bath deposition (CBD) [3,4], spin coating [5], atomic layer deposition (ALD) [6] or chemical spray pyrolysis (CSP) [7] method, has been applied in extremely thin absorber (ETA) solar cells due to its excellent absorption coefficient in the visible light spectrum (1.8×10^5 cm^{-1} at 450 nm) [1,2]. Improvements in photocurrent density have been sought by utilizing a transparent, nanostructured window layer instead of planar window layers with the ETA Sb_2S_3 absorber layer [4,7]. Previous studies show that achieving sufficient repeatability alongside optimization of the component layers, i.e., transparent (structured) window layer, Sb_2S_3 absorber layer, and hole transport material layer, and their respective interfaces, is a tremendous undertaking [4].

Attention has surged toward planar heterojunction Sb_2S_3 solar cells due to their simpler structure, less intricate production, and enhanced repeatability vs structured solar cells [8]. Planar ≈1.7 eV absorber layers can be applied in semitransparent solar cells as well as in tandem solar cells.

Chemical spray pyrolysis (CSP) is a robust and industrially scalable chemical method for rapid deposition of thin films [9]. Our research group first investigated spray-deposited Sb_2S_3 by pneumatically spraying aqueous solutions (tartaric acid added as complexing agent to prevent hydrolysis [10], akin to studies by Rajpure et al. [11]) or methanolic solutions of $SbCl_3$. Following, we studied the effect of the Sb/S precursor molar ratio in solution on ultrasonically sprayed Sb_2S_3 layers and presented the first planar TiO_2/Sb_2S_3/P3HT solar cells comprising ultrasonically sprayed Sb_2S_3 (power conversion efficiency $\eta \leq 1.9\%$) [12].

$SbCl_3$ and thiourea ($SC(NH_2)_2$) are often used in the field to deposit Sb_2S_3 thin films. Spraying the $SbCl_3/SC(NH_2)_2$ (henceforth Sb/S) 1:6 molar ratio solution at 250 °C in air yielded separate Sb_2S_3 grains, which did not cover the TiO_2 substrate entirely, whereas spraying the Sb/S 1:3 solution yielded an inhomogeneous mix of amorphous and polycrystalline Sb_2S_3 [12]. We learned to produce continuous uniform layers of polycrystalline Sb_2S_3 by a two-step process on ZnO nanorod/TiO_2 substrates [7]. In this study, we applied this two-step process, i.e., depositing amorphous Sb_2S_3 layers on planar substrates, followed by post-deposition crystallization.

The aim of this study was to produce crystalline, continuous, Sb_2S_3 optical coatings with uniform thickness to be applied as a photovoltaic absorber by ultrasonic spraying on planar glass/ITO/TiO_2 substrates, followed by a post-deposition treatment. To this end, we studied the effect of the deposition temperature (T_D), the molar ratio of precursors $SbCl_3$ and thiourea ($SC(NH_2)_2$) in the spray solution, and the post-deposition treatment temperature on the structure, morphology and optical properties of ultrasonically sprayed Sb_2S_3 thin films.

Results and Discussion

Two sequential operations were used to obtain homogeneous Sb_2S_3 optical coatings with uniform thickness on planar TiO_2 substrates. First, we tuned the deposition temperature and molar ratio of Sb/S precursors in spray solution to deposit continuous amorphous Sb_2S_3 layers. An intimate contact, which is a prerequisite for high power conversion efficiency in solar cells [13], is formed at the interface between TiO_2 and Sb_2S_3 during deposition of amorphous Sb_2S_3 layers. Second, all layers were thermally treated in an inert environment (vacuum, $<4 \times 10^{-6}$ Torr) to induce crystallization, without oxidation.

Preliminary experiments at deposition temperatures lower than 182 °C (decomposition of $SC(NH_2)_2$ [14,15]) yielded inhomogeneous red-brown layers. Furthermore, in our previous paper, 250 °C was found to be too high a deposition temperature to obtain sufficient coverage of TiO_2 substrate by polycrystalline Sb_2S_3 thin films, despite the suitable band gap of 1.6 eV and high phase purity [12]. Restricted to deposition temperatures in the range 182–250 °C, we sprayed Sb/S 1:3 and 1:6 molar ratio precursor solutions at T_D = 200, 210, and 220 °C. We varied the aforementioned parameters to attain the conditions to deposit dense and homogeneous layers of amorphous Sb_2S_3, which we then crystallized by a post-deposition thermal treatment.

Based on the scanning electron microscopy (SEM) images, preliminary experiments revealed that spraying Sb/S 1:6 solutions consistently yielded twice thinner layers compared to layers deposited from Sb/S 1:3 solutions. Sb_2S_3 layers of comparable thickness were deposited by spraying Sb/S 1:6 solutions for 40 minutes and Sb/S 1:3 solutions for 20 minutes.

The samples are named in the text as follows: A-B-C, where A is the S/Sb molar ratio in solution, B is the deposition temperature, and C is the specification of the treatment. [Sb/S molar ratio in solution: “3” for Sb/S 1:3 or “6” for Sb/S 1:6]-[deposition temperature: “200”, “210” or “220” (°C)]-[treatment: “As-dep.” for as-deposited and “170”, “200” or “250” (°C) for samples thermally treated in vacuum].

The samples in which Sb_2S_3 layers were deposited from either Sb/S 1:3 or 1:6 solution at T_D = 200 °C, followed by thermal treatment in vacuum at 200 °C (3-200-200, 6-200-200), contain no Sb_2S_3, as it likely volatilized completely during the vacuum thermal treatment. Likewise, treating the Sb_2S_3 layers at temperatures higher than 200 °C caused Sb_2S_3 to completely volatilize during treatment. Photographs of the samples (Figure S1) and the description of the vapor pressure calculations

(Comment S1) are provided in the Supporting Information File 1. Consequently, only as-deposited samples and samples thermally treated in vacuum at 170 °C and 200 °C are eligible for discussion.

Structure of as-deposited and thermally treated Sb_2S_3 layers

Raman spectroscopy provides quantitative and qualitative information on the vibrational modes in solids. The wide Raman band centered at 290 cm^{-1} [12,16] associated with metastibnite, i.e., amorphous Sb_2S_3, is characteristic of as-deposited orange colored (photograph in Supporting Information File 1, Figure S1) samples (3-200-As-dep., 3-210-As-dep., Figure 1A; 6-200-As-dep., Figure 1B). The band centered at 145 cm^{-1} is a low frequency E_g vibrational mode of anatase-TiO_2 [17], which is observed due to the laser beam penetrating to the substrate [12,16] through the discontinuous Sb_2S_3 layers. The TiO_2 vibrational band is absent in spectra of Sb_2S_3 layers containing less pinholes, as the signal is captured only from Sb_2S_3.

The narrower bands, attributed to orthorhombic Sb_2S_3 [16,18-20], are present in the spectra of as-deposited and thermally treated lustrous gray (photograph in Supporting Information File 1, Figure S1) samples (3-200-170, 3-210-170, 3-210-200, 3-220-As-dep., 3-220-170, 3-220-200, Figure 1A; 6-200-170, 6-210-As-dep., 6-210-170, 6-210-200, 6-220-As-dep., 6-220-170, 6-220-200, Figure 1B; photograph in Supporting Information File 1, Figure S1). According to group theory, orthorhombic Sb_2S_3 has 30 predicted Raman active modes: $\Gamma_{Raman} = 10A_g + 5B_{1g} + 10B_{2g} + 5B_{3g}$ [18,20]. The Raman spectra were deconvoluted using Lorentzian fitting into vibrational bands of Sb_2S_3 based on the literature [12,16,21,22]. The centers of the bands of Sb_2S_3 in the deconvoluted Raman spectra (Table 1, symmetries taken from [20,21]) are similar to

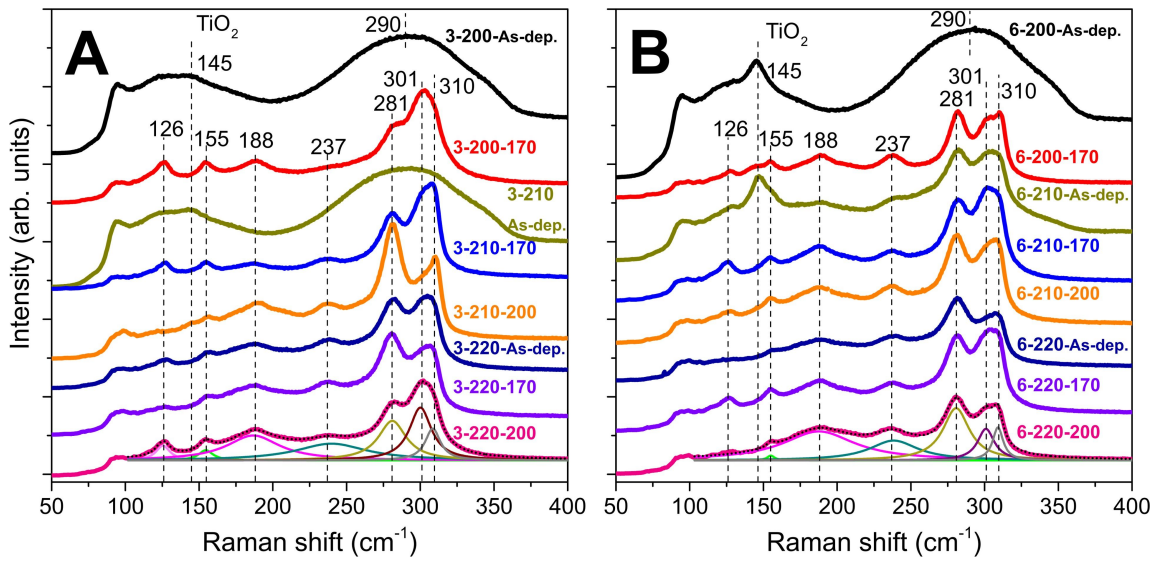

Figure 1: Raman spectra (shifted for visibility) of the as-deposited and thermally treated Sb_2S_3 films deposited from Sb/S 1:3 (A) or 1:6 (B) solution at 200, 210, 220 °C. Examples of deconvoluted fitted band curves are presented for the lowermost spectra. Sample names in figures: [S/Sb molar ratio in solution]-[deposition temperature]-[thermal treatment temperature].

Table 1: Raman band centers and assigned active modes for the studied Sb_2S_3 layers.

Center of Raman band, cm^{-1}			Symmetry		Vibrational mode, [21-23]
This study	Ref. [21]	Ref. [20]	Ref. [21]	Ref. [20]	
126	125	129	A_g	A_g	lattice mode
155	156	158	A_g	A_g/B_{2g}	lattice mode
188	189	186	B_{1g}	B_{1g}	antisym. S–Sb–S bending
237	237	239	B_{1g}	B_{1g}/B_{3g}	symmetric S–Sb–S bending
281	281	282	A_g	A_g/B_{2g}	antisym. S–Sb–S stretching
301	300	299	A_g	A_g/B_{2g}	antisym. S–Sb–S stretching
310	310	312	A_g	A_g/B_{2g}	symmetric S–Sb–S stretching

values reported in our previous studies [7,12]. Band centers, relative single peak intensities and full widths at half maximum (FWHM) of the narrow bands centered at 281, 301 and 310 cm^{-1} can be respectively found in Tables S1, S2, and S3 of Supporting Information File 1.

The FWHM of the vibrational band centered at 281 cm^{-1} narrows from ≈24 cm^{-1} to 21–23 cm^{-1} after vacuum thermal treatment of the samples deposited at 210–220 °C from both Sb/S 1:3 and Sb/S 1:6 solutions (3-210-170, 3-220-170, 6-210-170 and 6-220-170) at 170 °C (3-210-170, 3-220-170, 6-210-170 and 6-220-170) and narrows by 5 cm^{-1} at most after vacuum thermal treatment at 200 °C (3-210-200). The narrowing of the Raman bands due to thermal treatment leads us to suppose that crystallization continues during the vacuum thermal treatment and proceeds further at higher thermal treatment temperatures [16]. The vibrational bands corresponding to Sb_2O_3 were not detected by Raman spectroscopy in any of the studied glass/ITO/TiO_2/Sb_2S_3 samples.

X-ray diffraction (XRD) provides qualitative information on the phase composition and crystal structure. XRD patterns of reference glass/ITO/TiO_2 samples and samples containing XRD-amorphous Sb_2S_3 (3-200-As-dep., 3-210-As-dep., Figure 2A; 6-200-As-dep., Figure 2B) show only diffraction peaks corresponding to cubic In_2O_3 (2θ = 21.3°, 30.4°, 35.3°, 37.4°, 41.4°, 45.3°, ICDD PDF 03-065-3170) and anatase-TiO_2 (25.3°, 48.2°, ICDD PDF 00-016-0617). The diffraction peaks of orthorhombic Sb_2S_3 (ICDD PDF 01-075-4012), space group *Pnma* (D_{2h}^{16}) [20,24,25], appear in XRD patterns of lustrous gray as-deposited and thermally treated Sb_2S_3 samples (3-200-170, 3-210-170, 3-210-200, 3-220-As-dep., 3-220-170, 3-220-200, Figure 2A; 6-200-170, 6-210-As-dep., 6-210-170, 6-210-200, 6-220-As-dep., 6-220-170, 6-220-200, Figure 2B). The 2θ angles of observed Sb_2S_3 diffraction peaks and corresponding crystal plane indices are presented in Supporting Information File 1, Table S4. Experimentally determined mean lattice constants *a*, *b* and *c* of Sb_2S_3 are 11.25 ± 0.07 Å, 3.810 ± 0.025 Å and 11.16 ± 0.07 Å, respectively. Our experimentally deter-

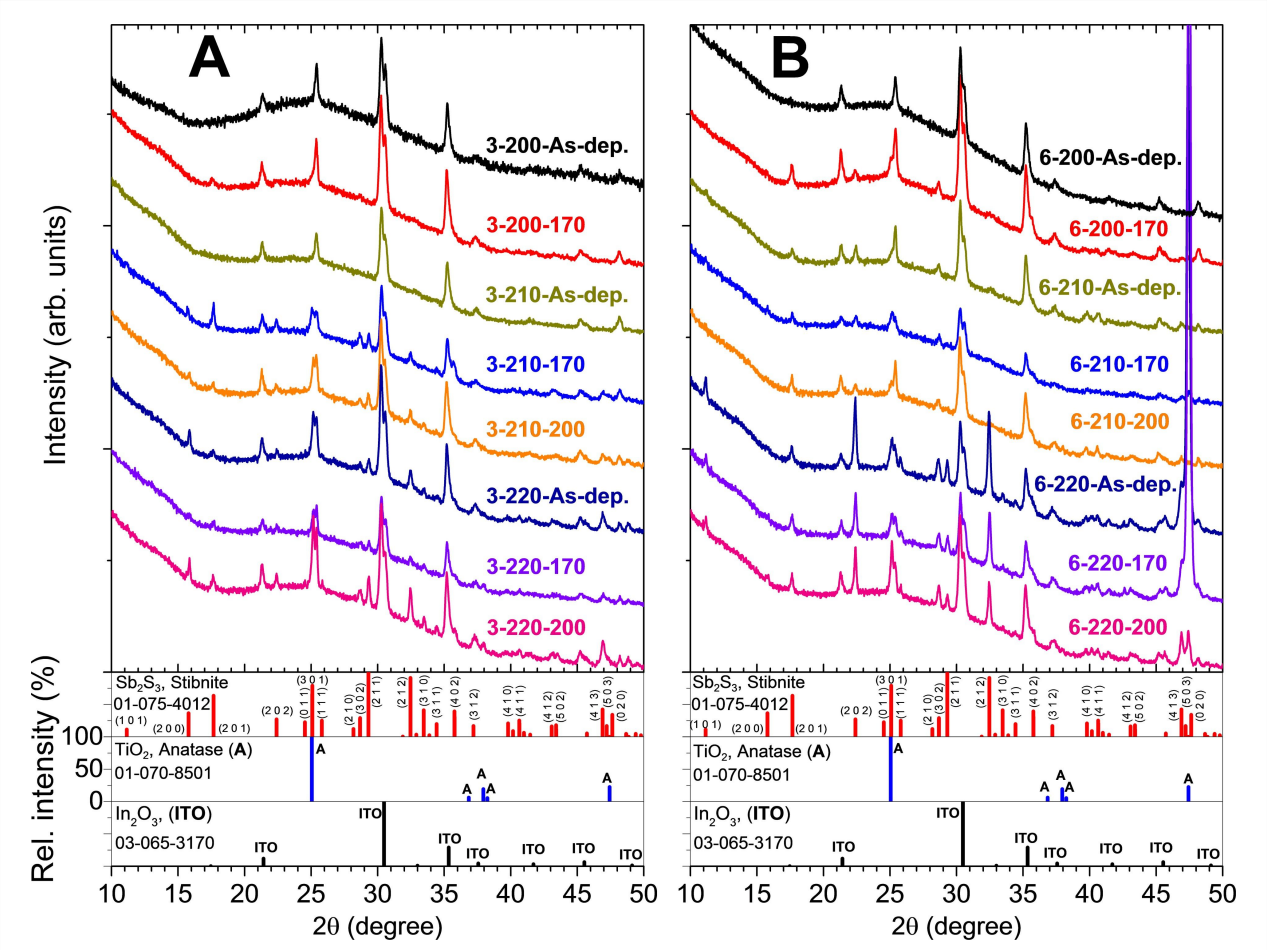

Figure 2: XRD patterns (shifted for visibility) of as-deposited and vacuum treated (170 °C or 200 °C, 5 minutes) Sb_2S_3 layers deposited on glass/ITO/TiO_2 substrate from Sb/S 1:3 (A) or 1:6 (B) solution at T_s = 200, 210, 220 °C. Sample names in figures: [S/Sb molar ratio in solution]-[deposition temperature]-[thermal treatment temperature].

mined mean unit cell volume (479 ± 4 Å^3) lies between the experimentally determined volume (486.7 Å^3) and the theoretically determined volume (470.5 Å^3) calculated from orthorhombic Sb_2S_3 powder (>99.99 wt %) data presented by Ibáñez et al. [20].

Sb_2S_3 layers deposited from Sb/S 1:6 solution at 210 °C (6-210-As-dep., Figure 2B) are polycrystalline, whereas layers deposited from Sb/S 1:3 solution (3-210-As-dep., Figure 2A) are XRD-amorphous. Sb_2S_3 layers deposited at 220 °C from both Sb/S 1:3 (3-220-As-dep., Figure 2A) and 1:6 (6-220-As-dep., Figure 2B) solution are polycrystalline. Several diffraction peaks corresponding to orthorhombic Sb_2S_3 were detected in these samples. No additional phases were detected by XRD in any studied samples. The presence or absence of amorphous Sb_2O_3 as a minor phase in the Sb_2S_3 layers, as it is difficult to ascertain by Raman or XRD analyses, has not been conclusively demonstrated.

The diffraction peak of the (2 0 0)/(0 0 2) plane of Sb_2S_3 is absent in most samples deposited from Sb/S 1:6 solution. Conversely, the diffraction peak of the (1 0 1) plane of Sb_2S_3 is absent in all samples deposited from Sb/S 1:3 solution. Sb_2S_3 crystallites in most of our samples have no preferred orientation. Only crystallites in as-deposited and vacuum treated (170 °C) samples deposited from Sb/S 1:6 solution (6-220-As-dep., 6-220-170, Figure 2B) show a preferred orientation parallel to the substrate surface along the (0 2 0) plane normal of Sb_2S_3. Interestingly, this preferred orientation of crystallites does not extend to the sample with Sb_2S_3 deposited in the same conditions, but thermally treated in vacuum at 200 °C (6-220-200, Figure 2B).

The larger crystallite size is a boon to the power conversion efficiency of all solar absorber materials because decreasing the amount of grain boundaries likely increases charge carrier mobility [26]. The crystallite sizes of as-deposited and thermally treated Sb_2S_3 layers are presented in Table 2. The effect of the deposition temperature is observed in Sb/S 1:3 Sb_2S_3 layers, as the crystallite size increases after vacuum annealing at 170 °C from 19 ± 8 nm to 100 ± 23 nm by raising T_D from 200 to 220 °C. The crystallite size in Sb/S 1:6 Sb_2S_3 layers (42 ± 15 nm) does not change significantly with T_D or vacuum treatment. Furthermore, vacuum treatment at 200 °C vs 170 °C does not substantially affect the crystallite size of Sb_2S_3 layers.

In comparison, the largest crystallites in Sb_2S_3 layers grown on TiO_2 substrates via CBD and annealed at 270 °C in N_2 for 30 min oriented along the (2 0 0) plane parallel to the substrate were 74 nm in size [16]. The crystallites oriented along the (2 0 1) plane were 24 nm in size in Sb_2S_3 layers grown on SnO_2/F (FTO) coated glass substrates via thermal evaporation [27]. The crystallite size was 52 nm along the (3 0 1) plane in Sb_2S_3 layers grown on glass substrates at 250 °C via spray pyrolysis [28], similar to the crystallite size in some of our samples. We conclude that the mean crystallite size in our Sb_2S_3 layers is in the general range of values obtained in the literature using both chemical and physical methods.

Morphology of as-deposited and thermally treated Sb_2S_3 layers

Influence of deposition temperature on morphology of Sb_2S_3 layers

The aim of this study was to obtain uniform Sb_2S_3 layers, which continuously coat the TiO_2 substrate. According to SEM surface studies, layers deposited from both Sb/S 1:3 and Sb/S 1:6 solutions at 200 and 210 °C (3-200-As-dep., 3-210-As-dep., Figure 3G,H, Supporting Information File 1, Figure S2A,B, Figure S3A,B; 6-200-As-dep., Figure 3A,B; 6-210-As-dep., Figure 3C,D) cover the substrate almost entirely. Grain boundaries and larger clusters of grains have formed in layers deposited from Sb/S 1:6 solutions for 40 minutes at 210 °C (6-210-As-dep., Figure 3C,D, Figure S5C,D). Cap-shaped islands (Ø 70 nm) in Sb_2S_3 layers deposited from Sb/S 1:6 solution at T_D = 210 °C for 20 minutes (Figure S4A,B), have grown (Ø 100 nm) and coalesced further after 40 minutes of deposition at 200–210 °C (6-200-As-dep., Figure 3A,B, Figure S5A,B; 6-210-As-dep., Figure 3C,D, Figure S5C,D, Figure

Table 2: Crystallite size (D) of as-deposited and vacuum treated Sb_2S_3 thin films. The crystallite size was calculated by the Scherrer equation from the (2 0 2) diffraction peak of as-deposited and vacuum treated (170 °C, 200 °C, 5 minutes) Sb_2S_3 thin films deposited on glass/ITO/TiO_2 substrates from Sb/S 1:3 and 1:6 precursor solution at T_D = 200, 210, 220 °C.

			D, nm			
Sb/S in sol.		1:3			1:6	
T_D, °C	200	210	220	200	210	220
as-dep.	amorph.	amorph.	33 ± 10	amorph.	39 ± 4	47 ± 1
vac. 170 °C	19 ± 8	38 ± 6	100 ± 23	37 ± 8	35 ± 4	49 ± 3
vac. 200 °C	no layer[a]	32 ± 8	67 ± 12	no layer[a]	45 ± 6	52 ± 3

[a]No Sb_2S_3 was detected by XRD or Raman.

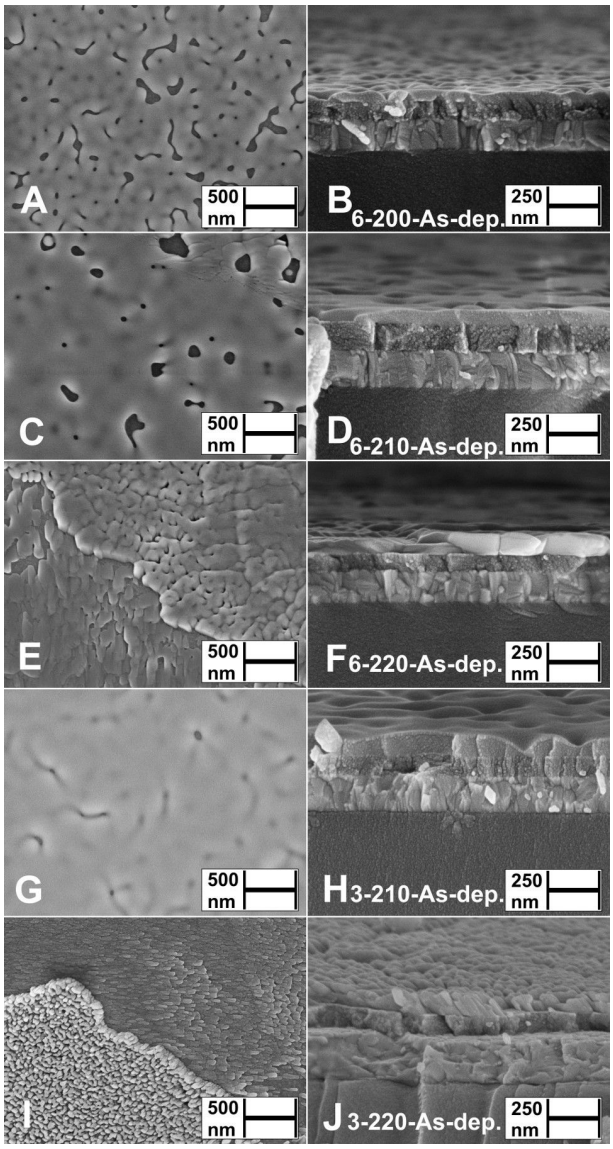

Figure 3: Surface and cross-sectional views by SEM study of as-deposited Sb_2S_3 layers deposited from Sb/S 1:6 solution at T_D = 200 °C (A, B), 210 °C (C, D) or 220 °C (E, F) and from Sb/S 1:3 solution at T_D = 210 °C (G, H) or 220 °C (I, J) on glass/ITO/TiO_2 substrate. Sample names in figures: [S/Sb molar ratio in solution]-[deposition temperature]-[as-deposited].

S6A,B), thereby covering the TiO_2 substrate to a greater extent. The layers deposited from Sb/S 1:6 solution at 220 °C for 40 minutes (6-220-As-dep., Figure 3E,F, Figure S5E,F) consist of various agglomerates, separated by pinholes, and grains flowing randomly along the partially exposed TiO_2 substrate (lower left, Figure 3E).

Increasing the deposition temperature from 210 to 220 °C significantly transforms the surface morphology in Sb/S 1:3 layers, as instead of the planar grains (3-210-As-dep., Figure 3G,H) domains of elongated rod-shaped grains (length ≈ 100 nm) appear either upright or sideways on the substrate (3-220-As-dep., Figure 3I,J, Figure S3C,D). Rod-shaped Sb_2S_3 grains were able to grow due to the nature of the material as well as due to complex interactions between the substrate and the turbulence of the spray during deposition [29].

Increasing the sulfur precursor concentration in the spray solution from Sb/S 1:3 to 1:6 (and deposition time from 20 to 40 minutes) yields Sb_2S_3 layers consisting of agglomerated grains (6-220-As-dep., Figure 3E,F). As the deposition time was simultaneously increased from 20 to 40 minutes, it is uncertain whether the morphology of the Sb_2S_3 layers is affected more by the Sb/S molar ratio in solution or by the deposition time. Sb_2S_3 tends to yield different morphologies in similar deposition conditions, possibly due to liquid phase reactions between molten-boiling $SbCl_3$ (mp 73.4 °C, bp 223.5 °C [30]) and molten thiourea (TU, mp 182 °C [14,15]) catalyzed by the highly active surface of the TiO_2 substrate [31].

We have consistently observed twice slower growth of Sb_2S_3 by spraying solutions with Sb/S 1:6 (Supporting Information File 1, Figure S4A,B) vs Sb/S 1:3 (Figure 3G,H) molar ratio at 200–220 °C. We speculate that doubling the concentration of TU could sterically inhibit the formation of solid Sb_2S_3 nuclei on the surface of the active TiO_2 substrate due to more intense bubbling of volatile TU decomposition products (CS_2, NH_3, HCN, COS, SO_2, HCl, HNCS at 200–220 °C in air based on decomposition studies of pure TU [14], $Cu(TU)_3Cl$ [32], $Zn(TU)_2Cl_2$ [33], and $Sn(TU)_2Cl_2$ [34]) in the surrounding liquid phase.

In summary, the most uniform and continuous Sb_2S_3 thin films were deposited from Sb/S 1:3 solution at 200–210 °C.

Influence of vacuum treatment temperature on morphology of Sb_2S_3 layers

The thermal treatment of X-ray amorphous Sb_2S_3 layers (6-200-As-dep., Figure 3A,B; 3-200-As-dep.; 3-210-As-dep., Figure 3G,H, Supporting Information File 1, Figure S2A,B) in vacuum at 170 °C for 5 minutes yields enhanced substrate coverage at the expense of decreased layer thickness due to coalescence of grains and film formation (6-200-170, Figure 4A,B; 3-200-170, Figure 4G,H; 3-210-170, Figure 4I,J). Complete substrate coverage is observed in the Sb_2S_3 layers deposited at 210 °C from Sb/S 1:3 solution as coalescence is facilitated during treatment in vacuum at 170 °C due to the near-continuous coverage of the TiO_2 substrate in the as-deposited layers (3-210-170, Figure 4G,H, Figure S2C,D, Figure S7A,B).

Planar grain agglomerates in thermally treated Sb_2S_3 layers (3-210-170, Figure 4G,H, Supporting Information File 1, Figure

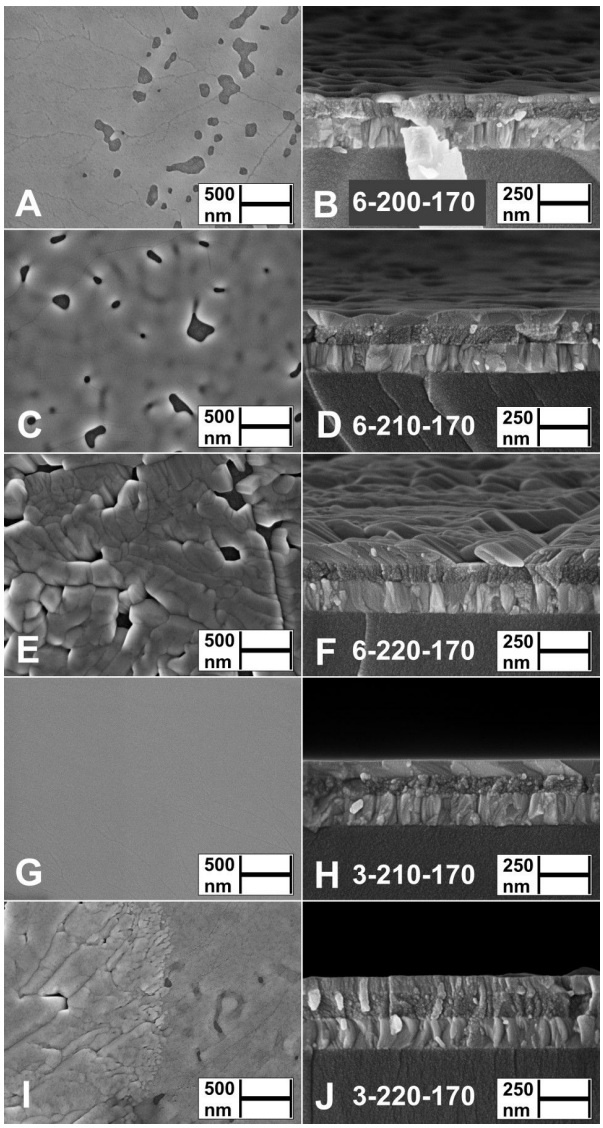

Figure 4: Surface and cross-sectional views by SEM study of thermally treated (170 °C, 5 minutes) Sb_2S_3 layers deposited from Sb/S 1:6 solution at T_D = 200 °C (A, B), 210 °C (C, D) or 220 °C (E, F) and from Sb/S 1:3 solution at T_D = 210 °C (G, H) or 220 °C (I, J) on glass/ITO/TiO_2 substrates. Sample names in figures: [S/Sb molar ratio in solution]-[deposition temperature]-[thermal treatment temperature].

S7A,B; 6-200-170, Figure 4A,B, Figure S9A,B; 6-210-170, Figure 4C,D, Figure S9C,D) range from 100 nm to over 10 μm in size. These agglomerates, consisting of smaller grains separated by ridges, resemble the surface morphology of 300 nm thick polycrystalline Sb_2S_3 films grown via thermal evaporation and annealed for 10 min at 300 °C in N_2 [35], and that of metal halide perovskites obtained by Volmer–Weber growth via hot casting [36]. The layers deposited at 220 °C from both Sb/S 1:3 and Sb/S 1:6 solutions, and thermally treated at 170 °C, consist of numerous grains and pinholes (3-220-170, Figure 4I,J; 6-220-170, Figure 4E,F).

Sb_2S_3 layers deposited at 210 °C from both Sb/S 1:3 and Sb/S 1:6 solutions, and thermally treated in vacuum at 200 °C (3-210-200, Figure 5A,B, Supporting Information File 1, Figure S8A,C,E; 6-210-200, Figure 5C,D, Figure S8B,D,F), are porous, inhomogeneous and ≈20 nm thinner (Table 3) vs the uniform in thickness layers after treatment at 170 °C (3-210-170, Figure 4I,J; 6-210-170, Figure 4C,D).

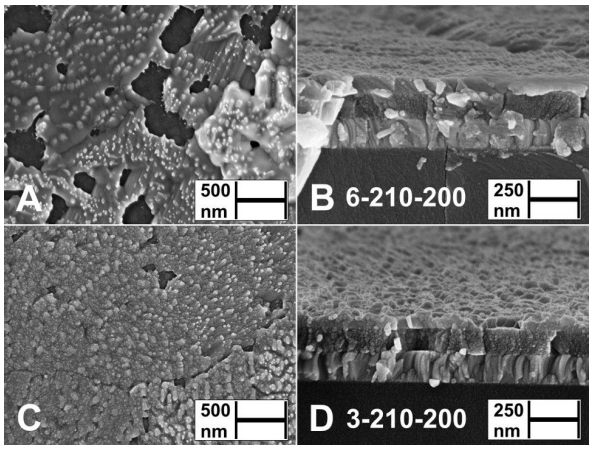

Figure 5: Surface and cross-sectional views by SEM study of vacuum treated (200 °C, 5 minutes) Sb_2S_3 layers deposited from Sb/S 1:6 solution (A, B) and from Sb/S 1:3 solution (C, D) at T_D = 210 °C on glass/ITO/TiO_2 substrates. Sample names in figures: [S/Sb molar ratio in solution]-[deposition temperature]-[thermal treatment temperature].

Table 3: Thicknesses of Sb_2S_3 layers estimated from SEM images.

	Sb_2S_3 layer thickness, nm					
	Sb/S 1:3 in sol., 20 min dep.			Sb/S 1:6 in sol., 40 min dep.		
T_D, °C	200	210	220	200	210	220
as-dep.	70–90	80–100	60/150[a]	50–70	60/400[a]	40/400[a]
vac., 170 °C	70–90	70–90	80/150[a]	30–40	60/400[a]	40/400[a]
vac., 200 °C	no layer[b]	60–70	N/A	no layer[b]	60–70	N/A

[a]Thickness of formations shown in the Supporting Information File 1 in Figures S5, S7, S8 and S9. [b]No Sb_2S_3 was detected by XRD or Raman.

The decreasing layer thickness indicates that approximately a quarter of Sb_2S_3 by volume has either evaporated or sublimated, i.e., volatilized. Incongruent evaporation, i.e., depletion of sulfur in Sb_2S_3 during evaporation, may cause the change in Sb_2S_3 layer morphology, as volatilization of the planar regions around the nucleating islands has been reported during thermal treatment of both Sb_2Se_3 layers grown via thermal evaporation [37] and oxide containing Sb_2S_3 layers grown via CBD [16].

The calculated vapor pressure of Sb_2S_3 is ≈2×10^{-10} Torr at 170 °C, 7×10^{-9} Torr at 200 °C and 9×10^{-7} Torr at 250 °C [38], whereas the dynamic system pressure is ≈4×10^{-6} Torr. The calculated partial pressure of Sb_2S_3 is ≈0.0050% at 170 °C, 0.18% at 200 °C and 23% at 250 °C (Comment S1 in Supporting Information File 1). The loss of a quarter of the Sb_2S_3 layer thickness in samples that were vacuum annealed at 200 vs 170 °C (Table 3) correlates with the exponential increase in Sb_2S_3 vapor pressure in the 170–250 °C range.

In conclusion, the most uniform and continuous Sb_2S_3 thin films were produced by vacuum treatment at 170 °C for 5 min of Sb_2S_3 layers deposited from Sb/S 1:3 solution at 200–210 °C.

Elemental composition of as-deposited and thermally treated Sb_2S_3 layers

The elemental composition of Sb_2S_3 in as-deposited and thermally treated glass/ITO/TiO_2/Sb_2S_3 samples was determined using energy dispersive X-ray spectroscopy (EDX). The EDX results of studied Sb_2S_3 layers in terms of S to Sb atomic ratio (S/Sb) are presented in Table 4. S/Sb in both as-deposited and vacuum annealed polycrystalline Sb_2S_3 layers deposited at T_D = 220 °C is close to the stoichiometric value of 1.5 of Sb_2S_3, whereas the S/Sb ratio of as-deposited and thermally treated Sb_2S_3 layers (Sb/S 1:3 in solution, T_D 200–210 °C, 3-200-As-dep., 3-210-As-dep., 3-200-170, 3-210-170) is ≈1.3. S/Sb is ≈1.5–1.6 in layers deposited from Sb/S 1:6 solution at 200–220 °C.

Table 4: S/Sb atomic ratio of as-deposited and thermally treated Sb_2S_3 layers calculated from EDX data.

	S/Sb in layer					
Sb/S in sol.	1:3			1:6		
T_D, °C	200	210	220	200	210	220
as-dep.	1.3	1.3	1.5	1.6	1.5	1.5
vac., 170 °C	1.3	1.3	1.5	1.6	1.6	1.5
vac., 200 °C	N/A	1.4	N/A	N/A	1.5	N/A

We note that interpretation of EDX spectra of very thin layers is difficult. Most of our Sb_2S_3 layers are thinner than 100 nm, which could explain the divergence in the elemental composition of our Sb_2S_3 layers. Therefore, future studies by more surface sensitive methods are required. Overall, S/Sb in most studied samples approximates the stoichiometric value of 1.5 of Sb_2S_3.

Oxygen could not be quantified by EDX due to the thin layers and high concentration of O in the glass/ITO/TiO_2 substrate. In addition, C and Cl levels were below the detection limit of the used EDX setup in all studied Sb_2S_3 layers, meaning most C and Cl species exit the growing Sb_2S_3 layer during deposition in open environment (Supporting Information File 1, Figure S11). We believe that this reinforces our claim that formation of Sb_2S_3 proceeds through a molten phase reaction between $SbCl_3$ and TU, where the denser (4562 kg/m^3 [39]) Sb_2S_3 precipitates and nucleates, while the remainder of the volatile compounds ($SbCl_3$, and various decomposition products of TU) exit the system [14,15,38,40].

Growth mechanism of Sb_2S_3 layers by spray pyrolysis

The three most common growth mechanisms of solids can be described by the following equations [41]:

$$\sigma_{SG} > \sigma_{LG} + \sigma_{SL} \quad (1)$$

$$\sigma_{SG} < \sigma_{LG} + \sigma_{SL} \quad (2)$$

$$\sigma_{SG} \approx \sigma_{LG} + \sigma_{SL} \quad (3)$$

Where σ_{SG} is the surface free energy of the substrate–gas interface (TiO_2–air), σ_{LG} is the surface free energy of the layer–gas interface (Sb_2S_3–air) and σ_{SL} is the surface free energy of the substrate–layer interface (TiO_2–Sb_2S_3). The surface free energy (σ) is the driving force of fluids and solids to seek a condition of minimum energy by contracting interfacial surface area [41]. Separate 3D islands grow if Equation 1 is valid, a.k.a. Volmer–Weber growth; 2D layer-by-layer growth occurs if Equation 2 is valid, a.k.a. Frank–Van der Merwe growth; combined 2D layer-by layer and 3D island growth occurs if Equation 3 is valid, a.k.a. Stranski–Krastanov growth [36,41-43].

Furthermore, SEM surface studies show cap-shaped islands indicative of Volmer–Weber growth in Sb_2S_3 layers deposited on Si/SiO_2 alternative substrates by ultrasonic spraying (Supporting Information File 1, Figure S10A,B). Metastibnite-Sb_2S_3 forms when formation of stibnite-Sb_2S_3 is halted by insufficient reaction time and energy [44-46]. Volmer–Weber island growth of amorphous Sb_2S_3 (and in some cases leaf-like grains of polycrystalline Sb_2S_3) have been observed in Sb_2S_3 layers

grown by chemical bath deposition on glass [47,48], In_2O_3/Sn (ITO) [49], planar TiO_2 [16] and TiO_2 nanotube arrays [50], by sequential deposition [51] and spin coating [8,52] on planar TiO_2, by photochemical deposition on mesoporous TiO_2 [53], by thermal evaporation on planar CdS [27] and planar TiO_2 [54]. Supported by these numerous observations, we consider the Volmer–Weber growth characteristic of Sb_2S_3, given that the substrate and deposition conditions are met. Indeed, metastibnite, the naturally occurring mineral form of amorphous Sb_2S_3, has the botryoidal characteristic, preferentially forming globular clusters [55]. We have also observed 3D growth of extremely thin TiO_2 layers by spray pyrolysis [56]. Therefore, 3D island growth may partially be imposed by the use of the spray pyrolysis method as well.

Based on the above observations, the morphology and crystallinity of as-deposited layers seems to determine the nature of Sb_2S_3 layer morphology as formed during vacuum thermal treatment. Our proposed growth mechanism of Sb_2S_3 by ultrasonic spraying in air is illustrated in Figure 6.

Optical properties of as-deposited and thermally treated Sb_2S_3 layers

The absorption coefficient (α) and band gap (E_g) values of Sb_2S_3 in both as-deposited and thermally treated glass/ITO/TiO_2/Sb_2S_3 samples were determined using an approximated Sb_2S_3 layer thickness of 100 nm derived from SEM images (Table 3). The absorption coefficient α was determined as

$$\alpha = d^{-1} \ln\left[(1-R)T^{-1}\right], \quad (4)$$

where d is the layer thickness, R is the total reflectance, included to compensate for thin film interference, and T is the total transmittance.

The band gap of Sb_2S_3 layers was determined by plotting $(\alpha h\nu)^{1/r}$ vs $h\nu$, where h is the Planck constant, ν is the frequency and $r = 1/2$ is the exponent corresponding to the assumed direct optical transition [57]. Extrapolating the linear region of this curve to the $h\nu$-axis yields the optical band gap. Thin film interference could not be completely removed by accounting for reflectance in α calculations. Thus, the absolute values of α may deviate from the expected values with the uncertainty introduced by using a constant layer thickness in calculations.

The α vs wavelength plots of samples, which contain as-deposited or vacuum-treated Sb_2S_3 layers deposited from Sb/S 1:3 solution, are shown in Figure 7A. Likewise, α vs wavelength plots of Sb/S 1:6 samples are shown in Figure 7B. The α in samples containing amorphous Sb_2S_3 increases steadily from 10^3–10^4 cm^{-1} at 600–800 nm to 10^5 cm^{-1} at around 400 nm. The α increases significantly faster in samples containing as-grown crystalline Sb_2S_3 or vacuum crystallized Sb_2S_3. The value of α surges by an order of magnitude from around 10^4 cm^{-1} to 10^5 cm^{-1} as the wavelength decreases from 750 nm to 650 nm due to the onset of absorption in crystalline Sb_2S_3. At shorter wavelengths beyond the absorption edge, α increases at a slower rate, from around 10^5 cm^{-1} at 650 nm to more than 5×10^5 cm^{-1} at 300 nm. The optical absorption results are in agreement with XRD, which shows that these samples (3-220-As-dep., 3-210-170, 6-210-As-dep. and 6-200-170) contain orthorhombic Sb_2S_3 (Figure 2A,B). Comparing the α spectra of samples containing amorphous and crystalline

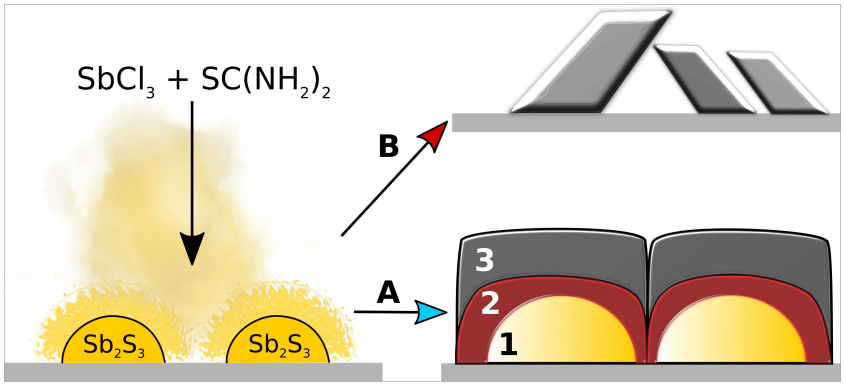

Figure 6: Proposed growth mechanism paths of Sb_2S_3 by Volmer–Weber growth during ultrasonic spraying of methanolic solution of $SbCl_3$–$SC(NH_2)_2$ in excess of sulfur precursor in aerosol. Amorphous Sb_2S_3 nucleates after precipitation from a molten $SbCl_3$–$SC(NH_2)_2$ mixture: A – Amorphous Sb_2S_3 islands nucleate on the rigid TiO_2 substrate and grow by 3D Volmer–Weber growth, surrounded by a protective bubbling liquid film of volatile $SbCl_3$ and TU decomposition products (1), eventually interconnecting by coalescence of sufficiently large islands to minimize Sb_2S_3–air interfacial free surface energy (2), and form grain boundaries during crystallization in vacuum or inert environment (3). B – Sb_2S_3 crystallizes into separate grains if either the deposition temperature, the deposition time or the excess of TU in Sb/S precursor molar ratio exceed a critical value before or during process A, i.e., the energetic threshold for crystallization is surpassed.

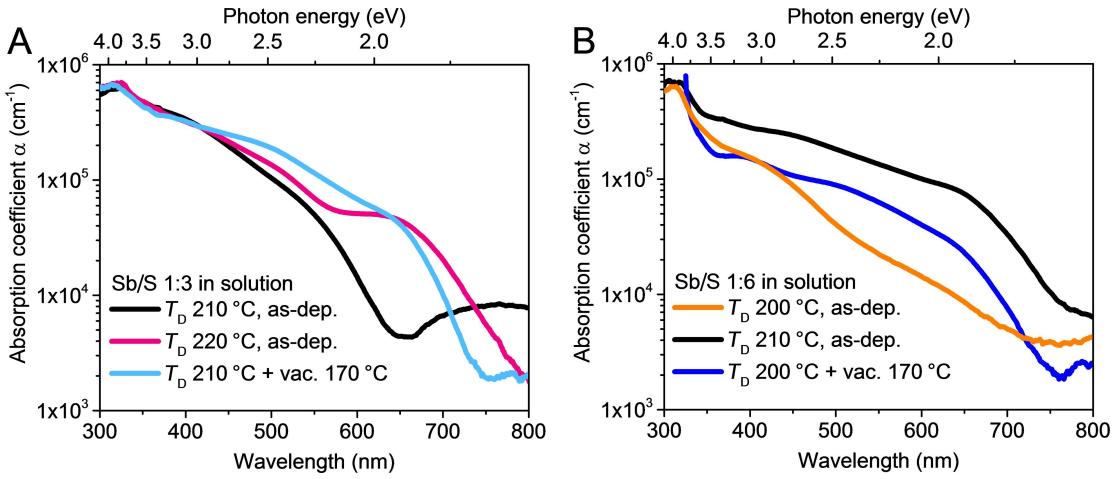

Figure 7: Absorption coefficient (α) vs wavelength of glass/ITO/TiO_2/Sb_2S_3 samples incorporating as-deposited and vacuum treated (170 °C, 5 minutes) Sb_2S_3 layers. The α of glass/ITO/TiO_2 substrates is not shown as it is negligible at the presented wavelengths. Sb_2S_3 layers were deposited from Sb/S 1:3 solution at 210 °C, 220 °C (A) and from Sb/S 1:6 solution at 200 °C and 210 °C (B).

Sb_2S_3 further confirms that the Sb_2S_3 layers deposited from Sb/S 1:3 solution at 200–210 °C, and from Sb/S 1:6 solution at 200 °C, are indeed amorphous. Namely, α is an order of magnitude smaller at around 600 nm in samples containing amorphous Sb_2S_3 layers (3-210-As-dep. and 6-200-As-dep.).

The experimentally determined E_g are ≈2.7 and 1.8 eV for amorphous and polycrystalline Sb_2S_3, respectively (Table 5, Tauc plots in Supporting Information File 1, Figure S12). In comparison, E_g of amorphous CBD-Sb_2S_3 on glass substrates is ≈2.5 eV [58] and E_g of polycrystalline Sb_2S_3 prepared by physical and chemical methods is commonly reported as 1.6–1.8 eV [1,22,58-60]. As such, we find the E_g of our polycrystalline Sb_2S_3 layers lies satisfactorily in the range of published values.

Table 5: Band gap (E_g) of as-deposited and thermally treated Sb_2S_3 layers, as estimated assuming direct optical transition and Tauc plots[a] of optical transmittance spectra of glass/ITO/TiO_2/Sb_2S_3 samples.

	E_g, eV					
Sb/S in sol.	1:3			1:6		
T_D, °C	200	210	220	200	210	220
as-dep.	2.6	2.7	1.8	2.7	1.8	1.8
vac. 170 °C	1.8	1.8	1.8	1.8	1.8	1.8
vac. 200 °C	no layer[b]	1.8	1.8	no layer[b]	1.8	1.8

[a]Supporting Information File 1, Figure S12A,B. [b]No Sb_2S_3 was detected by XRD or Raman.

Conclusion

The structure, the morphology, and the optical properties of Sb_2S_3 layers could be controlled by varying the spray deposition temperature and the molar ratio of precursors in spray solution. Nonuniform, discontinuous layers of polycrystalline Sb_2S_3 (E_g 1.8 eV) were deposited by ultrasonic spray pyrolysis of $SbCl_3$/$SC(NH_2)_2$ 1:3 solution at $T_D \geq 220$ °C or 1:6 solution at $T_D \geq 210$ °C on glass/ITO/TiO_2 substrates in air. Increasing the concentration of the sulfur precursor in spray solution from Sb/S 1:3 to 1:6 reduced the crystallization temperature of Sb_2S_3 layers by ≈10 °C. Uniform layers of amorphous Sb_2S_3 ($E_g \approx 2.7$ eV, S/Sb 1:3) were deposited on glass/ITO/TiO_2 substrates in air by ultrasonic spray pyrolysis of Sb/S 1:3 solution at T_D = 200–210 °C. High quality, uniform, pinhole-free coatings of polycrystalline orthorhombic Sb_2S_3 (E_g 1.8 eV, S/Sb 1.3) with lateral grain size as large as 10 μm were produced by crystallization of amorphous Sb_2S_3 layers in vacuum at 170 °C for 5 minutes. Such Sb_2S_3 optical coatings are very attractive for future application as low-cost absorber layers in solar cells.

Experimental

Materials

Commercial 1.1 mm thick soda-lime glass coated with 150 nm 25 $\Omega \cdot sq^{-1}$ tin doped indium oxide (ITO) from ZSW was used as a substrate. The substrates were rinsed with deionized water, methanol (99.9 vol %), deionized water, dipped in aqueous room temperature H_2SO_4 (1 vol %), rinsed again with deionized water, and dried at 105 °C in air.

TiO_2 was prepared by methods used in our previous papers [7,12]. The TiO_2 film thickness was ≈80 nm based on SEM images. The Sb_2S_3 layers were deposited from 30 mM $SbCl_3$ (99 wt %) and $SC(NH_2)_2$ (99 wt %) methanolic (99.9 vol %)

solutions at molar ratios of Sb/S 1:3 and Sb/S 1:6. All chemicals were purchased from Sigma-Aldrich and used without any additional processing. The precursor solutions were prepared inside a glovebox with controlled humidity (<14 ppm).

The solutions were ultrasonically nebulized and guided by compressed air at a flow rate of 5 $L \cdot min^{-1}$ onto glass/ITO/TiO_2 substrates at deposition temperatures of 200, 210, and 220 °C for 20 min (Sb/S 1:3) or 40 min (Sb/S 1:6). After deposition, some of the samples were thermally treated in dynamic vacuum (<4×10^{-6} Torr) at 170, 200 or 250 °C for 5 min. The average heating and cooling rate was ≈8 $°C \cdot min^{-1}$.

Characterization

The elemental composition of the films was determined by energy dispersive X-ray spectroscopy (EDX) using a Bruker spectrometer with ESPRIT 1.8 system at the Zeiss HR FESEM Ultra 55 scanning electron microscope (SEM) operating at an accelerating voltage of 7 kV. The surface and cross-sectional morphologies of the layers were recorded by the same SEM system at an electron beam accelerating voltage of 4 kV.

Unpolarized micro-Raman measurements were conducted at room temperature using a Horiba Jobin Yvon Labram HR 800 spectrometer in backscattering geometry. The laser intensity was attenuated to ca. 143 $\mu W \cdot \mu m^{-2}$ over a focal area of Ø 5 µm to prevent oxidation of the Sb_2S_3 layers, a common oversight according to Kharbish et al. [21]. Deconvoluted band centers in Raman shift, band intensities and full widths at half maximum (FWHM) were fitted using a Lorentzian function [61].

X-ray diffraction (XRD) patterns were recorded on a Rigaku Ultima IV powder diffractometer in θ-2θ mode (Cu $K\alpha_1$ λ = 1.5406 Å, 40 kV, 40 mA, step 0.02°, 5°/min, silicon strip detector D/teX Ultra). The crystal structure and phase composition were analyzed using Rigaku PDXL 2 software.

Optical total transmittance and total reflectance spectra of glass/ITO/TiO_2 reference and glass/ITO/TiO_2/Sb_2S_3 samples were measured in the 250–1600 nm range vs air as a reference using a Jasco V-670 UV-VIS-NIR spectrophotometer equipped with a 40 mm integrating sphere and Spectra Manager II software.

Supporting Information

Supporting Information File 1

Additional XRD, EDX data, SEM images, Lorentzian fitting of Sb_2S_3 Raman vibrational bands, and Tauc plots.
[https://www.beilstein-journals.org/bjnano/content/supplementary/2190-4286-10-18-S1.pdf]

Acknowledgements

We acknowledge Dr. Valdek Mikli from the Laboratory of Optoelectronic Materials Physics at Tallinn University of Technology for recording SEM images and EDX measurements, Estonian Research Council project IUT19-4 “Thin films and nanomaterials by wet-chemical methods for next-generation photovoltaics” and European Regional Development Fund project TK141 “Advanced materials and high-technology devices for sustainable energetics, sensorics and nanoelectronics” for funding.

ORCID® iDs

Jako S. Eensalu - https://orcid.org/0000-0002-4312-0227
Atanas Katerski - https://orcid.org/0000-0003-1980-3391
Erki Kärber - https://orcid.org/0000-0001-6157-3070
Ilona Oja Acik - https://orcid.org/0000-0002-1870-3543
Arvo Mere - https://orcid.org/0000-0001-9070-3970
Malle Krunks - https://orcid.org/0000-0003-4658-4403

References

1. Versavel, M. Y.; Haber, J. A. *Thin Solid Films* **2007,** *515,* 7171–7176. doi:10.1016/j.tsf.2007.03.043
2. Messina, S.; Nair, M. T. S.; Nair, P. K. *Thin Solid Films* **2007,** *515,* 5777–5782. doi:10.1016/j.tsf.2006.12.155
3. Itzhaik, Y.; Niitsoo, O.; Page, M.; Hodes, G. *J. Phys. Chem. C* **2009,** *113,* 4254–4256. doi:10.1021/jp900302b
4. Choi, Y. C.; Lee, D. U.; Noh, J. H.; Kim, E. K.; Seok, S. I. *Adv. Funct. Mater.* **2014,** *24,* 3587–3592. doi:10.1002/adfm.201304238
5. Choi, Y. C.; Seok, S. I. *Adv. Funct. Mater.* **2015,** *25,* 2892–2898. doi:10.1002/adfm.201500296
6. Wedemeyer, H.; Michels, J.; Chmielowski, R.; Bourdais, S.; Muto, T.; Sugiura, M.; Dennler, G.; Bachmann, J. *Energy Environ. Sci.* **2013,** *6,* 67–71. doi:10.1039/c2ee23205g
7. Parize, R.; Katerski, A.; Gromyko, I.; Rapenne, L.; Roussel, H.; Kärber, E.; Appert, E.; Krunks, M.; Consonni, V. *J. Phys. Chem. C* **2017,** *121,* 9672–9680. doi:10.1021/acs.jpcc.7b00178
8. Sung, S.-J.; Gil, E. K.; Lee, S.-J.; Choi, Y. C.; Yang, K.-J.; Kang, J.-K.; Cho, K. Y.; Kim, D.-H. *J. Ind. Eng. Chem. (Amsterdam, Neth.)* **2017,** *56,* 196–202. doi:10.1016/j.jiec.2017.07.012
9. Patil, P. S. *Mater. Chem. Phys.* **1999,** *59,* 185–198. doi:10.1016/s0254-0584(99)00049-8
10. Kriisa, M.; Krunks, M.; Oja Acik, I.; Kärber, E.; Mikli, V. *Mater. Sci. Semicond. Process.* **2015,** *40,* 867–872. doi:10.1016/j.mssp.2015.07.049
11. Rajpure, K. Y.; Bhosale, C. H. *Mater. Chem. Phys.* **2002,** *73,* 6–12. doi:10.1016/s0254-0584(01)00350-9
12. Kärber, E.; Katerski, A.; Oja Acik, I.; Mere, A.; Mikli, V.; Krunks, M. *Beilstein J. Nanotechnol.* **2016,** *7,* 1662–1673. doi:10.3762/bjnano.7.158
13. Kim, D.-H.; Lee, S.-J.; Park, M. S.; Kang, J.-K.; Heo, J. H.; Im, S. H.; Sung, S.-J. *Nanoscale* **2014,** *6,* 14549–14554. doi:10.1039/c4nr04148h
14. Madarász, J.; Pokol, G. *J. Therm. Anal. Calorim.* **2007,** *88,* 329–336. doi:10.1007/s10973-006-8058-4
15. Timchenko, V. P.; Novozhilov, A. L.; Slepysheva, O. A. *Russ. J. Gen. Chem.* **2004,** *74,* 1046–1050. doi:10.1023/b:rugc.0000045862.69442.aa

16. Parize, R.; Cossuet, T.; Chaix-Pluchery, O.; Roussel, H.; Appert, E.; Consonni, V. *Mater. Des.* **2017,** *121,* 1–10. doi:10.1016/j.matdes.2017.02.034
17. Chang, H.; Huang, P. J. *J. Raman Spectrosc.* **1998,** *29,* 97–102. doi:10.1002/(sici)1097-4555(199802)29:2<97::aid-jrs198>3.0.co;2-e
18. Liu, Y.; Eddie Chua, K. T.; Sum, T. C.; Gan, C. K. *Phys. Chem. Chem. Phys.* **2014,** *16,* 345–350. doi:10.1039/c3cp53879f
19. Makreski, P.; Petruševski, G.; Ugarković, S.; Jovanovski, G. *Vib. Spectrosc.* **2013,** *68,* 177–182. doi:10.1016/j.vibspec.2013.07.007
20. Ibáñez, J.; Sans, J. A.; Popescu, C.; López-Vidrier, J.; Elvira-Betanzos, J. J.; Cuenca-Gotor, V. P.; Gomis, O.; Manjón, F. J.; Rodríguez-Hernández, P.; Muñoz, A. *J. Phys. Chem. C* **2016,** *120,* 10547–10558. doi:10.1021/acs.jpcc.6b01276
21. Kharbish, S.; Libowitzky, E.; Beran, A. *Eur. J. Mineral.* **2009,** *21,* 325–333. doi:10.1127/0935-1221/2009/0021-1914
22. Medles, M.; Benramdane, N.; Bouzidi, A.; Sahraoui, K.; Miloua, R.; Desfeux, R.; Mathieu, C. *J. Optoelectron. Adv. Mater.* **2014,** *16,* 726–731. https://joam.inoe.ro/index.php?option=magazine&op=view&idu=3498&catid=84
23. Nakamoto, K. *Infrared and Raman Spectra of Inorganic and Coordination Compounds,* 6th ed.; Wiley-Blackwell: São Paulo, Brazil, 2008. doi:10.1002/9780470405888
24. Hofmann, W. *Z. Kristallogr.* **1933,** *86,* 225–245. doi:10.1524/zkri.1933.86.1.225
25. Petzelt, J.; Grigas, J. *Ferroelectrics* **1973,** *5,* 59–68. doi:10.1080/00150197308235780
26. Grovenor, C. R. M. *J. Phys. C: Solid State Phys.* **1985,** *18,* 4079–4119. doi:10.1088/0022-3719/18/21/008
27. Escorcia-García, J.; Becerra, D.; Nair, M. T. S.; Nair, P. K. *Thin Solid Films* **2014,** *569,* 28–34. doi:10.1016/j.tsf.2014.08.024
28. Boughalmi, R.; Boukhachem, A.; Kahlaoui, M.; Maghraoui, H.; Amlouk, M. *Mater. Sci. Semicond. Process.* **2014,** *26,* 593–602. doi:10.1016/j.mssp.2014.05.059
29. Birkholz, M.; Selle, B.; Fuhs, W.; Christiansen, S.; Strunk, H. P.; Reich, R. *Phys. Rev. B* **2001,** *64,* 085402. doi:10.1103/physrevb.64.085402
30. Greenwood, N. N.; Earnshaw, A. *Chemistry of the Elements,* 2nd ed.; Butterworth-Heinemann: Oxford, United Kingdom, 1997. doi:10.1016/c2009-0-30414-6
31. Fujishima, A.; Zhang, X.; Tryk, D. A. *Surf. Sci. Rep.* **2008,** *63,* 515–582. doi:10.1016/j.surfrep.2008.10.001
32. Madarász, J.; Krunks, M.; Niinistö, L.; Pokol, G. *J. Therm. Anal. Calorim.* **2015,** *120,* 189–199. doi:10.1007/s10973-015-4481-8
33. Madarász, J.; Krunks, M.; Niinistö, L.; Pokol, G. *J. Therm. Anal. Calorim.* **2004,** *78,* 679–686. doi:10.1023/b:jtan.0000046127.69336.90
34. Polivtseva, S.; Oja Acik, I.; Krunks, M.; Tõnsuaadu, K.; Mere, A. *J. Therm. Anal. Calorim.* **2015,** *121,* 177–185. doi:10.1007/s10973-015-4580-6
35. Lan, C.; Liang, G.; Lan, H.; Peng, H.; Su, Z.; Zhang, D.; Sun, H.; Luo, J.; Fan, P. *Phys. Status Solidi RRL* **2018,** *12,* 1800025. doi:10.1002/pssr.201800025
36. Zheng, Y. C.; Yang, S.; Chen, X.; Chen, Y.; Hou, Y.; Yang, H. G. *Chem. Mater.* **2015,** *27,* 5116–5121. doi:10.1021/acs.chemmater.5b01924
37. Kushkhov, A. R.; Gaev, D. S.; Rabinovich, O. I.; Stolyarov, A. G. *Crystallogr. Rep.* **2013,** *58,* 365–369. doi:10.1134/s1063774513020132
38. Piacente, V.; Scardala, P.; Ferro, D. *J. Alloys Compd.* **1992,** *178,* 101–115. doi:10.1016/0925-8388(92)90251-4
39. Lide, D. R., Ed. *CRC Handbook of Chemistry and Physics,* 87th ed.; CRC Press: Boca Raton, FL, U.S.A., 2006.
40. Ozturk, I. I.; Kourkoumelis, N.; Hadjikakou, S. K.; Manos, M. J.; Tasiopoulos, A. J.; Butler, I. S.; Balzarini, J.; Hadjiliadis, N. *J. Coord. Chem.* **2011,** *64,* 3859–3871. doi:10.1080/00958972.2011.633603
41. Rohrer, G. S. *Metall. Mater. Trans. A* **2010,** *41,* 1063–1100. doi:10.1007/s11661-010-0215-5
42. Volmer, M.; Weber, A. *Z. Phys. Chem., Stoechiom. Verwandtschaftsl.* **1926,** *119,* 277–301. doi:10.1515/zpch-1926-11927
43. Abraham, D. B.; Newman, C. M. *EPL* **2009,** *86,* 16002–16007. doi:10.1209/0295-5075/86/16002
44. Ostwald, W. *The Principles of Inorganic Chemistry,* 2nd ed.; Macmillan and Co., Ltd.: London, United Kingdom, 1904.
45. Brookins, D. G. *Econ. Geol.* **1972,** *67,* 369–372. doi:10.2113/gsecongeo.67.3.369
46. Clouet, E. Modeling of Nucleation Processes. In *ASM Handbook, Fundamentals of Modeling for Metals Processing;* Furrer, D. U.; Semiatin, S. L., Eds.; ASM International: Materials Park, OH, U.S.A., 2009; Vol. 22A, pp 203–219.
47. Lokhande, C. D.; Sankapal, B. R.; Mane, R. S.; Pathan, H. M.; Muller, M.; Giersig, M.; Ganesan, V. *Appl. Surf. Sci.* **2002,** *193,* 1–10. doi:10.1016/s0169-4332(01)00819-4
48. Krishnan, B.; Arato, A.; Cardenas, E.; Roy, T. K. D.; Castillo, G. A. *Appl. Surf. Sci.* **2008,** *254,* 3200–3206. doi:10.1016/j.apsusc.2007.10.098
49. Zhu, G.; Huang, X.; Hojamberdiev, M.; Liu, P.; Liu, Y.; Tan, G.; Zhou, J.-p. *J. Mater. Sci.* **2011,** *46,* 700–706. doi:10.1007/s10853-010-4797-5
50. Bessegato, G. G.; Cardoso, J. C.; Silva, B. F. d.; Zanoni, M. V. B. *J. Photochem. Photobiol., A* **2014,** *276,* 96–103. doi:10.1016/j.jphotochem.2013.12.001
51. Zheng, L.; Jiang, K.; Huang, J.; Zhang, Y.; Bao, B.; Zhou, X.; Wang, H.; Guan, B.; Yang, L. M.; Song, Y. *J. Mater. Chem. A* **2017,** *5,* 4791–4796. doi:10.1039/c7ta00291b
52. Wang, W.; Strössner, F.; Zimmermann, E.; Schmidt-Mende, L. *Sol. Energy Mater. Sol. Cells* **2017,** *172,* 335–340. doi:10.1016/j.solmat.2017.07.046
53. Kozytskiy, A. V.; Stroyuk, O. L.; Skoryk, M. A.; Dzhagan, V. M.; Kuchmiy, S. Y.; Zahn, D. R. T. *J. Photochem. Photobiol., A* **2015,** *303–304,* 8–16. doi:10.1016/j.jphotochem.2015.02.005
54. Kamruzzaman, M.; Chaoping, L.; Yishu, F.; Farid Ul Islam, A. K. M.; Zapien, J. A. *RSC Adv.* **2016,** *6,* 99282–99290. doi:10.1039/c6ra20378g
55. Morteani, G.; Ruggieri, G.; Möller, P.; Preinfalk, C. *Miner. Deposita* **2011,** *46,* 197–210. doi:10.1007/s00126-010-0316-5
56. Oja Acik, I.; Junolainen, A.; Mikli, V.; Danilson, M.; Krunks, M. *Appl. Surf. Sci.* **2009,** *256,* 1391–1394. doi:10.1016/j.apsusc.2009.08.101
57. Tauc, J.; Grigorovici, R.; Vancu, A. *Phys. Status Solidi* **1966,** *15,* 627–637. doi:10.1002/pssb.19660150224
58. Grozdanov, I. *Semicond. Sci. Technol.* **1994,** *9,* 1234–1241. doi:10.1088/0268-1242/9/6/013
59. Grozdanov, I.; Ristov, M.; Sinadinovski, G.; Mitreski, M. *J. Non-Cryst. Solids* **1994,** *175,* 77–83. doi:10.1016/0022-3093(94)90317-4

60. Medina-Montes, M. I.; Montiel-González, Z.; Paraguay-Delgado, F.; Mathews, N. R.; Mathew, X. *J. Mater. Sci.: Mater. Electron.* **2016,** *27,* 9710–9719. doi:10.1007/s10854-016-5033-0
61. Wojdyr, M. *J. Appl. Crystallogr.* **2010,** *43,* 1126–1128. doi:10.1107/s0021889810030499

License and Terms

BEILSTEIN JOURNAL OF NANOTECHNOLOGY

Relation between thickness, crystallite size and magnetoresistance of nanostructured $La_{1-x}Sr_xMn_yO_{3\pm\delta}$ films for magnetic field sensors

Rasuole Lukose[*1], Valentina Plausinaitiene[1,2], Milita Vagner[1,2], Nerija Zurauskiene[1,3], Skirmantas Kersulis[1], Virgaudas Kubilius[2], Karolis Motiejuitis[2], Birute Knasiene[4], Voitech Stankevic[1,3], Zita Saltyte[1,2], Martynas Skapas[5], Algirdas Selskis[5] and Evaldas Naujalis[4]

Letter

Open Access

Address:
[1]Department of Material Science and Electrical Engineering, Center for Physical Sciences and Technology, Sauletekio av. 3, LT-10257 Vilnius, Lithuania, [2]Institute of Chemistry, Faculty of Chemistry and Geosciences, Vilnius University, Naugarduko 24, LT- 03225 Vilnius, Lithuania, [3]Department of Electrical Engineering, Faculty of Electronics, Vilnius Gediminas Technical University, Naugarduko 21, LT- 03227 Vilnius, Lithuania, [4]Department of Metrology, Center for Physical Sciences and Technology, Sauletekio av. 3, LT-10257 Vilnius, Lithuania and [5]Department of Characterization of Materials Structure, Center for Physical Sciences and Technology, Sauletekio av. 3, LT-10257 Vilnius, Lithuania

Email:
Rasuole Lukose[*] - rasuole.lukose@ftmc.lt

* Corresponding author

Keywords:
colossal magnetoresistance; crystallites; magnetic field sensors; MOCVD growth; nanostructured films

Beilstein J. Nanotechnol. **2019,** *10,* 256–261.
doi:10.3762/bjnano.10.24

Received: 21 September 2018
Accepted: 21 December 2018
Published: 23 January 2019

This article is part of the thematic issue "Chemical thin coating methods for functional nanomaterials".

Guest Editor: J. Bachmann

Abstract

In the present study the advantageous pulsed-injection metal organic chemical vapour deposition (PI-MOCVD) technique was used for the growth of nanostructured $La_{1-x}Sr_xMn_yO_{3\pm\delta}$ (LSMO) films on ceramic Al_2O_3 substrates. The compositional, structural and magnetoresistive properties of the nanostructured manganite were changed by variation of the processing conditions: precursor solution concentration, supply frequency and number of supply sources during the PI-MOCVD growth process. The results showed that the thick (≈400 nm) nanostructured LSMO films, grown using an additional supply source of precursor solution in an exponentially decreasing manner, exhibit the highest magnetoresistance and the lowest magnetoresistance anisotropy. The possibility to use these films for the development of magnetic field sensors operating at room temperature is discussed.

Introduction

Perovskite manganite materials are an interesting topic of research since they can be applied as sensors for measuring the magnetic field due to the colossal magnetoresistance (CMR) phenomenon [1]. The complex physics of manganite materials provides an opportunity to tune their electric and magnetic properties over a wide range by variation of chemical composition [2-5], film thickness [6,7] and nanostructure [8,9], as well as induced lattice strain [10-12]. The manganite films consisting of columnar nanograins have already been successfully applied for the sensing of high pulsed magnetic fields (B-scalar sensor) [13,14]. Despite this development, the scalar (independent of field orientation) CMR effect under a low magnetic field is still a challenging goal towards practical applications due to low sensitivity and large magnetic anisotropy [15,16]. For this reason, the investigation and control of the magnetoresistive properties of manganite materials on the nanometer scale is of great importance. It was shown that the change of nanostructure by variation of deposition temperature influences the magnetic properties of the films [17]. The increase of the deposition rate also results in changes in the crystallite dimensions, leading to a higher number of nucleation sites [18]. In our research, the pulsed-injection metal organic chemical vapour deposition (PI-MOCVD) [19,20] was used to enable easy and reproducible control of the growth rate and nucleation site density by introducing the additional supply source of the precursor solution to the reaction chamber.

The novelty of our investigations concerns the growth of $La_{1-x}Sr_xMn_yO_{3\pm\delta}$ (LSMO) films on ceramic Al_2O_3 substrates in two different technological ways, resulting in different microstructure of the obtained nanostructured films. Such films have an advantage in comparison with the epitaxial films grown on monocrystalline substrates since they exhibit high magnetoresistance (MR) values over a broader temperature range [1].

In this study, we present the possibility to tune and to select the necessary properties of nanostructured LSMO films by changing the film thickness and microstructure in order to obtain higher sensitivity and lower anisotropy, important for magnetic field sensing.

Results and Discussion

Two series of films of variable thickness were deposited: I – one source with LSMO solution, II – 2 separate sources, LSMO solution and solvent source (Figure 1). The growth rate

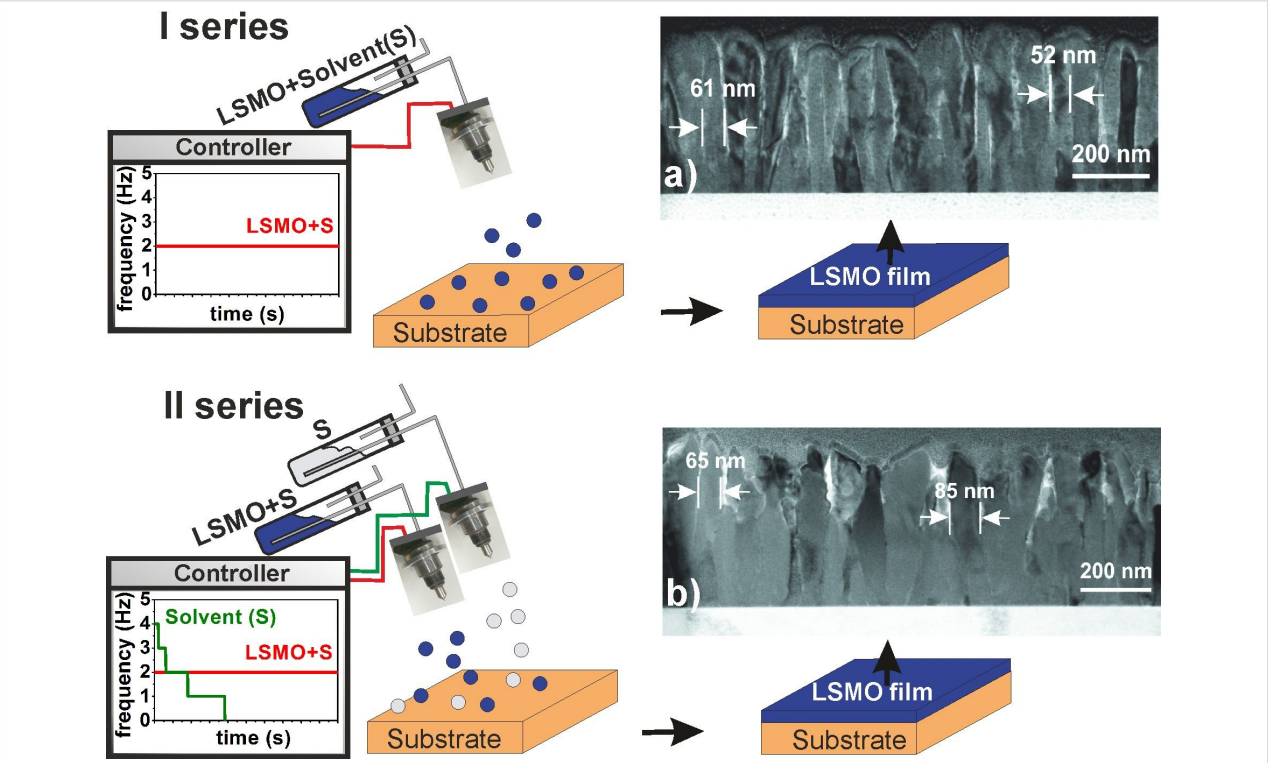

Figure 1: Schematic representation of the two deposition series of nanostructured LSMO films. I series – the mixture of precursors dissolved in the solvent is supplied to the reaction chamber. II series – 2 separate supply sources are used: i.) mixture of the precursor solution; ii.) solvent only, supplied in an exponentially decreasing manner leading to larger crystallites (TEM figures) and improved MR properties. (a, b) Cross-sectional TEM pictures of nanostructured LSMO films, for I and II deposition series.

was controlled by application of additional solvent, resulting in the dilution of the precursor in the gas phase.

The transmission electron microscopy (TEM) analysis (Figure 1a,b) shows the column-like growth with larger dimensions and more dense, close packing of the crystallites for the II series.

Film composition, structure and surface morphology

Figure 2a–c presents scanning electron microscopy (SEM) images of the films with different thickness showing the increase in the crystallite dimensions with the film thickness. Moreover, the mass spectroscopy measurements revealed the change of elemental composition: the average strontium amount decreased with the decrease of film thickness independent of the deposition series (Figure 2d). The amount of La (1−x(Sr)) was slightly decreased from 0.975 to 0.9 with respect to the increase of the amount of Sr from 0.025 up to 0.1. The measured content of Mn in the films was in the range of 1.12–1.21. The grazing incidence X-ray diffraction (GIXRD) measurements presented in Figure 2e show no secondary phases, only the characteristic peaks associated with the Al_2O_3 substrate and polycrystalline LSMO films with a perovskite-like crystal structure with rhombohedral distortions (the space group $R\bar{3}c$) for both deposition series. The shift of the characteristic LSMO peaks to higher θ/2θ angles indicates the reduction of the a and c lattice parameters. The LeBail modelling of the XRD patterns showed the linear dependence of lattice parameters on the film thickness (Figure 2f). Additionally, the reduction of (n0n) peak intensities was observed for nanostructured LSMO films with a decrease of the film thickness for both deposition series (Figure 2e and inset). This effect is attributed to the reduction of the cell volume and appearance of strain in the films with the decrease of the film thickness, as was also observed by H. Baaziz and co-authors for $La_{0.9}Sr_{0.1}MnO_3$ nanoparticles [21].

Transport and magnetoresistive properties

In nanostructured manganite materials the difference in dimensions of crystallites and change of the relative amount of grain boundaries (GBs) and film composition significantly change the transport behaviour [17,21]. The decrease of electrical resistivity and the increase of the metal–insulator transition temperature (T_{MI}) were observed with the increase of film thickness, crystallite dimensions and Sr content for both deposition series (Figure 3a and 3b). No significant difference in the T_{MI} was observed for the I and II series (Figure 3b insert).

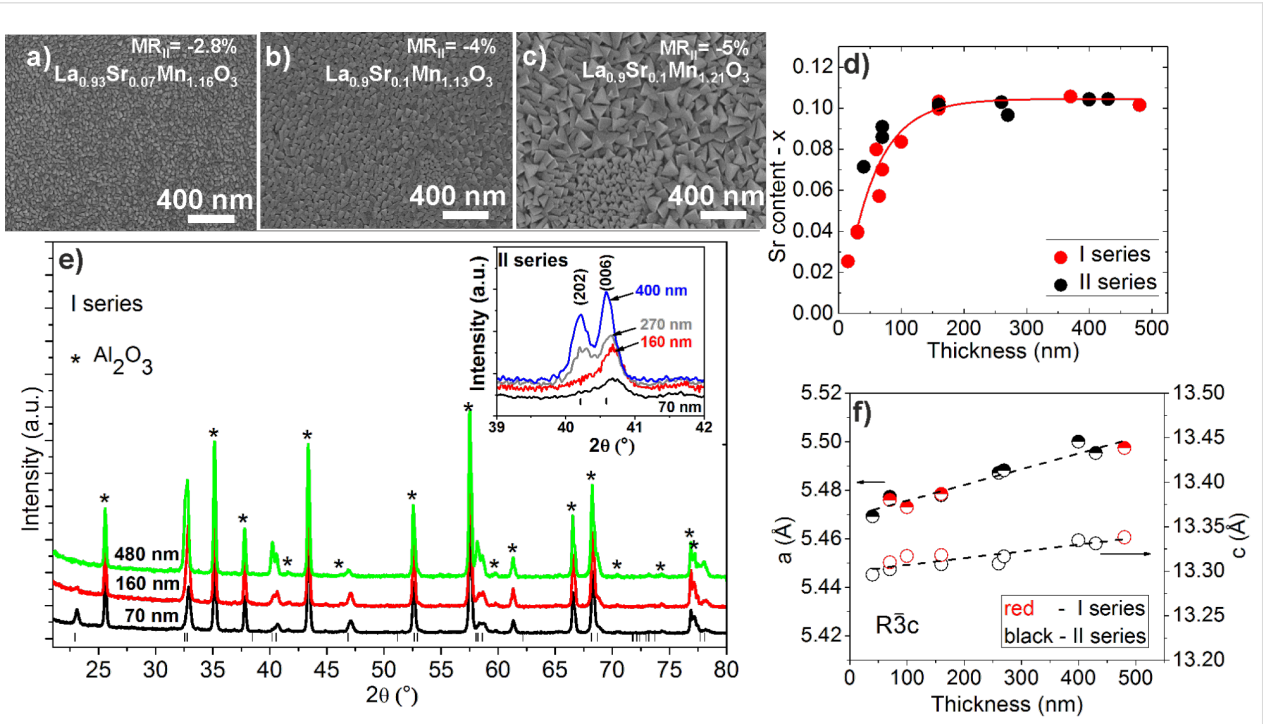

Figure 2: (a–c) SEM pictures of LSMO films (I series) deposited on Al_2O_3 substrates with different thickness: (a) 70 nm, (b) 160 nm and (c) 480 nm. (d) The average strontium (x) content (deduced from ICP-MS measurements) dependence on the thickness of the deposited LSMO films (I and II series, the red line is a guide for the eye). (e) GIXRD patterns for the LSMO films of different thickness for the I series. The inset presents peaks and their shift with thickness for the II series. The stars represent the characteristic peaks of the Al_2O_3 substrate, the vertical lines represent the characteristic peaks of LSMO in rhombohedral distortion. (f) The a and c lattice parameters calculated from XRD patterns for LSMO films of both series.

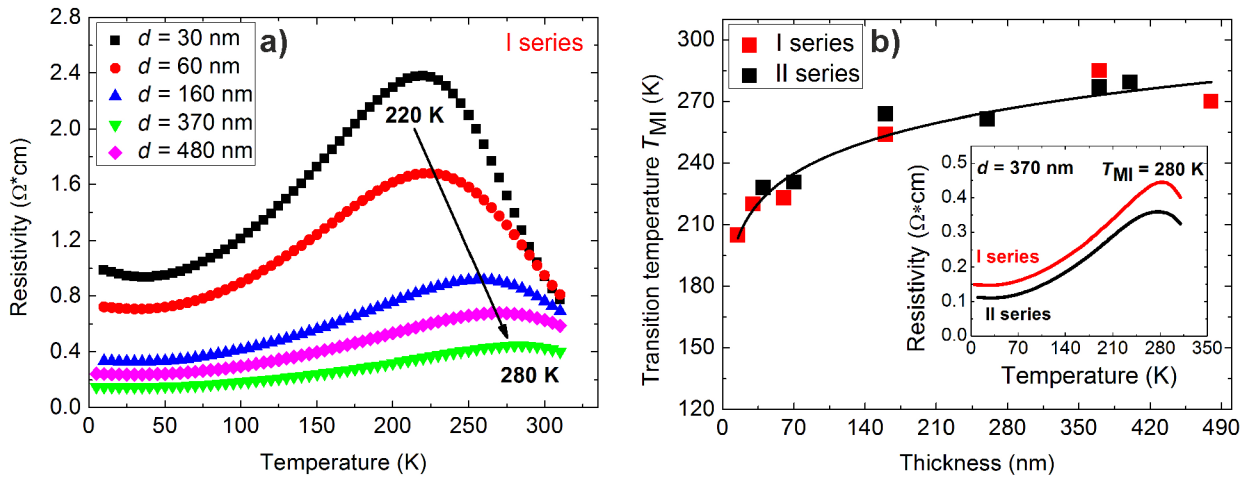

Figure 3: (a) Resistivity dependence on temperature for nanostructured LSMO films with thickness in the range of 30–480 nm grown on Al_2O_3 substrates; (b) T_{MI} dependence on film thickness for both deposition series, black line is a guide for the eye. Inset – resistivity dependence on temperature for 370 nm thick LSMO films of the I and II series.

However, higher resistivity values were observed for the I series films (Figure 3b insert) due to smaller crystallites (Figure 4a,b) and larger number of GBs. The average crystallite diameter of 56 nm and 69 nm was found for the I and II series (Figure 4c), respectively.

The technological processing and decrease of the growth rate (I series – 28 nm/min; II series – 18 nm/min) enabled an increase of the crystallite size at the same deposition temperature. In relation to the dimensions of the crystallites and transport properties, the increase of the MR (where MR = $(\rho_B - \rho_0)/\rho_0$ and ρ_B and ρ_0 are the field and zero field resistivity, respectively) with film thickness was observed (Figure 4d,e). The largest MR magnitude (6%, when the field was directed parallel to the film plane $B_{||}$ = 0.7 T) was obtained for the thickest films (≈400 nm) of the II series. The measured

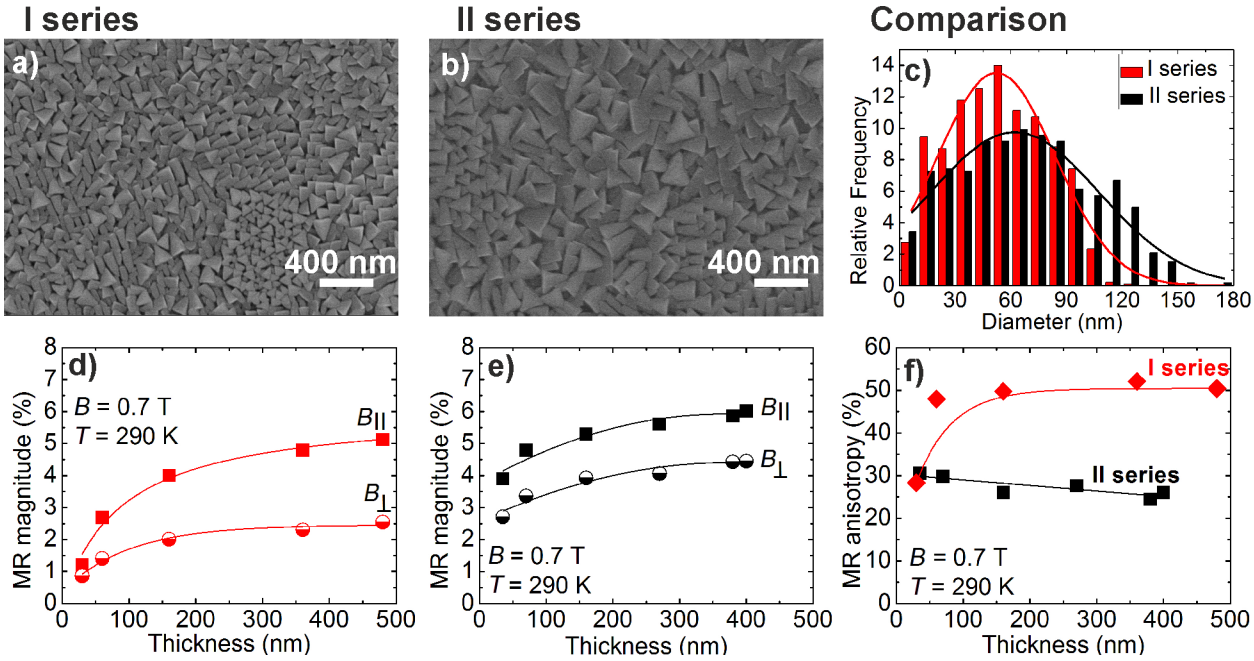

Figure 4: SEM picture of LSMO films grown from (a) one supply source - I series; (b) two supply sources - II series. (c) Comparison of relative frequency dependence on diameter of the crystallites for the I and II series 370 nm thick films. Magnetoresistance dependence on LSMO film thickness with applied external magnetic field of 0.7 T parallel ($B_{||}$) and perpendicular ($B_\perp$) to the plane of the film grown from (d) one supply source and (e) two supply sources. (f) Magnetoresistance anisotropy dependence on film thickness for both deposition series. The lines are the guides for the eye.

MR values of this II series films at room temperature are higher in comparison with the results obtained by other authors (<2%) [22,23]. For the field perpendicular to the film plane $B_{\perp}$, the MR was lower due to the demagnetization effect, which resulted in MR anisotropy (MRA = $(MR_{\parallel} - MR_{\perp}) / MR_{\parallel}$) (Figure 4f). It is known that in thin manganite films the direction of the easy axis of magnetization is parallel to the film plane due to the fact that the demagnetization field is directly linked with the geometric shape of the sample [15,16]. In our case, this effect is partly compensated by the columnar structure of the film, where each individual crystallite has the easy axis of magnetization directed perpendicular to the film plane. Therefore, this compensation is more effective for thicker films of the II series, having larger monolithic crystallites with the most probably of higher individual magnetization in comparison with the films of the I series with smaller crystallites. As a result, the compensation of the demagnetization field leads to the lower MRA (25%) and slightly higher sensitivity $\Delta MR/\Delta B$ (7.7%/T) measured at 0.7 T for II series films, whereas for the I series films, MRA is ≈50% and the sensitivity 6.5%/T. For higher fields, the MRA decreased (14% at 2 T, 2% at 10 T) implying the possibility to use these films for the development of B-scalar sensors operating under high magnetic fields.

Conclusion

In this study, the nanostructured LSMO films were grown by PI-MOCVD in two different technological ways (with and without additional source of solvent) enabling the control of the microstructure and magnetoresistive properties of the films. It was demonstrated that the crystallite dimensions and magnetoresistance magnitude increase with the film thickness. Moreover, the usage of an additional solvent source decreases the growth rate of the films, leading to an increase of crystallite dimensions. As a result, an increase in the magnetoresistance and reduction of magnetoresistance anisotropy is achieved, which is technologically important for the production of magnetic field sensors.

Experimental

The nanostructured LSMO films were grown on ceramic Al_2O_3 substrates by the PI-MOCVD technique by supplying a mixture of precursor solution and solvent in micro-doses of 3 mg. $La(thd)_3$, $Sr(thd)_2$, and $Mn(thd)_3$ (where thd is 2,2,6,6-tetramethyl-3,5-heptandionate) were used as precursors and dissolved in the dimethoxyethane solvent. Two deposition series were performed using one (precursor solution – I series) or two (precursor solution and solvent – II series) precursor supply sources with a constant 2 Hz supply frequency. The software controlling the operation of the second supply source (solvent) is based on the following 5-step program: the supply frequency is kept constant during each step and is changed after different time intervals (steps) – 30, 90, 105, 280 and 350 s, in order to follow an exponentially decreasing law. During the first cycle, two additional micro-doses of solvent with respect to the precursor solution were supplied, whereas during the last cycle, only the precursor solution was injected. The supply of the solvent source during the intermediate cycles was varied as shown in Figure 1. The LSMO films were deposited at 750 °C and 10 Torr with a partial 3.5 Torr oxygen pressure and post-annealed for 10 minutes in oxygen atmosphere. The thickness of the films was changed in the range of 30–480 nm and determined using a Taylor Hobson Talystep profilometer. The crystal structure of the films was analysed by GIXRD measurements using a Bruker D8 Advance diffractometer, where the incident X-ray beam was fixed at 0.5°. The refinement of the peak shape in the XRD diffraction patterns was performed by using the computer program TOPAS 4.2. The XRD peak shape corrections were proceeded with LaB_6 powder standard (SRM660a) certificated by the National Institute of Standards and Technology. The morphology of the films was investigated by SEM (Hitachi SU70). The structural analysis was performed in cross section geometry by TEM (FEI Tecnai G2 F20 X-TWIN). The elemental composition analysis was performed by inductively coupled plasma high-resolution mass spectrometry (ICP-MS) - Thermo Scientific Element2, where the films were totally dissolved in 2% nitric acid. For the electric transport and magnetoresistance measurements, the Ag contacts with a Cr sublayer were thermally deposited and postannealed at 450 °C for 1 h in Ar atmosphere. The magnetoresistance (MR) measurements were performed under a permanent magnetic field up to 0.7 T using an electromagnet and a pulsed field up to 10 T using a generator based on capacitor bank discharge through a special multi-shot magnetic field coil.

Acknowledgements

R. Lukose and N. Zurauskiene acknowledges the funding from the European Union's Horizon 2020 research and innovation programme under the Marie Sklodowska-Curie grant agreement No 751905. V. Plausinaitiene, M. Vagner, N. Zurauskiene, S. Kersulis and V. Stankevic are thankful for the partial support of these investigations by the Research Council of Lithuania under Grant S-MIP-17-110.

ORCID® iDs

Rasuole Lukose - https://orcid.org/0000-0003-0154-2656
Valentina Plausinaitiene - https://orcid.org/0000-0002-3591-2224
Milita Vagner - https://orcid.org/0000-0001-8557-5628
Nerija Zurauskiene - https://orcid.org/0000-0003-0912-4563
Skirmantas Kersulis - https://orcid.org/0000-0002-1815-357X
Virgaudas Kubilius - https://orcid.org/0000-0002-8727-1617
Karolis Motiejuitis - https://orcid.org/0000-0002-9197-1763
Voitech Stankevic - https://orcid.org/0000-0002-6552-0862

Martynas Skapas - https://orcid.org/0000-0002-6152-4612
Algirdas Selskis - https://orcid.org/0000-0002-0940-3733

References

1. Haghiri-Gosnet, A.-M.; Renard, J.-P. *J. Phys. D: Appl. Phys.* **2003,** *36,* R127–R150. doi:10.1088/0022-3727/36/8/201
2. Abdelmoula, N.; Dhahri, E.; Fourati, N.; Reversat, L. *J. Alloys Compd.* **2004,** *365,* 25–30. doi:10.1016/s0925-8388(03)00639-x
3. Yusuf, S. M.; Sahana, M.; Dörr, K.; Rößler, U. K.; Müller, K.-H. *Phys. Rev. B* **2002,** *66,* 064414. doi:10.1103/physrevb.66.064414
4. Raychaudhuri, P.; Mukherjee, S.; Nigam, A. K.; John, J.; Vaisnav, U. D.; Pinto, R.; Mandal, P. *J. Appl. Phys.* **1999,** *86,* 5718–5725. doi:10.1063/1.371584
5. Troyanchuk, I. O.; Lobanovsky, L. S.; Khalyavin, D. D.; Pastushonok, S. N.; Szymczak, H. *J. Magn. Magn. Mater.* **2000,** *210,* 63–72. doi:10.1016/s0304-8853(99)00620-4
6. Moon, E. J.; Balachandran, P. V.; Kirby, B. J.; Keavney, D. J.; Sichel-Tissot, R. J.; Schlepütz, C. M.; Karapetrova, E.; Cheng, X. M.; Rondinelli, J. M.; May, S. J. *Nano Lett.* **2014,** *14,* 2509–2514. doi:10.1021/nl500235f
7. Monsen, Å.; Boschker, J. E.; Macià, F.; Wells, J. W.; Nordblad, P.; Kent, A. D.; Mathieu, R.; Tybell, T.; Wahlström, E. *J. Magn. Magn. Mater.* **2014,** *369,* 197–204. doi:10.1016/j.jmmm.2014.06.038
8. Henry, L. L.; Gnanasekar, K. I.; Chen, C.; Meletis, E. I. *Nano Lett.* **2004,** *4,* 741–745. doi:10.1021/nl049947f
9. Hunter, D.; Dadson, J. B.; Zhang, K.; Lasley, B.; Lord, K.; Williams, T. M.; Rakhimov, R. R.; Pradhan, A. K.; Zhang, J.; Sellmyer, D. J. *J. Appl. Phys.* **2006,** *99,* 08Q307. doi:10.1063/1.2162088
10. Suzuki, Y.; Hwang, H. Y.; Cheong, S.-W.; van Dover, R. B. *Appl. Phys. Lett.* **1997,** *71,* 140–142. doi:10.1063/1.119454
11. Millis, A. J.; Darling, T.; Migliori, A. *J. Appl. Phys.* **1998,** *83,* 1588–1591. doi:10.1063/1.367310
12. Ovsyannikov, G. A.; Petrzhik, A. M.; Borisenko, I. V.; Klimov, A. A.; Ignatov, Y. A.; Demidov, V. V.; Nikitov, S. A. *J. Exp. Theor. Phys.* **2009,** *108,* 48–55. doi:10.1134/s1063776109010075
13. Stankevič, T.; Medišauskas, L.; Stankevič, V.; Balevičius, S.; Žurauskienė, N.; Liebfried, O.; Schneider, M. *Rev. Sci. Instrum.* **2014,** *85,* 044704. doi:10.1063/1.4870280
14. Balevičius, S.; Žurauskienė, N.; Stankevič, V.; Keršulis, S.; Plaušinaitienė, V.; Abrutis, A.; Zherlitsyn, S.; Herrmannsdörfer, T.; Wosnitza, J.; Wolff-Fabris, F. *Appl. Phys. Lett.* **2012,** *101,* 092407. doi:10.1063/1.4749820
15. Žurauskienė, N.; Keršulis, S.; Medišauskas, L.; Tolvaišienė, S. *Acta Phys. Pol., A* **2011,** *119,* 186–188. doi:10.12693/aphyspola.119.186
16. Zurauskiene, N.; Balevicius, S.; Stankevic, V.; Kersulis, S.; Schneider, M.; Liebfried, O.; Plausinaitiene, V.; Abrutis, A. *IEEE Trans. Plasma Sci.* **2011,** *39,* 411–416. doi:10.1109/tps.2010.2064338
17. Zurauskiene, N.; Balevicius, S.; Stankevic, V.; Kersulis, S.; Klimantavicius, J.; Plausinaitiene, V.; Kubilius, V.; Skapas, M.; Juskenas, R.; Navickas, R. *J. Mater. Sci.* **2018,** *53,* 12996–13009. doi:10.1007/s10853-018-2567-y
18. Willmott, P. R. *Prog. Surf. Sci.* **2004,** *76,* 163–217. doi:10.1016/j.progsurf.2004.06.001
19. Felten, F.; Senateur, J. P.; Weiss, F.; Madar, R.; Abrutis, A. *J. Phys. IV* **1995,** *05,* C5-1079. doi:10.1051/jphyscol:19955127
20. Abrutis, A.; Plausinaitiene, V.; Kubilius, V.; Teiserskis, A.; Saltyte, Z.; Butkute, R.; Senateur, J. P. *Thin Solid Films* **2002,** *413,* 32–40. doi:10.1016/s0040-6090(02)00352-8
21. Baaziz, H.; Tozri, A.; Dhahri, E.; Hlil, E. K. *Ceram. Int.* **2015,** *41,* 2955–2962. doi:10.1016/j.ceramint.2014.10.129
22. Staruch, M.; Jain, M. *J. Solid State Chem.* **2014,** *214,* 12–16. doi:10.1016/j.jssc.2013.11.037
23. Zhang, Z.; Ranjith, R.; Xie, B. T.; You, L.; Wong, L. M.; Wang, S. J.; Wang, J. L.; Prellier, W.; Zhao, Y. G.; Wu, T. *Appl. Phys. Lett.* **2010,** *96,* 222501. doi:10.1063/1.3432113

License and Terms

BEILSTEIN JOURNAL OF NANOTECHNOLOGY

Site-specific growth of oriented ZnO nanocrystal arrays

Rekha Bai[1], Dinesh K. Pandya[*1], Sujeet Chaudhary[1], Veer Dhaka[2], Vladislav Khayrudinov[2], Jori Lemettinen[2], Christoffer Kauppinen[2] and Harri Lipsanen[2]

Full Research Paper

Open Access

Address:
[1]Thin Film Laboratory, Physics Department, Indian Institute of Technology Delhi, New Delhi 110016, India and [2]Department of Electronics and Nanoengineering, Micronova, Aalto University, Tietotie 3, 02150 Espoo, Finland

Email:
Dinesh K. Pandya[*] - dkpandya@physics.iitd.ac.in

* Corresponding author

Keywords:
electrodeposition; growth kinetics; nanocrystals; nucleation; twinning; zinc oxide

Beilstein J. Nanotechnol. **2019,** *10,* 274–280.
doi:10.3762/bjnano.10.26

Received: 09 September 2018
Accepted: 27 December 2018
Published: 24 January 2019

This article is part of the thematic issue "Chemical thin coating methods for functional nanomaterials".

Guest Editor: J. Bachmann

Abstract

We report on the growth of ZnO nanocrystals having a hexagonal, prismatic shape, sized 700 nm × 600 nm, on bare indium tin oxide (ITO) substrates. The growth is induced by a low ion flux and involves a low-temperature electrodeposition technique. Further, vertically aligned periodic nanocrystal (NC) growth is engineered at predefined positions on polymer-coated ITO substrates patterned with ordered pores. The vertical alignment of ZnO NCs along the *c*-axis is achieved via ion-by-ion nucleation-controlled growth for patterned pores of size ≈600 nm; however, many-coupled branched NCs with hexagonal shape are formed when a patterned pore size of ≈200 nm is used. X-ray diffraction data is in agreement with the observed morphology. A mechanism is proposed to interpret the observed site-specific oriented/branched growth that is correlated to the pore size. As ordered NC arrays have the potential to generate new collective properties different from single NCs, our first demonstration of a cost effective and facile fabrication process opens up new possibilities for devices with versatile functionalities.

Introduction

Metal oxide semiconductor nanostructures are quite interesting not only in terms of the basic growth mechanism involved in their fabrication, but also due to the large number of applications based on them in the field of nanoscale optoelectronics [1-4]. ZnO is an important direct band gap (≈3.3 eV), nontoxic, metal oxide semiconductor, which can readily be used for optoelectronic applications. The properties of ZnO can be tailored by changing the morphology of the structures. Thus, fabrication of ZnO having different morphological structures such as nanorods [5-7], nanowires [8], tetrapods [9], nanodisks [10], nanotubes [11], flowers [12], and nanocrystals [13], have been reported. Among the many nanostructured morphologies possible for ZnO, self-assembled ZnO nanocrystals (NCs) have been attracting great attention due to their versatile applications [14]. Self-assembled NC arrays collectively can possibly demonstrate new properties, unlike the fixed properties of single NCs, forming new nanostructures with useful functionalities. Semiconductor NC self-assembly depends on the shape and size of the NCs, a broad range of interactions comprising the cohesive forces of the bulk material, as well as strong

coulomb interactions, weak van der Waal forces, and hydrogen bonding. There are reports on the growth of self-assembled twinned pyramids and twinned ZnO nanocrystals [14-16]. The growth of self-assembled NCs is generally reported by solution-based methods such as hydrothermal and solvothermal techniques, which are time consuming, involve multistep methodologies and may be cost ineffective processes [15-20]. In addition to that, these solution-based methods employ a high concentration of precursors and the growth is controlled by some additional reactants during the chemical reaction such as KOH, LiOH and NaOH [21,22]. These additional reactants are employed to reduce the growth rate as well as growth temperature. But, even for a very small concentration of additional reactant added in the reaction bath, the incorporation of some exotic metal ions in the ZnO lattice may produce some inadvertent defect levels and charge carrier recombination centers, in turn deteriorating some of the important material properties. Moreover, these reactants are responsible for changing the surface energy of the crystal facets in an undefined and complex way, which results in the formation of branched nanostructures [21]. Another disadvantage of these solution-based techniques is that the growth takes place in the solution itself and the grown nanocrystals are distributed randomly when collected on the substrate. However, in applications like solar cells based on core/shell ZnO nanocrystals, site-specific growth of the well-aligned nanocrystals is quite important. Therefore, the position-controlled oriented growth of ZnO NC array architectures is highly desirable for practical applications.

In order to simultaneously accomplish the controllable growth of highly ordered as well as highly oriented ZnO NCs with high throughput and maintain low cost for possible large-scale production, we have explored the feasibility of the process based on the combination of employing the use of patterned substrates and a cost-effective growth technique. In particular, we demonstrate the growth of hexagonal faceted self-assembled twin ZnO NCs on bare indium tin oxide (ITO) substrate via a facile low temperature electrodeposition technique that has the potential of yielding good crystal quality with a variety of possible nanoarchitectures under low ion-flux conditions. This growth method has many advantages over the techniques employed in the earlier reports, such as controlled, fast and mass-production process of material fabrication; no requirement of additional reactant (generally used for decreasing the growth temperature and growth rate); cost-effective (due to employing a simple electrolytic bath cell and current source) and ability to grow various nanostructures at ambient pressure and temperature. Moreover, the directed nanocrystal growth can be accomplished on a substrate, rather than in the solution. Furthermore, from the current reported work it is quite difficult to conclude about the nature of twinning, that is, whether twinning appears by joining two NCs or if a single nanocrystal gives rise to the twinned crystal. However, in the electrodeposition technique, since the growth proceeds from a nucleus formed on the conducting substrate used as an electrode, this technique can play an important role to shed some light on the plausible growth mechanism involved in the fabrication of twinned ZnO NCs.

We demonstrate the growth of self-assembled twin ZnO NC arrays at predefined positions by employing polymer-coated ITO substrates patterned with periodic ordered pores. The growth of *c*-axis-aligned twin ZnO nanocrystal arrays was achieved at specific sites via a low-temperature electrodeposition technique with excellent control over orientation, dimension, and location. The effect of a patterned pore size in controlling the growth of array vs branched ZnO NCs is shown. A mechanism based on the nucleation and growth is proposed to understand the oriented/branched twin ZnO NC morphologies.

Experimental

Growth of ZnO nanocrystals

An electrodeposition technique was employed to grow ZnO nanocrystals on both bare and on an array of pores patterned on the polymer-coated indium-doped tin oxide (ITO) conducting substrates. The patterning process for the polymer, poly(Disperse Red 1 acrylate), involves laser interference lithography and oxygen plasma etching and has been reported in detail previously [23]. Two different sizes of pores with diameter ≈600 and ≈200 nm patterned on the ITO substrate employed in the present work are shown in Figure 1. The period of the pores was kept nearly the same. The electrodeposition process was carried out in a specially designed, closed, three electrode, glass cell. The bare/polymer-coated patterned ITO substrates were used as a working electrode (2 × 2 cm^2) while a platinum sheet (2.5 × 2.5 cm^2) and a saturated calomel electrode (SCE) were used as the counter and reference electrodes, respectively. The electrolyte (bath) temperature was kept at 60 °C. For the growth of ZnO, the precursor solution was obtained from the 1 mM $Zn(NO_3)_3{\cdot}6H_2O$. The electrochemical deposition of ZnO was carried out in solution having pH ≈5.6 at deposition potential −1.0 V (vs SCE) for 15 minutes using an electrochemical analyzer (CHI1104A). After deposition, the sample was removed from the electrolyte and rinsed in deionized water [24]. The sample grown on bare ITO is named as SB; the samples grown on patterned ITO with pore size ≈600 and ≈200 nm are named as S600 and S200, respectively.

Characterization of ZnO nanocrystals

The ZnO nanocrystals grown on bare/patterned ITO were structurally characterized using an X-ray diffractometer (PANalytical X'pert Pro model) having Cu Kα radiation (λ = 1.54 Å) in the 2θ range 20° to 80° using grazing incidence X-ray diffrac-

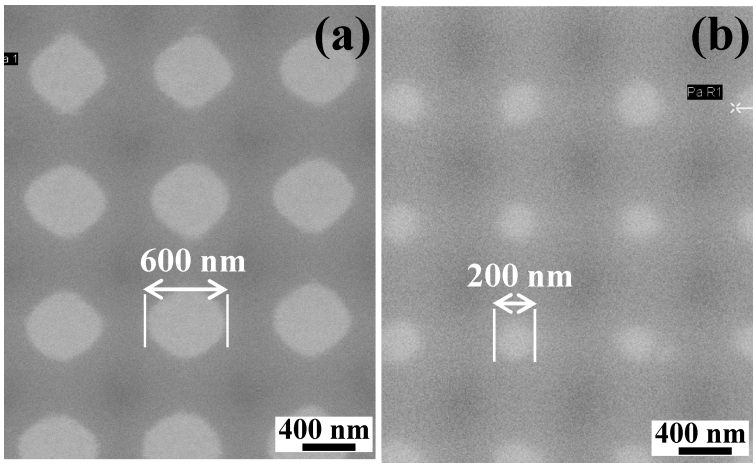

Figure 1: Field emission scanning electron microscopy images of (a) polymer-coated ITO patterned with a pore size of ≈600 nm, and (b) polymer-coated ITO patterned with a pore size of ≈200 nm.

tion (GIXRD). The setup consists of an X-ray mirror, a Ni filter, and a PIXcel3D detector in scanning line mode. The surface morphology of the prepared samples was investigated by using a field emission scanning electron microscopy (FESEM) using a Zeiss Supra 40 device. A JEOL 2200FS transmission electron microscope (TEM) was used to investigate the crystallinity of the NCs.

Results and Discussion

The FESEM images of ZnO NCs grown on bare ITO and on the array of pores patterned on the polymer-coated ITO substrates are shown in Figure 2. ZnO NCs grown on bare ITO are shown in Figure 2a–c and exhibit hexagonal prismatic shape that is characteristic of the wurtzite structure of ZnO. The crystals are well separated from each other and are oriented randomly on the substrate. This exhibits a central grain boundary (GB) perpendicular to the elongation direction (marked with dotted line in Figure 2b,c) that is generally assigned to twinning. These crystals with well-defined hexagonal face and side facets possess an overall length (2L) of ≈700 nm and a width/diagonal (D) of ≈600 nm. Typically, the top hexagonal faces of nanocrystals are composed of flat hexagonal terraces as seen in Figure 2b,c, characteristic of the layer-by-layer growth mechanism and are thus a clear indication of the ion-by-ion nucleation-controlled deposition process [5,25]. So, we observe that twinned ZnO NCs with almost the same diagonal dimension grow on bare ITO, though in random orientations. However, these become vertically aligned when grown in pores patterned on an ITO substrate with pore diameter ≈600 nm. Figure 2d–f shows the growth of such ZnO NCs (sample S600). It can be seen that the ZnO NCs grow in the pores on the ITO surface which is not covered with polymer. The growth of NCs is quite periodic as guided by the pore pattern. It can be further seen that the twinned ZnO NCs are grown in such a way that hexagonal faces, that define the *c*-axis, are parallel to the substrate. In Figure 2e,f, the central grain boundary perpendicular to the elongation direction can be clearly seen and indicates that polymer-assisted growth on ITO did not affect the morphology of twin NCs but helps to align them with their *c*-axis normal to the substrate. Moreover, the length and width of crystals are same as observed in the SB sample. Thus, we can say that the periodic array of *c*-axis-oriented twinned NCs at predetermined sites can be grown by patterning the polymer-coated ITO substrate. We also tried to control the width of well-aligned ZnO NCs by employing ITO patterned with a pore size of ≈200 nm (Figure 2g–i). Surprisingly, in contrast to the S600 sample, wherein crystals with *c*-axis normal to the ITO substrate are formed, many coupled branched ZnO NCs with hexagonal shape are revealed when the pore size was decreased to ≈200 nm (sample S200), demonstrating the significant effect of pore size on the morphology of ZnO NCs. However, it may be pointed out that although the overall morphology of the NCs is changed in S200, the periodicity observed is maintained in both S600 and S200 samples as per the pore pattern planned on the ITO substrate.

Now, the growth of twinned NCs on ITO substrate can be understood in terms of nucleation and growth kinetics involved during the fabrication process. The electrodeposition technique employed in this work rules out the formation of twinned ZnO NCs by co-joining two individual crystals of length ≈*L* (as is possible in solution-based techniques where two crystals independently formed by homogeneous nucleation in the solution itself can get coupled) as the growth starts by heterogeneous nucleation on the ITO surface. Since twinned crystals are observed to be formed, it is plausible that initially ZnO NCs

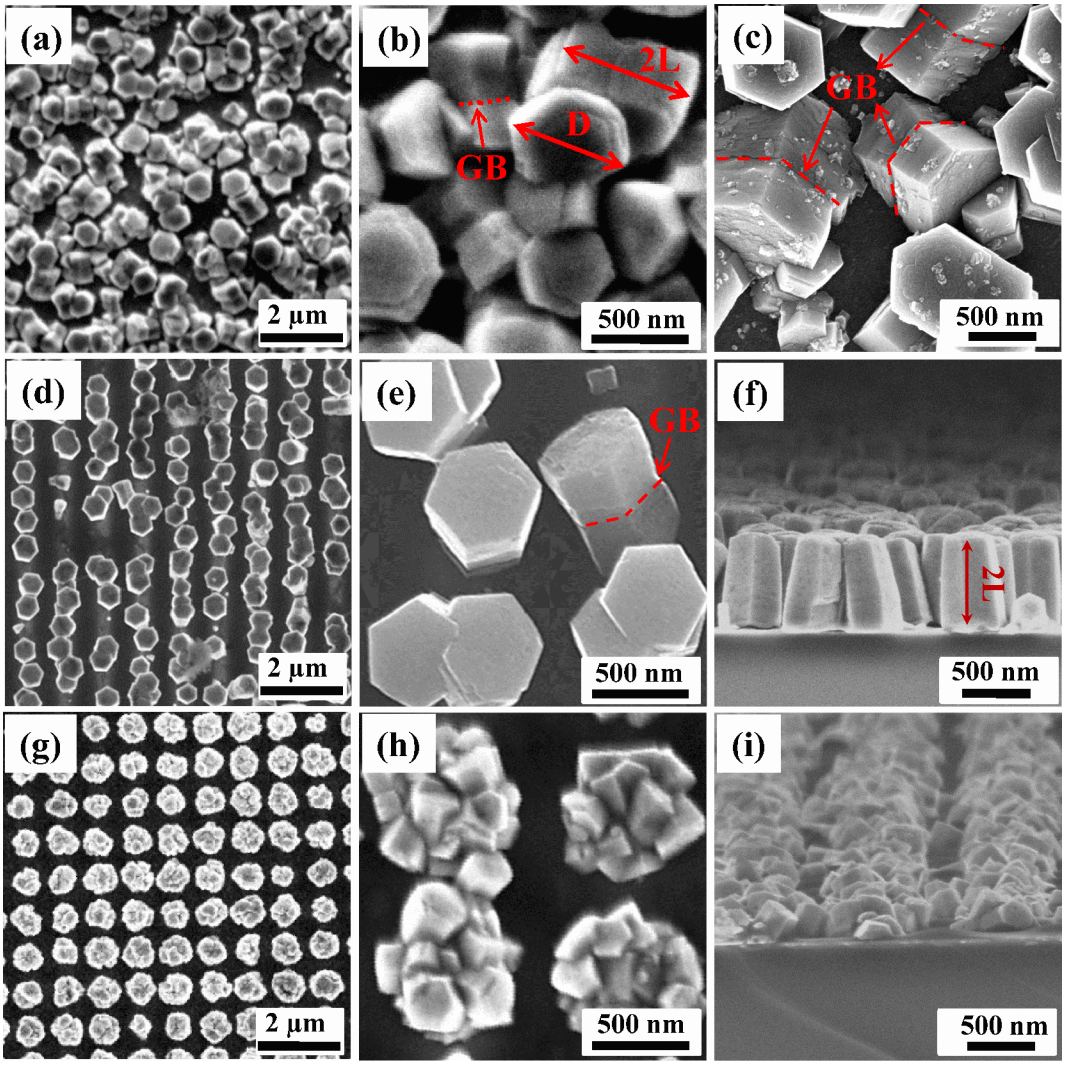

Figure 2: Top view FESEM images of ZnO NCs for (a, b, c) SB (on bare ITO) (d, e) S600 (on patterned ITO with pore size ≈600 nm), (g, h) S200 (on patterned ITO with pore size ≈200 nm) at low magnification and at high magnification; and the cross-sectional view for (f) S600 (i) S200, respectively.

having length ≈*L* and width ≈*D* grow on the bare ITO surface, and subsequently, a second set of crystalline material starts to grow on the top of first crystal and, in the process, leads to formation of twinned ZnO NCs. It is interesting to note that both the crystals forming the twin are almost of same dimensions, *L* and *D*. The obvious question is what gives rise to twin formation. The twin growth can be understood as follows. ZnO crystal structure consists of hexagonally close packed oxygen and zinc atoms. ZnO crystals consists of a top tetrahedron corner-exposed polar zinc (0001) face, six symmetric non-polar $\{10\bar{1}0\}$ planes parallel to the [0001] direction, and a basal polar oxygen $(000\bar{1})$ face [17]. It is well known that the hexagonal wurtzite ZnO has two polar planes (0001) and $(000\bar{1})$, which have high surface energy that can absorb new small particles to reduce its surface energy and thus ZnO NCs are oriented to grow along the [0001] direction [17]. The attractive force between the two basal planes is a prime requirement to make a twinned crystal. So, two negatively charged O (or positively charged Zn-terminated) crystal planes of ZnO can be linked together by adsorption of positively (or negatively) charged species. In the present work, only $Zn(NO_3)_3{\cdot}6H_2O$ is used as precursor to fabricate ZnO crystals and the reaction involved for the formation of ZnO crystals is as follows:

$$Zn^{2+} + NO_3^- + 2e^- \rightarrow ZnO + NO_2^-$$

As only NO_2^- ions are released during the reaction, so we can say that the two positively charged Zn-terminated polar planes are connected together by adsorption of NO_2^- and this could understandably account for the attractive force needed between two Zn-terminated basal planes for eventual formation of twinned NCs of ZnO.

The growth of *c*-axis oriented/branched ZnO NCs can be correlated to pore-size-dependent growth kinetics of ZnO crystals. In the case of the S600 sample that exhibits a vertical array of ZnO nanocrystals, the size of the pore was approximately equal to the width of ZnO NCs that are formed on bare ITO (sample SB). The growth conditions, still being same, allow the unhindered growth of ZnO NCs identical to that of the SB case, except only on the specific sites on the ITO surfaces exposed by patterning that are available for the heterogeneous nucleation. As the size of the pore was equal to the width of ZnO NCs grown on bare ITO, the lateral growth on the substrate is not restricted by the walls of the pores; however, the growth direction becomes aligned normal to the substrate. It is well known that ZnO crystals can be grown on ITO substrate with the (0001) plane parallel to the substrate plane. This results in the formation of *c*-axis-oriented NCs and twinning appears as explained earlier. But, in the case of S200 sample, the size of the patterned pore is three times smaller than the width of the crystals grown in case of SB and S600 samples. This results in the constrained lateral growth due to the walls of the pore and results in increased surface energy at the side faces of ZnO NCs. The constrained growth continues until the ZnO crystal grows to fill the pore and comes above the pore walls. Subsequently the seven surfaces (six sides and one top surface) serve as secondary nucleation sites and growth restarts from these high surface energy sites in order to reduce the surface energy accumulated from pore wall constrained growth. The branched coupled crystals are thus formed. So, we can conclude that the size of the patterned pore plays a crucial role to determine the morphology developed during the growth process.

XRD spectra of twinned ZnO NCs grown on the bare and patterned ITO substrates are shown in Figure 3. The XRD patterns of all the samples show that all the observed peaks correspond to hexagonal wurtzite phase (JCPDS 05-0664) of ZnO. The absence of any additional peak suggests that no other phase is formed. The peak marked by (*) emerged from the underlying ITO substrate. The substrate peak has relatively low intensity since the used GIXRD setup measures the volume close to the sample surface. It can be further seen that the XRD pattern of ZnO NCs grown on bare ITO does not show any preferential orientation for a particular plane and indicates the random orientation of the crystals grown on the bare ITO substrate, which is in accordance with the FESEM observations (Figure 2a). In contrast, the XRD pattern of S600 is dominated by a sharp diffraction peak at 34.4° corresponding to (002) planes and is indicative of the growth of ZnO NCs with the *c*-axis perpendicular to the substrate [5]. Some weak peaks corresponding to ZnO phase, e.g., (103), are also present on account of the slight tilt of the NCs away from vertical. The XRD results and FESEM images (Figure 2d) exhibiting vertically standing hexagonal prisms are consistent with each other. However, the XRD spectra of S200 shows no preferential orientation of any particular plane. This is in accordance with the FESEM data of the sample (Figure 2g), where ZnO NCs with branches oriented in various non-vertical directions are observed. Thus, we can conclude that the observed FESEM and XRD observations are consistent with each other with respect to the oriented and aligned growth of ZnO NCs or otherwise.

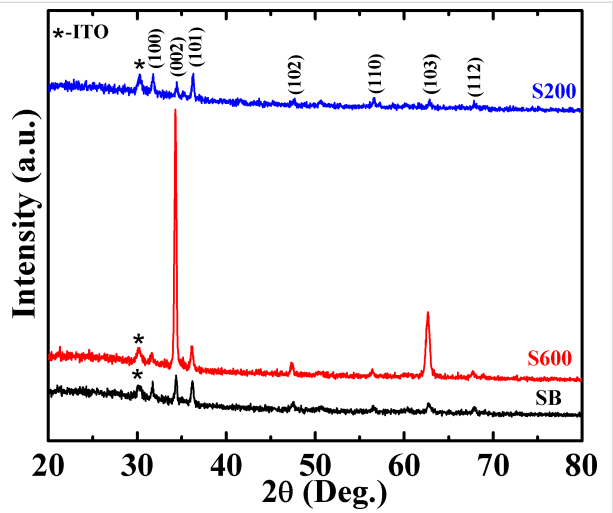

Figure 3: X-ray diffraction spectra of ZnO NCs for SB (on bare ITO), S600 (on patterned ITO with pore size ≈600 nm), and S200 (on patterned ITO with pore size ≈200 nm).

To further examine the crystal structure and morphology of the twinned ZnO NCs, TEM measurements were performed and the recorded images for the S600 sample are shown in Figure 4. Figure 4a,b shows the low-resolution bright-field TEM images of the hexagonal-shaped twinned S600 ZnO NCs. The figures reveal a smooth and clean surface with flat hexagonal terraces at the top of ZnO NCs having width/diagonal $D \approx 600$ nm, which is consistent with the observed FESEM in Figure 2d,e. The corresponding high-resolution TEM (HRTEM) image is recorded to further investigate the morphological characteristics of ZnO NCs. The observed sharp lattice fringes in the HRTEM image reveal the good crystallinity of twinned ZnO NCs. This is possibly due to the low ion flux arriving at the substrate surface that promotes the formation of well-ordered hexagonal-shaped twinned ZnO NCs followed by a controlled heterogeneous ion-by-ion growth mechanism [5,6] as demonstrated by the lattice fringes in Figure 4c. The NCs exhibit interplanar spacing of $d \approx 2.6$ Å belonging to the (002) lattice plane of the wurtzite phase of ZnO (JCPDS 05-0664), which is well in agreement with the XRD results (Figure 3). Moreover, the selected area electron diffraction (SAED) pattern (Figure 4d) reveals the excellent crystallinity of ZnO NCs and confirms the growth of the *c*-axis normal to the substrate in these twinned ZnO NCs.

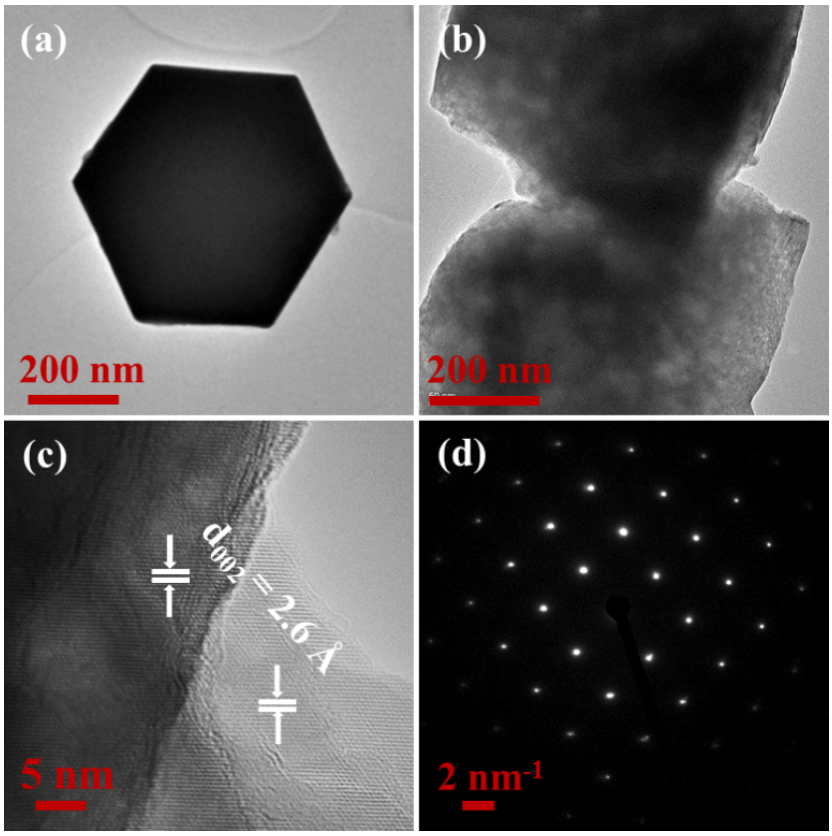

Figure 4: Microstructure characterization of hexagonal-shaped twinned ZnO NCs for the S600 sample. (a, b) Low-resolution TEM image, (c) high-resolution TEM image, and (d) selected area electron diffraction pattern.

Now we compare our growth method and quality of twinned ZnO NCs with similar structures reported previously. Greer et al. [15] have employed gelatin as the structure-directing agent to fabricate twinned ZnO NCs. The removal of embedded gelatin in NCs requires calcination at 600 °C, which may in turn impact the physical properties on account of the known role of oxygen vacancies and defects on electron transport behavior of ZnO [26,27]. But in our case no such high temperature processing is required at any stage. Cho et al. [17] have used a solution method with tri-potassium citrate and trisodium citrate as additional reagents to grow the twinned ZnO NCs. The growth method they adopted involves multiple steps and is quite time consuming as zinc acetate dihydrate and ammonia solution containing citrates is initially kept at 90 °C for one hour in a Teflon-lined autoclave and subsequently dried in an oven at 60 °C for 12 hours. Taubert et al. [18-20] have employed different polymers to grow the twinned ZnO NCs, but the surface quality and flatness of their NCs are quite low compared to those synthesized in our case, which are almost atomically flat. In addition to that, none of the previous reports exhibit fabrication of well-aligned periodic arrays of ZnO NCs and site-specific growth, which is quite essential for their use in novel technological applications.

Conclusion

The growth of twinned nanocrystals of ZnO, 700 nm length and 600 nm width, with hexagonal prismatic shape has been demonstrated by employing a low-temperature single-step electrodeposition process, free of any supplementary reactants/additives, by creating low ion-flux conditions. It is further demonstrated that the ITO substrate patterned with a pore size of ≈600 nm provides site-specific growth centers for fabrication of ordered arrays of twin ZnO NCs with their *c*-axis [0001] perpendicular to the substrate plane. In contrast, a substrate patterned with a pore size of ≈200 nm (significantly smaller than the width of the NCs that form under uninhibited growth on the bare ITO surface) leads to the formation of coupled branched ZnO NCs. Plausible growth mechanisms underlying the formation of twinned crystals oriented/branched ZnO NCs are presented. The formation of twins seems to be facilitated by the linking of the two positively charged Zn polar surfaces of ZnO NCs by the negatively charged NO_2^- ions. The formation of branched structures is attributed to the constrained lateral growth due to limit imposed by the pore walls and the associated increase in surface energy. In the absence of such a constraint, for example, in the case where the pore size matches the crystal width, a vertically aligned twinned NC array is formed. Such a simple,

cost effective and large area, scalable fabrication of ZnO NC array potentially opens a path for new device possibilities with novel functionalities.

Acknowledgements

S.C. and D.K.P. acknowledge the financial support from DST under the Indo-Finland Project [INT/FIN/P-12]. V.D. and H.L. acknowledge support from the Academy of Finland project 284529. C.K. and V.K. would like to acknowledge the support of Aalto University's Doctoral school. We thankfully acknowledge Dr. Dinesh Kumar for helping in the discussion and manuscript writing.

ORCID® iDs

Rekha Bai - https://orcid.org/0000-0001-9080-0754
Dinesh K. Pandya - https://orcid.org/0000-0002-1604-1187
Sujeet Chaudhary - https://orcid.org/0000-0002-0535-6132
Vladislav Khayrudinov - https://orcid.org/0000-0002-4125-6104
Christoffer Kauppinen - https://orcid.org/0000-0002-2850-2702
Harri Lipsanen - https://orcid.org/0000-0003-2487-4645

References

1. Wei, Y.; Wu, W.; Guo, R.; Yuan, D.; Das, S.; Wang, Z. L. *Nano Lett.* **2010,** *10,* 3414–3419. doi:10.1021/nl1014298
2. Singh, A.; Senapati, K.; Satpati, B.; Sahoo, P. K. *Phys. Chem. Chem. Phys.* **2017,** *19,* 14012–14019. doi:10.1039/c7cp01880k
3. Son, N. T.; Noh, J.-S.; Park, S. *Appl. Surf. Sci.* **2016,** *379,* 440–445. doi:10.1016/j.apsusc.2016.04.107
4. Li, Q.; Kumar, V.; Li, Y.; Zhang, H.; Marks, T. J.; Chang, R. P. H. *Chem. Mater.* **2005,** *17,* 1001–1006. doi:10.1021/cm048144q
5. Kumar, D.; Bai, R.; Chaudhary, S.; Pandya, D. K. *Mater. Today Energy* **2017,** *6,* 105–114. doi:10.1016/j.mtener.2017.09.004
6. Bai, R.; Kumar, D.; Chaudhary, S.; Pandya, D. K. *J. Phys. Chem. C* **2018,** *122,* 14408–14419. doi:10.1021/acs.jpcc.8b04675
7. Mahalingam, T.; Lee, K. M.; Park, K. H.; Lee, S.; Ahn, Y.; Park, J.-Y.; Koh, K. H. *Nanotechnology* **2007,** *18,* 035606. doi:10.1088/0957-4484/18/3/035606
8. Huang, M. H.; Wu, Y.; Feick, H.; Tran, N.; Weber, E.; Yang, P. *Adv. Mater. (Weinheim, Ger.)* **2001,** *13,* 113–116. doi:10.1002/1521-4095(200101)13:2<113::aid-adma113>3.0.co;2-h
9. Rackauskas, S.; Mustonen, K.; Järvinen, T.; Mattila, M.; Klimova, O.; Jiang, H.; Tolochko, O.; Lipsanen, H.; Kauppinen, E. I.; Nasibulin, A. G. *Nanotechnology* **2012,** *23,* 095502. doi:10.1088/0957-4484/23/9/095502
10. Park, W. I.; Yi, G.-C.; Kim, M.; Pennycook, S. J. *Adv. Mater. (Weinheim, Ger.)* **2002,** *14,* 1841–1843. doi:10.1002/adma.200290015
11. Pan, Z. W.; Dai, Z. R.; Wang, Z. L. *Science* **2001,** *291,* 1947–1949. doi:10.1126/science.1058120
12. Zhang, T.; Dong, W.; Keeter-Brewer, M.; Konar, S.; Njabon, R. N.; Tian, Z. R. *J. Am. Chem. Soc.* **2006,** *128,* 10960–10968. doi:10.1021/ja0631596
13. Viswanatha, R.; Amenitsch, H.; Sarma, D. D. *J. Am. Chem. Soc.* **2007,** *129,* 4470–4475. doi:10.1021/ja068161b
14. Javon, E.; Gaceur, M.; Dachraoui, W.; Margeat, O.; Ackermann, J.; Saba, M. I.; Delugas, P.; Mattoni, A.; Bals, S.; Van Tendeloo, G. *ACS Nano* **2015,** *9,* 3685–3694. doi:10.1021/acsnano.5b00809
15. Greer, H. F.; Zhou, W.; Liu, M.-H.; Tseng, Y.-H.; Mou, C.-Y. *CrystEngComm* **2012,** *14,* 1247–1255. doi:10.1039/c1ce05958k
16. Chen, X.; Song, X.; Qiao, W.; Zhang, X.; Sun, Y.; Xu, X.; Zhong, W.; Du, Y. *CrystEngComm* **2016,** *18,* 9139–9151. doi:10.1039/c6ce02056a
17. Cho, S.; Jang, J.-W.; Jung, S.-H.; Lee, B. R.; Oh, E.; Lee, K.-H. *Langmuir* **2009,** *25,* 3825–3831. doi:10.1021/la804009g
18. Taubert, A.; Kübel, C.; Martin, D. C. *J. Phys. Chem. B* **2003,** *107,* 2660–2666. doi:10.1021/jp020569h
19. Taubert, A.; Palms, D.; Weiss, Ö.; Piccini, M.-T.; Batchelder, D. N. *Chem. Mater.* **2002,** *14,* 2594–2601. doi:10.1021/cm011670m
20. Taubert, A.; Glasser, G.; Palms, D. *Langmuir* **2002,** *18,* 4488–4494. doi:10.1021/la011799a
21. Sun, X.; Qiu, X.; Li, L.; Li, G. *Inorg. Chem.* **2008,** *47,* 4146–4152. doi:10.1021/ic702348c
22. Tang, L.; Ding, X.; Zhao, X.; Wang, Z.; Zhou, B. *J. Alloys Compd.* **2012,** *544,* 67–72. doi:10.1016/j.jallcom.2012.07.138
23. Kauppinen, C.; Haggren, T.; Kravchenko, A.; Jiang, H.; Huhtio, T.; Kauppinen, E.; Dhaka, V.; Suihkonen, S.; Kaivola, M.; Lipsanen, H.; Sopanen, M. *Nanotechnology* **2016,** *27,* 135601. doi:10.1088/0957-4484/27/13/135601
24. Singh, T.; Pandya, D. K.; Singh, R. *Opt. Mater.* **2013,** *35,* 1493–1497. doi:10.1016/j.optmat.2013.03.015
25. Ohring, M. *Materials Science of Thin Films,* 2nd ed.; Academic Press: Cambridge, MA, U.S.A., 2002; p 358. doi:10.1016/b978-0-12-524975-1.x5000-9
26. Rotella, H.; Mazel, Y.; Brochen, S.; Valla, A.; Pautrat, A.; Licitra, C.; Rochat, N.; Sabbione, C.; Rodriguez, G.; Nolot, E. *J. Phys. D: Appl. Phys.* **2017,** *50,* 485106. doi:10.1088/1361-6463/aa920b
27. Singh, A.; Chaudhary, S.; Pandya, D. K. *Acta Mater.* **2014,** *77,* 125–132. doi:10.1016/j.actamat.2014.05.048

License and Terms

BEILSTEIN JOURNAL OF NANOTECHNOLOGY

Development of an anti-pollution coating process technology for the application of an on-site PV module

Sejin Jung[1], Wonseok Choi*[1], Jung Hyun Kim[2] and Jang Myoun Ko[3]

Full Research Paper

Open Access

Address:
[1]Department of Electrical Engineering, Hanbat National University, Dajeon 34158, Republic of Korea, [2]Department of Advanced Materials Science and Engineering, Hanbat National University, Daejeon 34158, Republic of Korea and [3]Department of Chemical Engineering and Biotechnology, Hanbat National University, Daejeon 34158, Republic of Korea

Email:
Wonseok Choi* - wschoi@hanbat.ac.kr

* Corresponding author

Keywords:
annealing; anti-pollution; functional film; gas torch; PV module

Beilstein J. Nanotechnol. **2019,** *10,* 332–336.
doi:10.3762/bjnano.10.32

Received: 21 September 2018
Accepted: 04 January 2019
Published: 01 February 2019

This article is part of the thematic issue "Chemical thin coating methods for functional nanomaterials".

Guest Editor: J. Bachmann

Abstract

This study aimed to apply annealing processes during the coating of photovoltaic (PV) module glasses to PV modules already installed through an easy and simple procedure. Three types of annealing treatments were applied to PV module glasses, i.e., furnace, rapid thermal annealing (RTA) and torch. Among these, torch annealing, which can be easily carried out at PV module installation sites, was applied to PV module glasses using different numbers of repetition. Light transmittance, contact angle, anti-pollution characteristics, adhesion and hardness of the functional coating films after using different annealing treatment times and methods were measured, and it was confirmed that these characteristics varied depending on the annealing treatment times and methods. Through this, it was possible to optimize the process conditions that provide excellent anti-pollution characteristics and could be easily utilized at on-site PV modules.

Introduction

The worldwide consumption of fossil fuels has caused global warming through emitting carbon dioxide (CO_2) and greenhouse gases. To address this problem, continuous efforts have been made to reduce CO_2 emissions through the Paris Agreement in December 2015. In addition, as fossil fuels are expected to be depleted in approximately 130 years, the development of renewable energy sources that can replace fossil energy is required. Solar energy represents the highest proportion among the renewable energy sources, and it can produce clean electricity without noise or by-products [1,2]. Photovoltaic (PV) modules are installed outdoors and are thus exposed to various external surface pollutants, such as dust, yellow dust, animal excrement and rainfall sediment. These pollutants prevent sunlight from entering the PV modules and thereby degrade the power generation efficiency. Therefore, various studies have been conducted of late to effectively prevent the surface pollution of PV modules [3,4]. The PV module surface coating materials that are currently under research must have anti-pollution

functions and must endure severe temperature differences, and harsh physical (e.g., external shock) and chemical environments (e.g., animal excrement). They must also have a light transmittance of 95% or higher [5,6]. Large solar power plants are currently being installed for power generation, and a huge amount of time and cost is required for maintenance, including surface cleaning. Therefore, the introduction of a technology capable of easily removing pollutants using natural water will significantly improve the economic efficiency of the maintenance of solar power generation systems [7]. Although a self-cleaning coating technique using a photocatalyst has been developed, the durability is poor due to low adhesion and hardness. Also, production is very difficult, an energy source that causes catalytic action is needed, and the supply is low. In addition, anti-fogging and anti-condensation technologies have been applied to module production, but their anti-pollution effects are not significant [8,9].

In this study a new, easily usable coating technology is proposed that could be applied to PV modules already installed in the field to effectively improve the self-cleaning of the surfaces of PV modules. This technology should have the advantage of being applicable directly at the PV module installation site, without having to bring the module to the factory for modification. Before applying the coating technology to PV modules, glass substrates for PV modules were coated with a hydrophilic silica-based eco-friendly nanomaterial, and the coating films were thermally annealed using either a furnace, RTA or a torch. The annealing treatment that uses a torch was applied using different periods of time. For the fabricated specimens, the contact angle, anti-pollution characteristics, hardness, and adhesion were measured. The process conditions were optimized by analyzing the measurement results.

Experimental

The coating solution that was used to improve the anti-pollution characteristics of the PV modules contained silicon dioxide (SiO_2), lithium (Li), and potassium (K). The viscosity, density, and specific gravity (referring to the density of water) of the coating solution were 0.01–0.03 kg/m·s, 1.1 g/cm^3, and 1.13 ± 0.05, respectively. The solution can be used to coat various materials, such as metals, ceramics, and glass [9].

Before coating the glass slide substrates, the substrates were subjected to ultrasonic cleaning for 10 min in, consecutively, trichloroethylene, acetone, methanol and deionized water (DI water). The substrates were coated with the coating solution using a brush. After being dried at room temperature for 20 min, the substrates were thermally annealed using a furnace (L-Series, Jeio Tech Co., South Korea), RTA (RTP-1200, Nextron Co., South Korea), and a gas torch (KT-2211, Kovea Co., South Korea, using butane gas). The length of the flame was about 10 cm, the distance between the flame and the specimen was about 5 cm, and the temperature was about 300 °C. In addition, the annealing treatment that uses a gas torch, which can be easily utilized to surfaces of installed or operating PV modules, was applied from one to five times.

The contact angles of the fabricated functional coating films were measured using a contact angle analyzer (Phoenix 300 Touch, S.E.O. Co., South Korea). The anti-pollution characteristics were measured using permanent markers instead of actual pollutants. This method is useful for checking the level of pollutant removal. The hardness was measured using a hardness tester (CT-PC1, CORETECH Co., South Korea) equipped with pencils with hardness values from H to 9H (Mitsubishipencil Co., Ltd., Japan) in accordance with ASTM D3363 of the American Society for Testing and Materials (ASTM). The optical characteristics were measured using the integrating sphere of a UV–visible spectrophotometer (Mega 700, Scinco Co., Ltd., South Korea).

Results and Discussion

The light transmittance measurement results of the fabricated functional coatings are summarized in Figure 1. The light transmittance of the coating film thermally annealed at 300 °C using a furnace was determined to be 95.4%, and that of the coating film thermally annealed at 300 °C using RTA, 96.5%. When annealing treatment was performed one to five times using a torch, the light transmittance was found to be 91.3, 94.7, 98.3, 98.5, and 98.2%, respectively. The light transmittance increased for the first three times of torch annealing. After the fourth and fifth treatment the transmittance was similar to that after the third annealing.

Figure 2 and Figure 3 show the contact angle characteristics according to the annealing treatment method. The contact angle was 15.4° when the coating film was thermally annealed using a furnace, and it was 14.8° when the coating film was thermally annealed using RTA. When annealing treatment was performed one to three times using a torch, the contact angle was 24.3°, 15.5°, and 13.9°, respectively, but the contact angles in the fourth and fifth annealing treatments were similar to that in the third annealing treatment.

Figure 4 shows the anti-pollution characteristics after annealing treatment. Black, red, and blue markings were applied on the glass slide substrates coated with the functional coating solution, using oil pens. After the markings were naturally dried and cleaned with water, the specimens thermally annealed using a furnace, RTA, and three to five torch applications showed excellent anti-pollution characteristics. In particular, the speci-

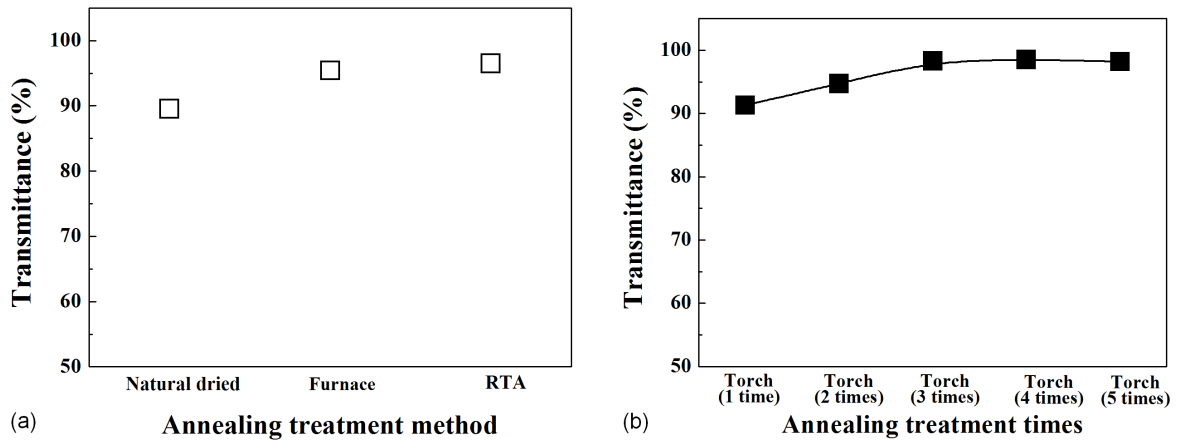

Figure 1: Transmittance (a) according to the annealing treatment method and (b) according to the number of annealing treatment using a gas torch.

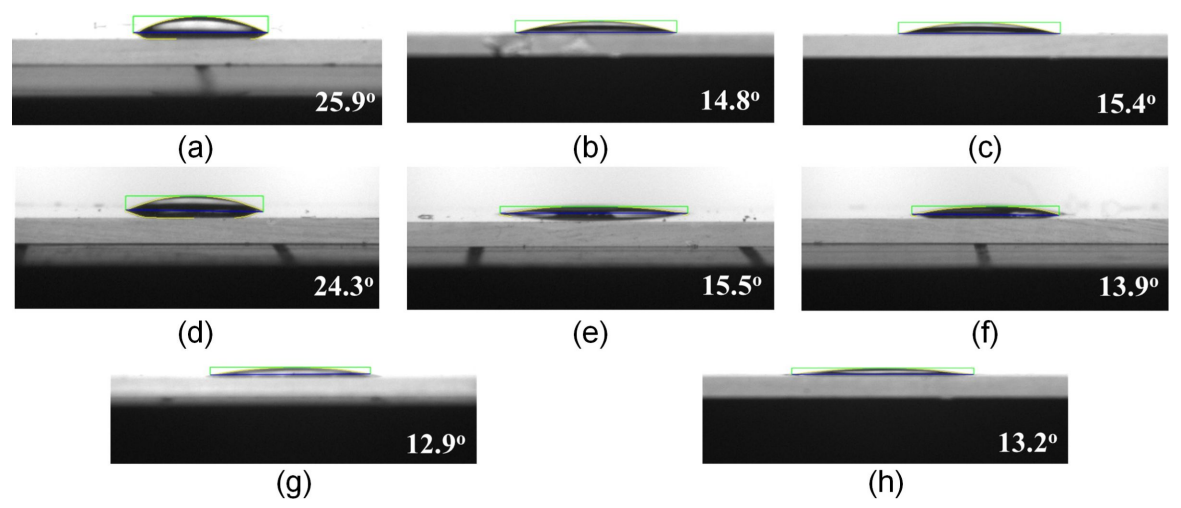

Figure 2: Contact angles of the coating films fabricated using various annealing treatment methods: (a) naturally dried; (b) annealed with RTA; (c) annealed with a furnace; (d) annealed once with a gas torch; (e) annealed two times with a gas torch; (f) annealed three times with a gas torch; (g) annealed four times a with gas torch; and (h) annealed five times with a gas torch.

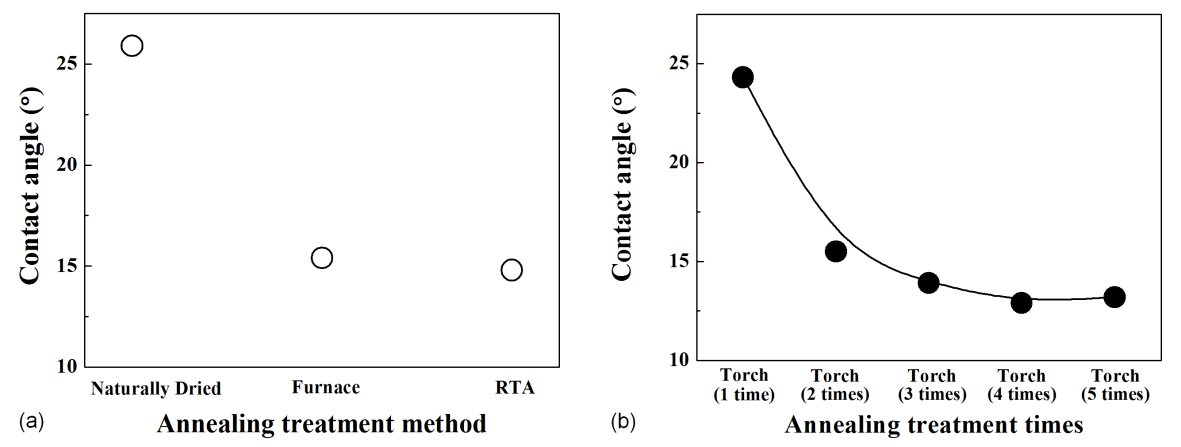

Figure 3: Contact angle by (a) annealing treatment method and (b) annealing treatment times using a gas torch.

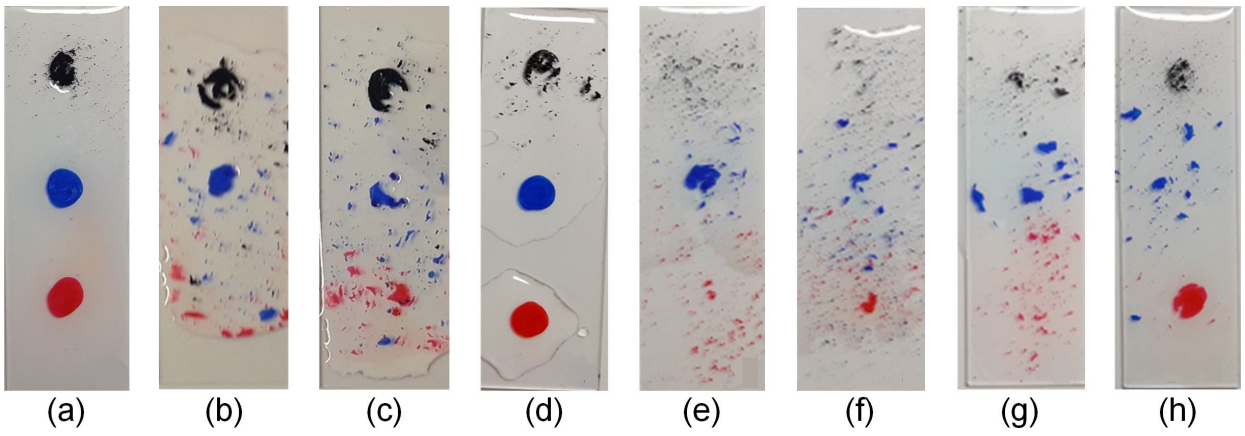

Figure 4: Anti-pollution characteristics of the coating films fabricated using various annealing treatment methods: (a) naturally dried; (b) annealed with RTA; (c) annealed with a furnace; (d) annealed once with a gas torch; (e) annealed two times with a gas torch; (f) annealed three times with a gas torch; (g) annealed four times with a gas torch; and (h) annealed five times with a gas torch.

mens thermally annealed using three to five torch applications exhibited the most excellent characteristics.

Figure 5 and Figure 6 show the hardness and adhesion characteristics when annealing treatment was performed on the coating films using a furnace, RTA, and one to five torch applications. For the analysis of the characteristics, the hardness values of the fabricated films were measured using a pencil hardness tester, in accordance with the ASTM D3363 criteria, and the adhesion values were measured in accordance with the ASTM D3359 criteria. All the annealed coating films exhibited 5B adhesion and 9H hardness, while the coating film that had been dried at room temperature exhibited 2B adhesion and 7H hardness.

Conclusion

A functional coating was applied to glass slide substrates to improve their anti-pollution characteristics for application in PV

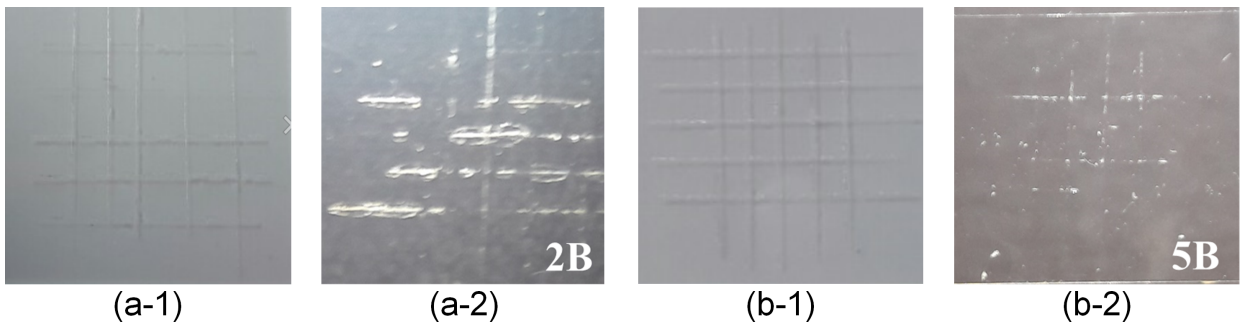

Figure 5: Adhesion characteristics of the coating films fabricated using various annealing treatment methods: (a-1) naturally dried; (a-2) coating film after the adhesion test; (b-1) annealed; and (b-2) coating film after the adhesion test.

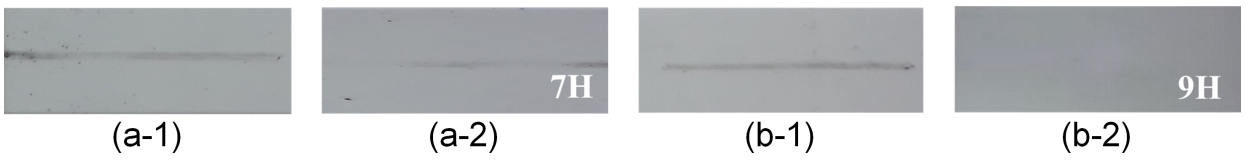

Figure 6: Hardness characteristics of the coating films fabricated using various annealing treatment methods: (a-1) naturally dried; (a-2) coating film after the hardness test; (b-1) annealed; and (b-2) coating film after the hardness test.

modules. After coating glass slide substrates made of the same material as glass substrates for PV modules with functional films, the results of naturally drying them or thermally annealing them with a furnace, RTA, or a torch were compared. In addition, annealing treatments with a torch were carried out one to five times to observe the changes in the sample characteristics. For the analysis of the characteristics of the fabricated specimens, light transmittance, contact angle, anti-pollution characteristics, hardness, and adhesion were measured.

The thermally annealed specimens showed 91.3% or higher light transmittance. In particular, when annealing using a torch three to four times, high light transmittance values of 98.3 and 98.5% were obtained. For the results of the contact angle analysis, the thermally annealed specimens showed a contact angle of 24.3° or lower. In particular, when annealing using a torch four to five times, the contact angles were 12.9 and 13.2°, respectively, indicating improvements in the hydrophilic characteristics. The analysis of the anti-pollution characteristics revealed that all the thermally annealed specimens exhibited improved anti-pollution characteristics. In particular, it was confirmed that the anti-pollution characteristics improved as the contact angle decreased. As for the measurement results of the hardness and adhesion, which are mechanical characteristics, all the thermally annealed substrates exhibited 9H hardness and 5B adhesion results, but the coating film that had been dried at room temperature showed 7H and 2B values. These results indicate that annealing treatment with a torch produces results similar to or better than those produced by annealing treatment with a furnace or RTA. Therefore, if the surfaces of PV modules installed outdoors are coated and thermally annealed with a torch, the annealing treatment process will be faster and easier. The results of this study confirm that the annealing treatment process using a torch can be applied directly to the installed PV module. On-site PV modules can be immediately processed without having to go to the factory, so it is expected that the amount of maintenance work will be reduced and that the economic efficiency will increase.

Supporting Information

Supporting Information File 1

Overview.
[https://www.beilstein-journals.org/bjnano/content/supplementary/2190-4286-10-32-S1.pdf]

Acknowledgements

This study was supported by Korea Electric Power Corporation (Grant No. R17XA05-01) and Korea Institute of Energy Technology Evaluation and Planning (Grant No. 20184030201900).

ORCID® iDs

Sejin Jung - https://orcid.org/0000-0002-9180-6397

References

1. Tyagi, V. V.; Rahim, N. A. A.; Rahim, N. A.; Selvaraj, J. A. *Renewable Sustainable Energy Rev.* **2013,** *20,* 443–461. doi:10.1016/j.rser.2012.09.028
2. Cao, F.; Chen, K.; Zhang, J.; Ye, X.; Li, J.; Zou, S.; Su, X. *Sol. Energy Mater. Sol. Cells* **2015,** *141,* 132–138. doi:10.1016/j.solmat.2015.05.030
3. Li, X.; Zhou, Y.; Xue, L.; Huang, L. *Technol. Forecast. Soc. Change* **2015,** *97,* 205–222. doi:10.1016/j.techfore.2014.05.007
4. Liu, C.; Zhang, X.; Li, J.; He, Y.; Li, Z.; Li, H.; Guo, W.; Xie, W. *Synth. Met.* **2015,** *204,* 65–69. doi:10.1016/j.synthmet.2015.03.012
5. Isshiki, M.; Sichanugrist, P.; Abe, Y.; Oyama, T.; Odaka, H.; Konagai, M. *Curr. Appl. Phys.* **2014,** *14,* 1813–1818. doi:10.1016/j.cap.2014.10.021
6. Yu, W.; Shen, L.; Shen, P.; Meng, F.; Long, Y.; Wang, Y.; Lv, T.; Ruan, S.; Chen, G. *Sol. Energy Mater. Sol. Cells* **2013,** *117,* 198–202. doi:10.1016/j.solmat.2013.06.002
7. Shan, B.; Kang, H.; Choi, W.; Kim, J. H. *Trans. Electr. Electron. Mater.* **2017,** *18,* 148–150.
8. Park, J. T.; Kim, J. H.; Lee, D. *Nanoscale* **2014,** *6,* 7362–7368. doi:10.1039/c4nr00919c
9. Joung, Y.-H.; Choi, W. S.; Shin, Y.; Lee, M.; Kim, H.; Song, W. *J. Korean Phys. Soc.* **2013,** *63,* 246–250. doi:10.3938/jkps.63.246

License and Terms

BEILSTEIN JOURNAL OF NANOTECHNOLOGY

Integration of $LaMnO_{3+\delta}$ films on platinized silicon substrates for resistive switching applications by PI-MOCVD

Raquel Rodriguez-Lamas[1], Dolors Pla[1], Odette Chaix-Pluchery[1], Benjamin Meunier[1], Fabrice Wilhelm[2], Andrei Rogalev[2], Laetitia Rapenne[1], Xavier Mescot[3], Quentin Rafhay[3], Hervé Roussel[1], Michel Boudard[1], Carmen Jiménez[1] and Mónica Burriel[*1]

Full Research Paper

Open Access

Address:
[1]Univ. Grenoble Alpes, CNRS, Grenoble INP (Institute of Engineering Univ. Grenoble Alpes), LMGP, F-38000 Grenoble, France, [2]European Synchrotron Radiation Facility (ESRF), F-38054 Grenoble, France and [3]Univ. Grenoble Alpes, CNRS, IMEP-LAHC, F-38000 Grenoble, France

Email:
Mónica Burriel[*] - monica.burriel@grenoble-inp.fr

* Corresponding author

Keywords:
manganite; metal organic chemical vapour deposition (MOCVD); resistive switching; thin film; valence-change memory

Beilstein J. Nanotechnol. **2019,** *10,* 389–398.
doi:10.3762/bjnano.10.38

Received: 10 October 2018
Accepted: 08 January 2019
Published: 07 February 2019

This article is part of the thematic issue "Chemical thin coating methods for functional nanomaterials".

Guest Editor: J. Bachmann

Abstract

The next generation of electronic devices requires faster operation velocity, higher storage capacity and reduction of the power consumption. In this context, resistive switching memory chips emerge as promising candidates for developing new non-volatile memory modules. Manganites have received increasing interest as memristive material as they exhibit a remarkable switching response. Nevertheless, their integration in CMOS-compatible substrates, such as silicon wafers, requires further effort. Here the integration of $LaMnO_{3+\delta}$ as memristive material in a metal–insulator–metal structure is presented using a silicon-based substrate and the pulsed injection metal organic chemical vapour deposition technique. We have developed three different growth strategies with which we are able to tune the oxygen content and Mn oxidation state moving from an orthorhombic to a rhombohedral structure for the active $LaMnO_{3+\delta}$ material. Furthermore, a good resistive switching response has been obtained for $LaMnO_{3+\delta}$-based devices fabricated using optimized growth strategies.

Introduction

Resistive switching (RS) denotes the phenomena occurring in capacitor-like heterostructures (metal–insulator/semiconductor–metal, MIM), namely memristors, when a non-volatile change of resistance is produced under the effect of an applied current or electric field [1]. As these resistance changes are reversible, RS is suitable for redox-based resistive switching random access memory (Re-RAM) applications, where different resistance values can be written, read and erased by applying the appropriate voltages. Typically two different states are characterized per device, i.e., a high-resistance state (HRS) and a low-resistance state (LRS).

As promising candidates for this application, manganites present large programming windows [2,3], i.e., a high ratio be-

tween HRS and LRS, as well as the possibility of multi-level resistance states [4], a clear advantage towards increasing storage density. The manganite of our choice is $LaMnO_{3+\delta}$ (LMO), as it is able to accommodate a wide range of cation and oxygen stoichiometry ($La_{1-y}MnO_{3-(3y/2)+\delta}$ and $LaMn_{1-z}O_{3-(3z/2)+\delta}$), which leads to changes in its electrical properties [5]. Here it is important to notice that for a La/Mn ratio of 1 $LaMnO_{3+\delta}$ corresponds to the simplified formula for cation deficient $La_{1-\varepsilon}Mn_{1-\varepsilon}O_3$, where $\varepsilon = \delta/(3 + \delta)$. The apparent oxygen excess in LMO films is expected to be compensated by a mixed valence state of the manganese cation (Mn^{3+}/Mn^{4+}).

Particularly, RS in LMO has been reported to be larger for oxygen vacancy-rich films [6,7]. Depending on the oxygen content (δ), the LMO structure changes from orthorhombic to rhombohedral at high δ [8]. This transition occurs around $\delta = 0.09$ at room temperature for a La/Mn ratio of 1:1 [5,9]. A similar transition from orthorhombic to rhombohedral with increasing oxygen content has also been reported for non-stoichiometric lanthanum manganites (La/Mn ≠ 1), for which, following Vegard's law, a linear variation of the lattice constants was observed with *y* and *z* for the orthorhombic samples, while a monotonic decrease of the rhombohedral angle α was observed for the rhombohedral samples [10].

In order to grow engineered LMO films, we chose the pulsed injection metal organic chemical vapour deposition (PI-MOCVD) technique, as it allows for a controlled growth of the perovskite phase over large areas (at wafer level) with high film uniformity and conformal coverage using liquid precursors at room temperature and under an inert atmosphere [11,12]. Both conventional MOCVD [13-15] and PI-MOCVD [16,17] have been used for the deposition of epitaxial and polycrystalline LMO and doped LMO thin films enabling the control of the oxygen and cation stoichiometry.

Since the precursor solution is simply prepared by dissolution of metalorganic species, the stoichiometry of the film is easily tuneable by changing their concentration. Besides, the PI-MOCVD technique offers the additional benefit of injecting micro droplets by using an electric valve granting excellent control over the quantity of precursor transferred to the reaction chamber and therefore a good control of the thickness of the films. Hence, by modifying a number of controlled parameters on the process, such as pulse frequency, oxygen partial pressure and temperature, the structure of the LMO thin films can be tuned during growth.

In memristors, the electrodes play a crucial role in the RS response. For example, in electrochemical metallization memory chips, ions from the electrode (such as Cu or Ag) [18,19] migrate to the other electrode generating a filament across the memristive material. Another example is the case of valence-change memories, in which the nature of the contact varies depending on the difference between the work functions of electrode and active material, creating an ohmic contact or a Schottky barrier. Furthermore, some electrodes can be oxidized forming a new interface layer that can also act as oxygen reservoir (e.g., Ti, TiO_2) [20-22]. The use of Pt as bottom electrode in our LMO-based devices guarantees an inert and ohmic contact, as the work function of LMO is 4.5–5.1 eV [23] and the one of Pt is 5.9–6.2 eV [24].

In order to integrate crystalline LMO memristive films in silicon-based devices, we used commercial platinized silicon as the bottom electrode/substrate heterostructure. Nevertheless, these substrates undergo dewetting when exposed to high temperatures for long times. The high temperatures required to grow perovskite thin films by techniques such as PI-MOCVD or PLD are a drawback because the continuity of the Pt bottom electrode can be lost [25]. In this work, we explore a number of different strategies to integrate LMO films on platinized silicon-based devices by PI-MOCVD, overcoming the challenge of the high temperatures required for their deposition. The growth parameters have been optimized to fabricate homogeneous and dense LMO films with different values of δ. Furthermore, we report the experimental proof of structural changes related to the growth strategy, being able to tune the LMO structure from an orthorhombic to a rhombohedral phase, as well as the changes in Mn^{n+} valence associated to this structure.

Experimental

LMO deposition conditions

$LaMnO_{3+\delta}$ (LMO) thin films were grown by pulsed injection metal–organic chemical vapour deposition (PI-MOCVD) in a JIPELEC reactor [26,27]. The precursor solutions were prepared using tris(2,2,6,6-tetramethyl-3,5-heptanedionato)lanthanum(III) [$La(thd)_3$] and tris(2,2,6,6-tetramethyl-3,5-heptanedionato)manganese(III) [$Mn(thd)_3$] commercial metal–organic precursors provided by Strem chemicals, and *m*-xylene (1,3-dimethylbenzene) solvent from Alfa Aesar. All solutions were prepared with a total metallic precursor concentration of 0.0225 M and a La/Mn precursor ratio of 2, the value of which was previously optimized to grow stoichiometric films with a La/Mn ratio close to 1.

The injection of the liquid precursors was performed using a frequency of 2.5 Hz and an opening time of 2 ms with a solution feeding rate of 0.35 mL/min. The evaporator was thermalized at 250 °C and Ar was used as carrier gas. The total pressure in the chamber was fixed at 5 Torr and oxygen gas was

added directly in the reaction chamber to obtain an oxygen partial pressure of 50%. Independent heaters and several thermocouples distributed along the reactor circuit allowed for a well-controlled heat gradient from the injector to the reaction chamber, maximizing the flux of carried precursor. The deposition temperature inside the main chamber (a hot-wall quartz reactor heated by an external furnace) ranged from 500 to 750 °C. The substrates used were 1 cm × 1 cm chips cut from a Pt (150 nm)/TiO_2 (40 nm)/SiO_2 (500 nm)/Si (111) wafer (VinKarola Instruments).

Structural and electrical characterization

Scanning electron microscopy (SEM) was performed in a Quanta250 environmental SEM FEG from FEI, and SEM FEG ZEISS GeminiSEM 500 to study the surface morphology and determine the LMO thickness using the cross section of the films. The cationic film composition was analyzed by semi-quantitative energy-dispersive X-ray analyses (EDX) using an Oxford Inca Energy detector coupled to the SEM. A combined study in X-ray diffraction (XRD) and Raman spectroscopy was performed to determine the crystal structure of the films and to detect the presence/absence of secondary phases. XRD was measured in grazing incidence configuration (GIXRD) in a 5-circle Rigaku Smartlab diffractometer to enhance the diffraction signal from the polycrystalline films and minimize the signal of the platinized silicon substrate. Raman spectra were collected using a Jobin Yvon/Horiba Labram spectrometer equipped with a liquid nitrogen-cooled CCD detector. Experiments were conducted in the micro-Raman mode in a backscattering geometry using a green laser (λ = 514.5 nm). The silicon spectrum at ambient temperature was always measured and used as reference to calibrate the LMO spectra. The nanostructure growth was further analyzed in cross section by transmission electron microscopy (TEM), a JEOL 2011 equipment operating at 200 kV with a 0.19 nm point-to-point resolution.

X-ray absorption near-edge spectroscopy (XANES) spectra at the Mn K-edge of LMO thin films were collected at the ESRF ID12 beamline (Grenoble, France). Measurements were taken under vacuum at 25 °C in fluorescence mode using a nearly constant 200 mA beam current. Two silicon photodiodes detectors were used to collect the total fluorescence, one in backscattering geometry and a second diode mounted at 90° with respect to the incident beam. The relative variation in the Mn formal valence was carried out from the experimental recorded inflection point after XANES spectra normalization, and using references found in the literature for other manganite perovskites [28].

The device fabrication for electrical measurements was performed in clean-room facilities combining laser lithography (Heidelberg instruments µPG 101) to define the top electrode pads (200 µm squared pads) and metal evaporation (Plassys MEB_{550} electron gun 10 kW) to grow 100 nm thick Au layer as top metal electrode. The electrical characteristics were measured under ambient conditions within a Faraday cage with microprobe manipulators using a B1500 Agilent semiconductor parameter analyzer.

Results and Discussion

Dense and homogeneous $LaMnO_{3+\delta}$ (LMO) thin films with variable oxygen content (δ) have been deposited by pulsed injection metal organic chemical vapour deposition (PI-MOCVD). The structural transition between orthorhombic and rhombohedral phases has been correlated with δ and the manganese oxidation state of the films. Furthermore, the tuned LMO films integrated in a silicon-based substrate showed resistive switching behavior as a proof-of-concept of the suitability of their use as ReRAM.

Optimisation of the deposition conditions

In this section we present the optimisation of the temperature and number of pulses using a fixed pressure of 5 Torr, a gas mixture composed of Ar 50% and O_2 50% during the deposition step, a pulse injection frequency of 2.5 Hz, and an opening time of the valve of 2 ms. These last two parameters allowed for a good evaporation of the precursors and a constant flux during deposition.

Samples grown at 675 °C and ca. 1 h of deposition time (i.e., 10000 pulses) evidenced the thermal instability of the platinum substrate surface. The main issues were Pt dewetting, the formation of pinholes at the LMO film, and/or LMO film cracking due to Pt grain evolution. The surface and the cross section of the heterostructures showing cracking of the sample, holes and Pt percolating to the surface are presented in Figure S1 and Figure S2, respectively, in Supporting Information File 1. In order to avoid these problems and with the aim of decreasing the time of exposure of the bare Pt surface to high temperatures, three strategies including different heating and deposition steps were proposed and tested, as shown in Figure 1.

(I) Single-step strategy: The reactor was heated at 25 °C/min in vacuum (ca. 0.15 Torr) up to the deposition temperature. Once the temperature was reached and stabilized (ca. 10 min), the gas mixture was introduced in the chamber and the injection of precursors started and ran for a limited deposition time (controlled number of pulses). Several deposition temperatures in the range of 650–700 °C were tested.

(II) Single-step strategy with annealing: The heating and deposition procedure was the same as described in strategy I, but

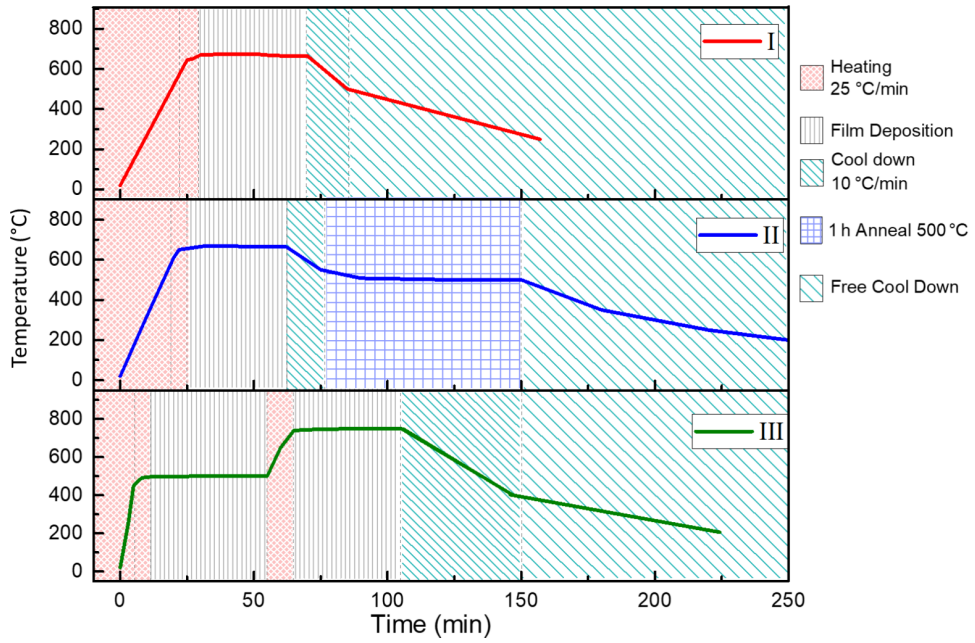

Figure 1: Growth diagrams of the three deposition strategies. The deposition steps correspond to temperature plateaus at 5 Torr using a gas mixture of 50% O_2 + 50% Ar. I) single-step strategy; II) single-step strategy with an annealing treatment (i.e., anneal in oxygen) at 500 °C and 5 Torr; III) two-step strategy scheme.

adjusting the deposition temperature between 660 and 680 °C. Once the injection was completed, an additional thermal treatment at 500 °C was performed. The samples were let to cool down to the post-deposition annealing temperature at a rate of 10 °C/min. At this temperature the environment was modified (i.e., annealing in oxygen) and the temperature was held for 1 h.

(III) Double-step strategy: This growth procedure was divided in two deposition steps at different temperatures. The first step consisted of depositing a stabilizing layer at an intermediate temperature (500 °C) and was followed by a second deposition step at high temperature (750 °C) to achieve the complete crystallization of the film. The heating conditions of the first step were the same as described in strategy I. Next, after a new heating ramp up to 750 °C (25 °C/min), the second deposition step took place once the temperature was reached. Cooling down began right after the injection was completed to minimize the time the sample was held at high temperature.

As common points to all strategies the mixture of gases (O_2/Ar) was introduced in the reactor chamber when a temperature 50 °C lower than the deposition temperature was reached. Controlled cool-down conditions varied depending on the desired structure (orthorhombic or rhombohedral). The samples were cooled down to an intermediate temperature (450–400 °C) using a cooling ramp of 10 °C/min in a specific gas environment (either pure Ar or O_2/Ar mixture in strategy I, and O_2/Ar mixture in strategies II and III). From this intermediate temperature, the cool-down rate was free and the pressure was kept at 5 Torr using only Ar gas. The influence of the atmosphere during cooling was investigated using strategy I through comparison of the effect of using either O_2/Ar mixture gas or pure Ar.

Figure 2 summarizes the LMO film growth as a function of the maximum temperature used and the period of time at which the samples were exposed to temperatures above 500 °C. This representation allows one to define the temperature region in which Pt remains thermomechanically stable, as well as the time limits to obtain dense and homogenous LMO films, i.e., without nanoporosities due to insufficient thickness, or the opening of grains in a flower bouquet-manner for thick films (see Figure S3 in Supporting Information File 1).

For strategy I, as a first approach samples were deposited at 500, 600 and 700 °C. At 600 °C the LMO layers showed low crystallinity whereas above 700 °C, diffusion of Pt across the film occurred, which may lead to short circuits in the final LMO-based device. The samples corresponding to this strategy are depicted as red squares in Figure 2. The points inside the shadowed green region correspond to deposition conditions for which dense and homogeneous LMO films are successfully obtained. The maximum appropriate temperature was 700 °C for times (above 500 °C) shorter than 45 min. This time limit could be increased (up to 50 min) for the deposition temperature range between 640 and 680 °C.

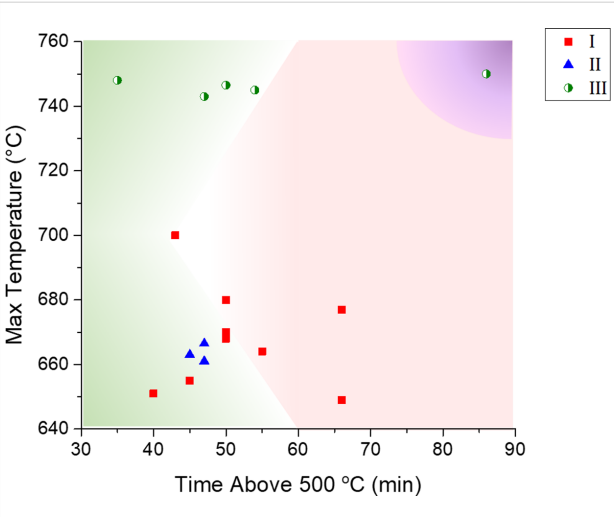

Figure 2: Representation of the range of appropriate deposition conditions. Maximum temperature used versus time of exposure to temperatures above 500 °C. Red squares stand for single step strategy (strategy I), blue triangles for single step strategy with in situ annealing (strategy II). Green circles stand for double step strategy (strategy III). Data in the green shadowed area correspond to successfully grown dense and homogeneous LMO films without instability issues. The red shadowed region corresponds to films with Pt instability problems. Purple area corresponds to columnar growth and opening of the grains, leading to porous films.

Strategy II was designed to obtain higher δ values in the LMO film by adding a post-deposition annealing step. LMO films were grown following strategy II (represented in Figure 2 by blue triangles) respecting the same critical limits established from strategy I. It was proved that despite the addition of a thermal annealing at 500 °C for 1 h, the selected conditions led to dense and homogeneous LMO films.

For strategy III, based on two consecutive deposition steps at 500 and 750 °C, the critical parameters were: (i) the LMO layer thickness obtained by growth at low temperature (d_1) to stabilize the Pt layer, and the LMO layer thickness corresponding to the second growth at 750 °C (d_2) that must fully cover the LMO film deposited first; (ii) the time at 750 °C, which must be sufficiently long to allow the bottom LMO layer to be fully crystallized but short enough to avoid Pt dewetting; (iii) the maximum thickness $d_1 + d_2$ (and the ratio between both thicknesses d_1/d_2) in order to obtain non-porous films (see Figure S2 in Supporting Information File 1), which is limited by the opening of grains in a flower bouquet-manner through columnar growth.

As previously explained, for strategies I and II, the time above 500 °C was limited to 45/50 min and the temperature should not exceed 700/685 °C during this time. This leads necessarily to a limitation in the LMO film thickness, which was of 60–80 nm for the fixed injection frequency of 2.5 Hz. Nevertheless, this limitation cannot be extrapolated to strategy III, for which the growth is stable for longer times, since the protective layer grown at 500 °C prevents Pt dewetting and Pt grain evolution.

The deposition time at 750 °C in strategy III was varied between 35 and 85 min. It is important to notice that strategy III allowed the growth of highly dense LMO films on Pt at 750 °C for longer deposition times, the Pt film was stable for all samples. In addition, the exposure times at 750 °C were enough to fully crystallise the LMO protective layer. From this point of view, strategy III is more robust than strategies I and II. Nevertheless, large thickness samples (green circle at 85 min above 500 °C in Figure 2) exhibit columnar grain opening that makes them inappropriate for device fabrication where flat surfaces are required. Besides, in strategy III, we have to take into consideration the effect of thicknesses d_1 (500 °C) and d_2 (750 °C), bearing in mind that d_1 should be thick enough to operate as protective layer and that d_2 should be continuous enough. Therefore, for this last strategy the minimum deposition time required above 500 °C is ca. 30 min, and the maximum time will be limited by the beginning of columnar opening, around 60 min.

In summary, the outcome of this optimisation process allowed for the determination of the optimal temperature/time range of growth for each strategy, i.e., the time limit before Pt begins dewetting, films begin to crack or nanoporosities begin to form. For films thicknesses smaller than 80 nm, strategy I and II are the most suitable, while strategy III is optimal for film thicknesses above 80 nm. In the latter case, the maximal thickness before columnar grain opening depends on d_1 and d_2 and will be subject of further studies.

Structural and composition characterisation of LMO thin films

In order to properly compare the films obtained by each strategy, structural and chemical studies were carried out by electron microscopy coupled to EDX. Within the resolution limit no differences in composition were observed for the different deposition strategies. Figure 3 shows the comparison of the surface films morphology with the same thickness (80–100 nm) grown by strategy I (Figure 3A), strategy II (Figure 3B) and strategy III (Figure 3C). All films are polycrystalline and highly compact with average grain sizes of 15 ± 4 nm, 18 ± 4 nm, and 22 ± 4 nm, respectively. Moreover, the LMO films are homogeneous and do not exhibit porosity, cracking or dewetting.

Furthermore, TEM cross-section observation of the LMO films was performed for strategies I and III, which correspond to the extreme cases (Figure 4). The cross-section images corrobo-

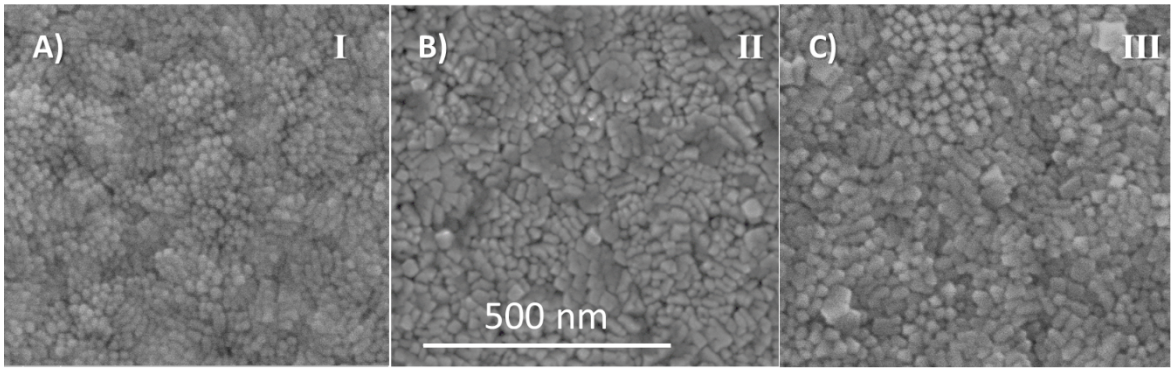

Figure 3: SEM surface images of the LMO films deposited by, A) strategy I, B) strategy II, and C) strategy III. The grain size increases from strategy I to III (i.e., 15, 18, 22 nm, respectively). All presented LMO thin films are of the same thickness of ca. 100 nm.

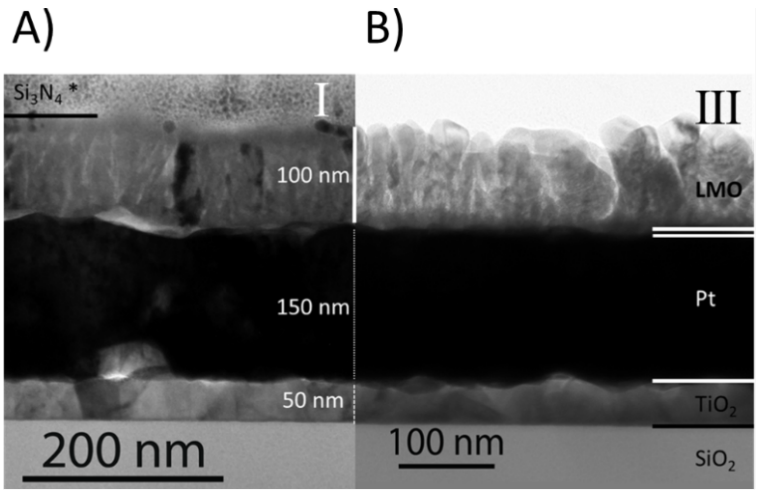

Figure 4: TEM cross-section images from LMO films grown by strategy I (A) and strategy III (B). A) A continuous and homogeneous film is observed. The Si_3N_4 coating marked with * comes from device fabrication. B) A homogeneous crystallization of LMO from bottom to top was achieved in the second deposition step.

rated that in both heterostructures the Pt layer is continuous and stable as required; neither dewetting nor Pt diffusion occurred at the interface. The good crystallization of both films was also verified, including the bottom part of the film for the case of strategy III (d_1 thickness), which was deposited at a lower temperature. The cross section of strategy III showed more irregular columns, probably due to the difference in growth temperature between the two steps, but no flower bouquet effect is observed for this thickness of ca. 100 nm.

The first step of the phase identification for the LMO films grown by strategies I, II and III was performed by GIXRD. The XRD patterns corresponding to representative LMO films deposited by the three strategies are shown in Figure 5.

All diffraction peaks can be attributed to the polycrystalline LMO perovskite phase without any clear preferential orientation and no impurities. Therefore, pure LMO can be obtained through all three deposition strategies. Nevertheless, the orthorhombic and rhombohedral patterns are quite similar and do not allow for an easy discrimination between both structures. Because the structure is strongly linked to the oxygen content, complementary structural characterization was carried out by Raman spectroscopy to identify the LMO phase. As reported by M. N. Iliev et al. [29], Raman spectroscopy is very sensitive to small changes in the LMO structure, allowing one to discriminate between the two phases. The orthorhombic phase is characterized by sharp Raman lines at high wavenumbers: A_g mode (in-phase stretching/out-of-phase bending) at 493 cm^{-1} and B_{2g} mode (in-phase stretching) at 612 cm^{-1}, while a weaker A_g mode (rotational) is observed around 257 cm^{-1}. On the other hand, the Raman spectrum of the rhombohedral phase is composed of broad bands centred at ca. 497 and 617 cm^{-1}, related to the Jahn–Teller distortion while weaker bands are ob-

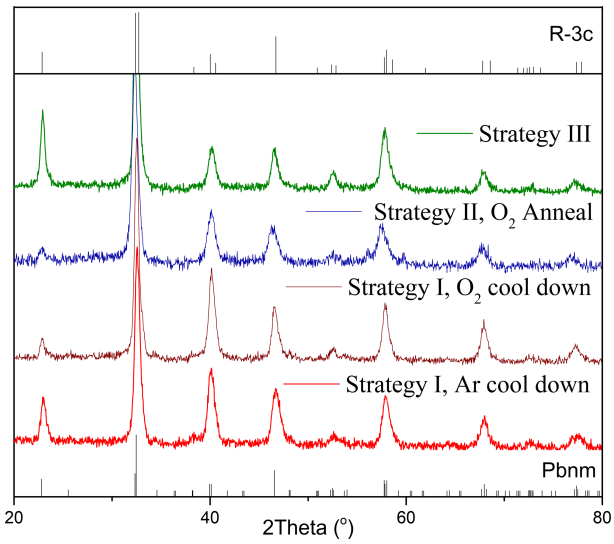

Figure 5: GIXRD patterns obtained for LMO thin films grown by strategy I (cooled in Ar and cooled in O_2), strategy II (1 h post-anneal in O_2) and strategy III. The orthorhombic (Pnma for $La_{0.974}Mn_{0.974}O_3$) and rhombohedral (R-3c for $La_{0.95}Mn_{0.95}O_3$) patterns have been added for comparison (ICDD: 01-087-2015 and 04-007-6350, respectively).

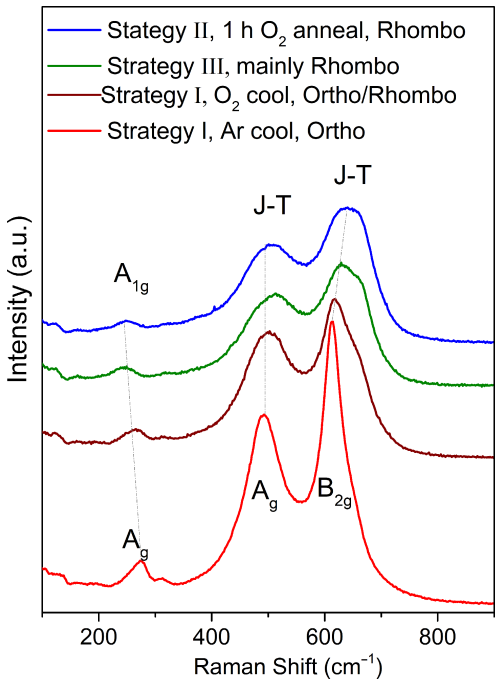

Figure 6: Raman spectra of LMO films obtained by the three deposition strategies under different conditions of cooling or annealing. An evolution of the structure from orthorhombic to rhombohedral phases is observed (dashed lines are guidelines for the eyes).

served at lower wavenumbers, such as the characteristic rotational mode, A_{1g}, at 217 cm^{-1}.

Figure 6 shows the evolution of the LMO Raman spectrum from an orthorhombic phase (bottom red curve) to a rhombohedral phase (top blue curve). At low wavenumbers, we can follow the evolution from the orthorhombic mode. At higher wavenumbers, a shift can be observed from the A_g and B_{2g} orthorhombic modes centred at 495 and 614 cm^{-1}, respectively, to the broad Jahn–Teller bands characteristic of mixed-valence manganites with Mn^{3+}/Mn^{4+} charge and orbital disorder [30], i.e., the first one at ca. 513 cm^{-1} and the second one split into a main band at ca. 630 cm^{-1} and a second component at ca. 660 cm^{-1} [31].

In Figure 6 we observe that pure orthorhombic and rhombohedral phases can be obtained for the two extreme deposition conditions. The LMO films obtained by strategy I show a pure orthorhombic phase when cooling down in Ar, which favours a lower oxygen incorporation in the LMO films. When the cooling is performed in O_2, the films contain a mixture of both phases since δ increases. The annealing step incorporated in strategy II, when performed under O_2 atmosphere, yielded a completely rhombohedral phase. Finally, the films grown using strategy III appear as mainly rhombohedral. Therefore, the Raman results give us an indication of the variation of the oxygen content in the LMO films from the structural phases observed.

The apparent oxygen excess in LMO films is expected to be compensated by a mixed valence state of the manganese cation (Mn^{3+}/Mn^{4+}). The variation of the Mn oxidation state for the same series of LMO films measured by Raman was confirmed by XANES (Figure 7). The local geometry of Mn was extracted from the pre-edge feature. For all the spectra, the absence of a sharp pre-edge shape reveals an octahedral (O_h) symmetry, i.e., a local symmetry of MnO_6 units, number of coordination = 6, which is in agreement with the perovskite structure [32]. The formal valence of Mn was estimated from the Mn K-edge position using reference values reported for the $LaMnO_3$ compound [28]. The Mn K-edge position was obtained from the inflection point of the absorption edges, calculated from the second derivative of the curves. The energy values obtained for the four LMO films are detailed in Table 1. As expected, the edge position increases with the Mn valence, being the lowest energy value the one of the orthorhombic LMO reference (strategy I, cooling in Ar) and the highest the one of the rhombohedral LMO reference (strategy II, annealing in O_2). The relative variation of the Mn formal valence was estimated comparing the shift in the Mn K-edge position with the one obtained in the literature [28]. Cuartero et al. measured an energy shift of 0.4 eV for an increase from Mn^{3+} to Mn^{4+}. Table 1 shows the estimated gradient in Mn formal valence among the four thin films, which is of 0.10 for the two extreme samples (rhombohedral and orthorhombic).

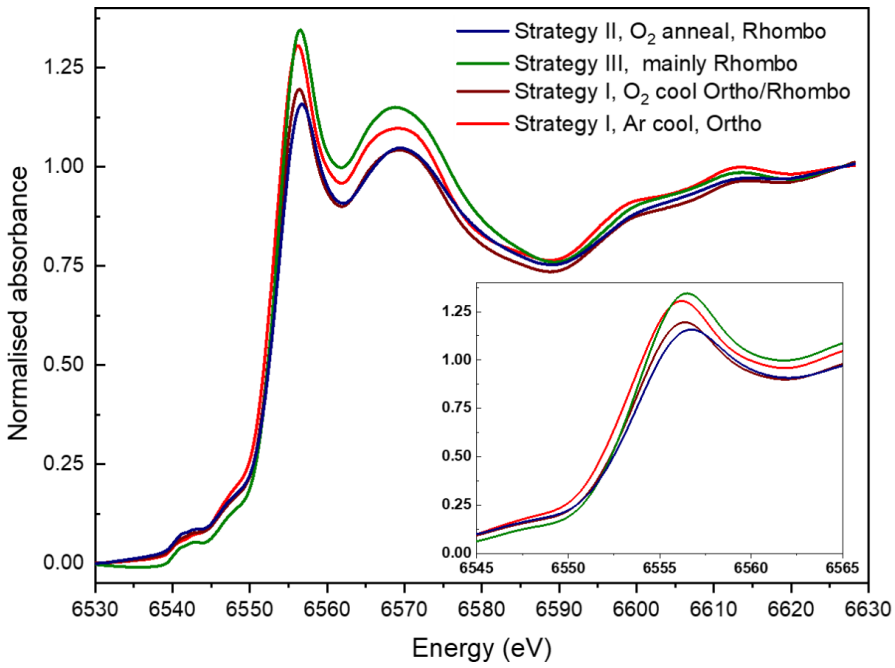

Figure 7: XANES absorption in Mn K-edge data of LMO films obtained by the three deposition strategies under different conditions of cooling or annealing (same samples as in Figure 6). The inset corresponds to an enlargement of the region close to the edge. An evolution of the structure from orthorhombic to rhombohedral phases is observed in good agreement with Raman spectra.

Table 1: Mn K-edge position for the four representative $LaMnO_{3+\delta}$ samples obtained by strategies I, II and III and estimated variation in the Mn formal valence taking as reference the orthorhombic sample.

LMO deposited films	Mn K-edge position (eV)	relative variation in Mn formal valence
strategy II (O_2 post-anneal) rhombohedral reference	6554.26	0.10
strategy III (double step) mainly rhombohedral	6554.22	0.09
strategy I (O_2 cooling) rhombohedral + orthorhombic	6554.00	0.04
strategy I (Ar cooling) orthorhombic reference	6553.85	0

All presented results confirm that it is possible to grow dense polycrystalline LMO films by PI-MOCVD adjusting the deposition conditions. Furthermore, we can tune the oxygen content and the resulting Mn oxidation state, leading to a structure transition from orthorhombic to rhombohedral phase. Considering the advantages and limitations of the three deposition strategies, despite the narrow temperature and time ranges required to avoid Pt instability, strategy I allows for the growth of LMO thin films up to 80 nm providing a very good control of the crystal structure. On the other hand, when rhombohedral films are suitable for the required application, the double-step strategy has proven to be more robust, allowing for the growth of thicker samples by adjusting the thicknesses d_1 and d_2.

Once the films were obtained we proceeded to the fabrication of MIM structures by evaporating squared Au electrodes of $200 \times 200\ \mu m^2$. Figure 8 presents the current–voltage characteristics of an orthorhombic LMO device. After a forming step, reproducible and reversible clockwise bipolar RS response was attained. The "set" and "reset" values were around −0.7 V and +0.6 V, respectively, which are considerably lower than those reported for epitaxial LMO (−1.5 V and +3.0 V) [6]. While the ratio of resistance of the "ON" and "OFF" states was of the same order as the one reported in the literature (over 7.3 in our case for polycrystalline LMO and between 1.8 and 18 depending on anneal conditions for epitaxial LMO [6]). Therefore, LMO films have proven their suitability as functional material for ReRAM applications.

Conclusion

After solving the issues related to the thermomechanical instability of Pt in the substrate, LMO films have been integrated on a platinized silicon substrate by using PI-MOCVD to fabricate perovskite-based ReRAM devices. To do so, three deposition strategies have been developed. All of them offer the possibility of growing dense and homogeneous LMO films suitable for

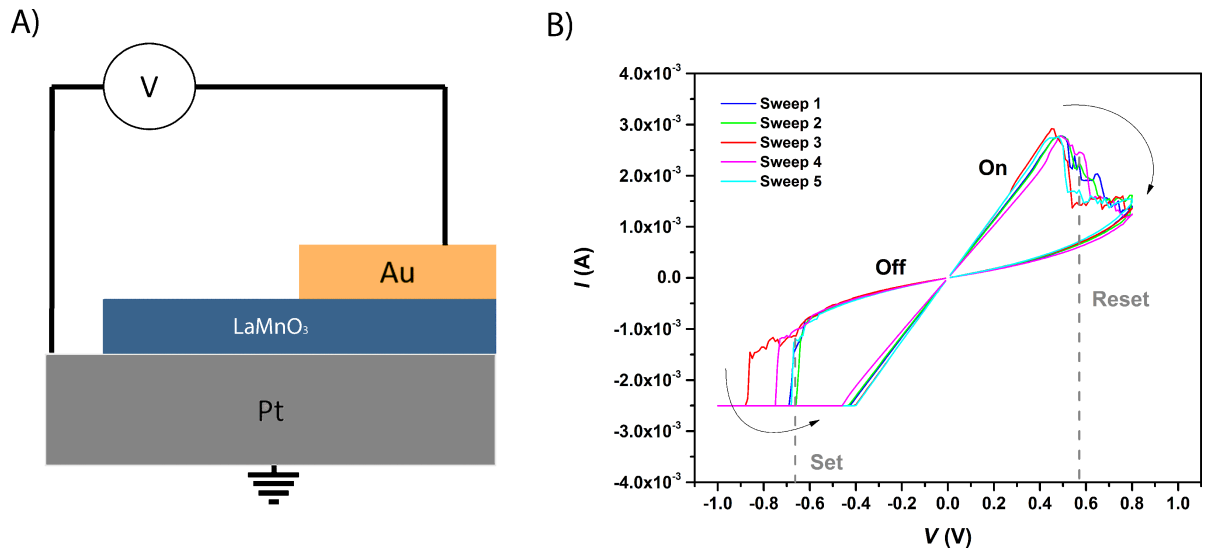

Figure 8: A) Cross section of the LMO-based MIM structure. B) Resistive switching cycles, *I–V* characteristics detailing the "set" and "reset" values.

resistive switching applications. Furthermore, the oxygen content can be tailored by adjusting the deposition parameters, such as temperature, number of pulses and atmosphere used during cooling. The transition from the orthorhombic to the rhombohedral phase has been correlated with the oxygen content and the Mn oxidation state of the LMO films. Orthorhombic films, as well as films with a mixture of phases have been obtained by using strategy I. With strategy II, which includes annealing in oxygen atmosphere, it was possible to obtain a purely rhombohedral structure. The third double-step strategy has proven to be a very robust method to grow mainly rhombohedral samples of comparable and higher thicknesses than the other strategies by adjusting the thicknesses d_1 and d_2. Therefore, by combining growth parameters in PI-MOCVD and wisely choosing the best deposition strategy we can tune the characteristics of the LMO films for functional devices. Finally, using Au and Pt as top and bottom electrodes, respectively, the functional resistive switching properties of the optimized LMO films has been validated.

Supporting Information

Supporting Information File 1

Additional figures.
[https://www.beilstein-journals.org/bjnano/content/supplementary/2190-4286-10-38-S1.pdf]

Acknowledgements

This work has been partially supported by the ANR funded "Alps Memories" project (ANR-15-CE24-0018) and has been performed with the help of the "Plateforme Technologique Amont" de Grenoble, with the financial support of the CNRS Renatech network. In addition, this work benefited from the facilities and expertise of the OPE)N(RA characterization platform of FMNT (FR 2542, fmnt.fr) supported by CNRS, Grenoble INP and UGA and from the facilities, and the scientific and technical assistance of the CMTC platform. This project has also received funding from the European Union's Horizon 2020 research and innovation program under the Marie Skłodowska-Curie Grant Agreement No. 746648 — PerovSiC (for D.P.) and from the "Microswitch" French ANR project (ANR-14-ACHN-0012) (for Mo.Bu.).

ORCID® iDs

Raquel Rodriguez-Lamas - https://orcid.org/0000-0002-0137-8174
Benjamin Meunier - https://orcid.org/0000-0001-5178-6427
Mónica Burriel - https://orcid.org/0000-0002-7973-7421

References

1. Waser, R.; Dittmann, R.; Staikov, G.; Szot, K. *Adv. Mater. (Weinheim, Ger.)* **2009,** *21,* 2632–2663. doi:10.1002/adma.200900375
2. Rubi, D.; Tesler, F.; Alposta, I.; Kalstein, A.; Ghenzi, N.; Gomez-Marlasca, F.; Rozenberg, M.; Levy, P. *Appl. Phys. Lett.* **2013,** *103,* 163506. doi:10.1063/1.4826484
3. Alposta, I.; Kalstein, A.; Ghenzi, N.; Bengio, S.; Zampieri, G.; Rubi, D.; Levy, P. *IEEE Trans. Magn.* **2013,** *49,* 4582–4585. doi:10.1109/tmag.2013.2258662
4. Stoliar, P.; Levy, P.; Sanchez, M. J.; Leyva, A. G.; Albornoz, C. A.; Gomez-Marlasca, F.; Zanini, A.; Toro Salazar, C.; Ghenzi, N.; Rozenberg, M. J. *IEEE Trans. Circuits Syst. II: Express Briefs* **2014,** *61,* 21–25. doi:10.1109/tcsii.2013.2290921

5. Xu, Z.-t.; Jin, K.-j.; Gu, L.; Jin, Y.-l.; Ge, C.; Wang, C.; Guo, H.-z.; Lu, H.-b.; Zhao, R.-q.; Yang, G.-z. *Small* **2012,** *8,* 1279–1284. doi:10.1002/smll.201101796
6. Jin, Y.-L.; Xu, Z.-T.; Jin, K.-J.; Ge, C.; Lu, H.-B.; Yang, G.-Z. *Mod. Phys. Lett. B* **2013,** *27,* 1350074. doi:10.1142/s0217984913500747
7. Töpfer, J.; Goodenough, J. B. *J. Solid State Chem.* **1997,** *130,* 117–128. doi:10.1006/jssc.1997.7287
8. Rodríguez-Carvajal, J.; Hennion, M.; Moussa, F.; Moudden, A. H.; Pinsard, L.; Revcolevschi, A. *Phys. Rev. B* **1998,** *57,* R3189–R3192. doi:10.1103/physrevb.57.r3189
9. Töpfer, J. *Solid State Ionics* **1997,** *101–103,* 1215–1220. doi:10.1016/s0167-2738(97)00153-7
10. Töpfer, J.; Goodenough, J. B. *Chem. Mater.* **1997,** *9,* 1467–1474. doi:10.1021/cm9700211
11. Dubourdieu, C.; Roussel, H.; Jimenez, C.; Audier, M.; Sénateur, J. P.; Lhostis, S.; Auvray, L.; Ducroquet, F.; O'Sullivan, B. J.; Hurley, P. K.; Rushworth, S.; Hubert-Pfalzgraf, L. *Mater. Sci. Eng., B* **2005,** *118,* 105–111. doi:10.1016/j.mseb.2004.12.019
12. Pla, D.; Jimenez, C.; Burriel, M. *Adv. Mater. Interfaces* **2017,** *4,* 1600974. doi:10.1002/admi.201600974
13. Bertrand, G. L.; Caboche, G.; Dufour, L.-C. *Solid State Ionics* **2000,** *129,* 219–235. doi:10.1016/s0167-2738(99)00328-8
14. Bosak, A. A.; Gorbenko, O. Y.; Kaul, A. R.; Graboy, I. E.; Dubourdieu, C.; Senateur, J. P.; Zandbergen, H. W. *J. Magn. Magn. Mater.* **2000,** *211,* 61–66. doi:10.1016/s0304-8853(99)00714-3
15. Snyder, G. J.; Hiskes, R.; DiCarolis, S.; Beasley, M. R.; Geballe, T. H. *Phys. Rev. B* **1996,** *53,* 14434–14444. doi:10.1103/physrevb.53.14434
16. Vincent, H.; Audier, M.; Pignard, S.; Dezanneau, G.; Sénateur, J. P. *J. Solid State Chem.* **2002,** *164,* 177–187. doi:10.1006/jssc.2001.9440
17. Pignard, S.; Vincent, H.; Sénateur, J. P.; Giauque, P. H. *Thin Solid Films* **1999,** *347,* 161–166. doi:10.1016/s0040-6090(98)01746-5
18. Tsuruoka, T.; Terabe, K.; Hasegawa, T.; Aono, M. *Nanotechnology* **2010,** *21,* 425205. doi:10.1088/0957-4484/21/42/425205
19. Guo, X.; Schindler, C.; Menzel, S.; Waser, R. *Appl. Phys. Lett.* **2007,** *91,* 133513. doi:10.1063/1.2793686
20. Herpers, A.; Lenser, C.; Park, C.; Offi, F.; Borgatti, F.; Panaccione, G.; Menzel, S.; Waser, R.; Dittmann, R. *Adv. Mater. (Weinheim, Ger.)* **2014,** *26,* 2730–2735. doi:10.1002/adma.201304054
21. Cabout, T.; Buckley, J.; Cagli, C.; Jousseaume, V.; Nodin, J.-F.; de Salvo, B.; Bocquet, M.; Muller, C. *Thin Solid Films* **2013,** *533,* 19–23. doi:10.1016/j.tsf.2012.11.050
22. Schroeder, H.; Jeong, D. S. *Microelectron. Eng.* **2007,** *84,* 1982–1985. doi:10.1016/j.mee.2007.04.042
23. Jacobs, R.; Booske, J.; Morgan, D. *Adv. Funct. Mater.* **2016,** *26,* 5471–5482. doi:10.1002/adfm.201600243
24. Derry, G. N.; Ji-Zhong, Z. *Phys. Rev. B* **1989,** *39,* 1940–1941. doi:10.1103/physrevb.39.1940
25. Garbayo, I.; Pla, D.; Morata, A.; Fonseca, L.; Sabaté, N.; Tarancón, A. *Energy Environ. Sci.* **2014,** *7,* 3617–3629. doi:10.1039/c4ee00748d
26. Sénateur, J. P.; Felten, F.; Pignard, S.; Weiss, F.; Abrutis, A.; Bigelyte, V.; Teiserskis, A.; Saltyte, Z.; Vengalis, B. *J. Alloys Compd.* **1997,** *251,* 288–291. doi:10.1016/s0925-8388(96)02699-0
27. Szkutnik, P. D.; Rapenne, L.; Roussel, H.; Lachaud, C.; Lahootun, V.; Weiss, F.; Jiménez, C. *Surf. Coat. Technol.* **2013,** *230,* 305–311. doi:10.1016/j.surfcoat.2013.06.063
28. Cuartero, V.; Lafuerza, S.; Rovezzi, M.; García, J.; Blasco, J.; Subías, G.; Jiménez, E. *Phys. Rev. B* **2016,** *94,* 155117. doi:10.1103/physrevb.94.155117
29. Iliev, M. N.; Abrashev, M. V. *J. Raman Spectrosc.* **2001,** *32,* 805–811. doi:10.1002/jrs.770
30. Iliev, M. N.; Abrashev, M. V.; Popov, V. N.; Hadjiev, V. G. *Phys. Rev. B* **2003,** *67,* 212301. doi:10.1103/physrevb.67.212301
31. Popov, S. E.; Nikiforov, A. E. *arXiv* **2003,** No. cond-mat/0307036. https://arxiv.org/abs/cond-mat/0307036
32. Farges, F. *Phys. Rev. B* **2005,** *71,* 155109. doi:10.1103/physrevb.71.155109

License and Terms

BEILSTEIN JOURNAL OF NANOTECHNOLOGY

Growth of lithium hydride thin films from solutions: Towards solution atomic layer deposition of lithiated films

Ivan Kundrata*[1,2,3], Karol Fröhlich[1,3], Lubomír Vančo[4], Matej Mičušík[5] and Julien Bachmann[2,6]

Full Research Paper

Open Access

Address:
[1]Institute of Electrical Engineering, SAS, Dúbravská cesta 9, 841 04 Bratislava, Slovakia, [2]Friedrich-Alexander University of Erlangen-Nürnberg, Dept. Chemie and Pharmacy, Chair "Chemistry of Thin Film Materials", Cauerstr. 3, 91058 Erlangen, Germany, [3]Centre of Excellence for Advanced Materials Application SAS, Dúbravská cesta 5807/9, 841 04, Bratislava, Slovakia, [4]STU Centre for Nanodiagnostics, Slovak University of Technology in Bratislava, Vazovova 5, 812 43 Bratislava, Slovakia, [5]Polymer Institute, Slovak Academy of Sciences, Dúbravská cesta 9, 845 41 Bratislava, Slovakia and [6]Saint Petersburg State University, Institute of Chemistry, Universitetskii pr. 26, 198504 St. Petersburg, Russia

Email:
Ivan Kundrata* - ivan.kundrata@savba.sk

* Corresponding author

Keywords:
lithiated thin films; lithium hydride; solution atomic layer deposition (sALD)

Beilstein J. Nanotechnol. **2019,** *10,* 1443–1451.
doi:10.3762/bjnano.10.142

Received: 14 February 2019
Accepted: 25 June 2019
Published: 18 July 2019

This article is part of the thematic issue "Chemical thin coating methods for functional nanomaterials".

Associate Editor: J. J. Schneider

Abstract

Lithiated thin films are necessary for the fabrication of novel solid-state batteries, including the electrodes and solid electrolytes. Physical vapour deposition and chemical vapour deposition can be used to deposit lithiated films. However, the issue of conformality on non-planar substrates with large surface area makes them impractical for nanobatteries the capacity of which scales with surface area. Atomic layer deposition (ALD) avoids these issues and is able to deposit conformal films on 3D substrates. However, ALD is limited in the range of chemical reactions, due to the required volatility of the precursors. Moreover, relatively high temperatures are necessary (above 100 °C), which can be detrimental to electrode layers and substrates, for example to silicon into which the lithium can easily diffuse. In addition, several highly reactive precursors, such as Grignard reagents or *n*-butyllithium (BuLi) are only usable in solution. In theory, it is possible to use BuLi and water in solution to produce thin films of LiH. This theoretical reaction is self-saturating and, therefore, follows the principles of solution atomic layer deposition (sALD). Therefore, in this work the sALD technique and principles have been employed to experimentally prove the possibility of LiH deposition. The formation of homogeneous air-sensitive thin films, characterized by using ellipsometry, grazing incidence X-ray diffraction (GIXRD), in situ quartz crystal microbalance, and scanning electron microscopy, was observed. Lithium hydride diffraction peaks have been observed in as-deposited films by GIXRD. X-ray photoelectron spectroscopy and Auger spectroscopy analysis show the chemical identity of the decomposing air-sensitive films. Despite the air sensitivity of BuLi and LiH, making many standard measurements

difficult, this work establishes the use of sALD to deposit LiH, a material inaccessible to conventional ALD, from precursors and at temperatures not suitable for conventional ALD.

Introduction

While the development of electric motors and semiconductor devices is progressing, the pressure on battery development is increasing correspondingly. Rechargeable, and if possible recyclable, batteries are versatile power sources for virtually all mobile devices. The advent of pocket hand-held devices places even stricter demands on the safety of rechargeable batteries. Although increased safety can be achieved using sophisticated and reliable charge-controller circuits, inherent safety is still desirable. Since the hazardous components in lithium-ion batteries are organic solvents used as electrolyte, their exclusion would greatly improve the inherent safety of lithium-ion batteries. Solid-state batteries that are already in use, such as the LIPON battery in which the solid electrolyte consists of nitrogen-doped lithium phosphate, present several shortcomings. One of them is the use of sputtering [1] for the deposition of the thin layers. Inherently, sputtering does not yield coatings with high conformity on non-planar substrates. Low conformity leads to low surface area and thick films are needed to avoid pinholes. This, in turn, leads to low capacity mainly due to the low surface area. The whole concept of a solid-state battery needs to be reconsidered, particularly if we wish to surpass the capacity of current liquid-electrolyte batteries. However, the natural obstacle of upscaling from the nanoscale to macroscopic batteries and large macroscopic capacities cannot be avoided. While a niche use can be found for wholly nanoscale batteries, such as a nanoscale batteries for nanoscale transistors, the scaling issue needs to be addressed for more general applicability. To meet this challenge, the use of atomic layer deposition (ALD) has been proposed [2,3]. The inherent conformity of ALD indeed allows for thinner, conformal, pin-hole free films [4,5].

ALD has been instrumental in enabling the development of nanobatteries, especially when combined with substrates of high surface area, which allow for increased capacity values. One such example is the V_2O_5–SnO_2 nanobattery [6] grown on anodized alumina. ALD can also deposit lithiated films, using precursors such as Li(thd), lithium *tert*-butoxide, and lithium hexamethyldisilazane [7]. Lithium hexamethyldisilazane enabled the direct deposition of deposit Li_2SiO_3 using ozone as a secondary precursor [7], at temperatures beginning at 150 °C, which are among the lowest for lithium ALD. Especially interesting is the ALD deposition of the aforementioned LIPON, which is currently the most popular solid-state electrolyte. Two approaches have been demonstrated in 2015. One is a quaternary process [8] adopting the lithium *tert*-butoxide and water process used to deposit Li_2O. To the cycle additional pulses of trimethylphosphate and nitrogen plasma were added, incorporating phosphorus and nitrogen into the Li_2O film at 250 °C. In the resulting LIPON films the nitrogen concentration could be varied between 0 and 16.3% [8]. Another approach to deposit LIPON using ALD is to incorporate nitrogen into the phosphorus precursors. Diethyl phosphoramidate has been successfully used in combination with lithium hexamethyldisilazane to deposit LIPON films [9]. The key insight was the use of a nitrogen-containing phosphorus precursor to directly create the P–N bonds. The resulting films grown by this technique at 270–330 °C were amorphous and the nitrogen concentration increased with the process temperature [9]. Despite these progresses, ALD has not yet been adopted to deposit lithium-containing films outside of laboratories, mainly due to the sensitivity of electrochemically active films to water, oxygen, and carbon dioxide. [7].

The deposition of lithiated compounds using conventional ALD uses expensive and complicated precursors, as well as relatively high temperatures. Especially high temperatures can be detrimental for the stability of lithiated films [10], because a part of the Li ions can diffuse [11] into substrates and devices. The use of several highly reactive precursors, such as Grignard reagents, which only exist in solution, could in theory allow for lower temperatures to be used. However, ALD cannot easily work with precursors that only exist in solution, or decompose below 100 °C. A novel ALD technique, namely solution atomic layer deposition [12] (sALD), opens up new ways to overcome these difficulties. In contrast to regular ALD, sALD uses solvents as precursor-carrying media, thereby eliminating the need for complicated gas supply lines and vacuum chambers, vastly simplifying the necessary setup for deposition. Furthermore, there is no need for complex filters for hazardous byproducts, since the liquid waste from the deposition process can be easily caught, neutralized, and the solvent can be recovered by distillation.

sALD opens up the possibility to use *n*-butyllithium, which does not exist in the gas phase, as a precursor for lithiated films [13]. Furthermore, such organolithium precursors in solution are inexpensive and easier to handle, more so than the required volatility of precursors for standard ALD would allow [7]. Because precursors that cannot be used in ALD are used in sALD, reactions that are impossible in the gas phase can be explored, even producing ionic compounds. Here we focus on

the reaction of BuLi with water in diethyl ether, exploring the deposition characteristics when using the sALD technique of sequential delivery of precursors in solution.

Experimental

Deposition setup

Initially, a deposition chamber made out of PTFE, which is shown schematically in Figure 1, was loaded with sample substrates. To close the chamber, a glass slide (see below in Figure 2) was sealed to the chamber with PTFE grease. The solutions were introduced into the chamber with stainless steel threaded pipes, which were connected to threads in the PTFE body of the chamber. Teflon tubes running through peristaltic pumps served as connections between the chamber and the needles in the precursors flasks, which were kept under nitrogen overpressure in a Schlenk line. All depositions were carried out at room temperature. Samples in the chamber during deposition can be seen below in Figure 3.

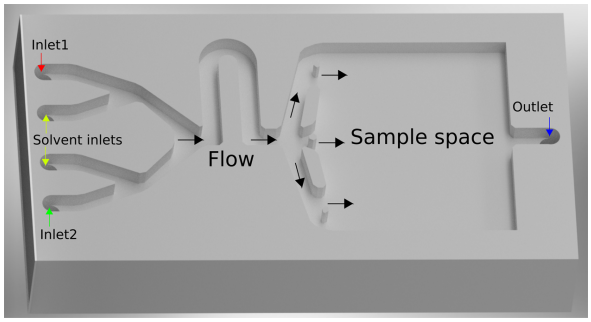

Figure 1: Illustration of the experimental deposition chamber. Top view, without cover. The chamber is closed from the top and then sequentially flooded with solutions.

Materials and methods

Precursors for the deposition were prepared in an argon-filled moisture-free glovebox, and then handled within a nitrogen-filled Schlenk line. Dry ether (ROTIPURAN 99.5%, p.a., lump), used as the primary solvent, was further dried with pure sodium and molecular sieves. *n*-Butyllithium (2.5 M in hexanes, Sigma) was diluted to 10 mM with diethyl ether. Deionized water was used as the complementary precursor, dissolved in diethyl ether (20 mM). The purging was carried out with nitrogen from the Schlenk line. In order to monitor the surface chemistry, a quartz crystal microbalance (QCM) system was installed behind the exit of the deposition setup with tubing of minimal length (2 cm), effectively allowing the deposition to occur on the QCM crystal as well. The waste pumped out of the QCM chamber was immediately neutralized with ethanol.

Contamination was a major limiting factor in the deposition setup. Examples of difficulties due to contamination include the loss of BuLi precursor when small amounts of air got into the reaction flask, and the repeating failure of the QCM measurement due to clogging and subsequent seal failure. Therefore, contamination was avoided as much as reasonably possible.

Measures for safe handling of *n*-butyllithium

Due to the pyrophoric nature of *n*-butyllithium these safety procedures were followed. (i) The *n*-butyllithium solution was handled in an argon-filled glovebox, set up specifically for precursor handling. (ii) The precursor was prepared in the glovebox and transferred into a Schlenk flask that was resealed, thus ensuring inert atmosphere during transfer. (iii) A concentration of 10 mM of *n*-butyllithium in diethyl ether was selected such that the energy released during the exothermic reaction between n-butyllithium and atmosphere would be insufficient to ignite the diethyl ether. This approach was tested and confirmed to work. Notably, the last step of this approach increases the sensitivity of the precursor to contamination, which was a major limiting factor, as mentioned before. However, safety was chosen as a priority, and contamination can be worked around. We expect such an approach to be scalable for use with larger deposition chambers, using more sophisticated and contamination-proof precursor flasks and delivery.

Deposition recipe

An example for a simple recipe used to deposit LiH: (i) The chamber was purged with pure solvent for 30 s. (ii) The solvent containing BuLi was pumped into the chamber for 10 s. (iii) The chamber was purged with pure solvent for 30 s. (iv) The solvent containing water was pumped into the chamber for 10 s.

Before, the deposition chamber was flushed with nitrogen for 1 min, and then with pure solvent for 2 min. The steps listed above were repeated for the desired number of cycles. After the last cycle was finished, a 1 min purge was performed to clean the chamber of any possible leftover precursors. Then the chamber was flushed with nitrogen from the Schlenk line, and only afterwards was the chamber opened. Since the deposition took place on the entire chamber, the film deposited on the glass slide could be used for further analysis. The chamber had to be cleaned with nitric acid after every deposition. Substrates of Si with native oxide and Pt/Si were used.

Characterization

Auger spectroscopy was carried out on a Auger microprobe Jeol JAMP-9510F with hemispherical analyser using 3 kV accelerating voltage and 10 nA probe current. Sample was tilted 55° to the excitation, with the normal coincident with the axis of the collection optics of the analyser. Point Auger spectra were collected from different areas on the surface of the sample after

20 s cleaning with 500 eV Ar^+ ions. Dwell time during the acquisitions was 100 ms with 1 eV measurement steps with an energy resolution of $\Delta E/E$ of 0.5 %. XPS signals were recorded using a Thermo Scientific K-Alpha XPS system (Thermo Fisher Scientific, UK) equipped with a micro-focused, monochromatic Al Kα X-ray source (1486.7 eV). An X-ray beam of 400 mm size was used at 6 mA and 12 kV. The spectra were acquired in the constant analyser energy mode with pass energy of 200 eV for the survey. Narrow regions were collected using the pass energy of 50 eV. Charge compensation was achieved with the system dual beam flood gun. The Thermo Scientific Avantage software, version 5.9904 (Thermo Fisher Scientific), was used for digital acquisition and data processing. Spectral calibration was determined by using the automated calibration routine and the internal Au, Ag and Cu standards supplied with the K-Alpha system. Argon etching was done with ion gun (1.4 μA of 2 keV Ar^+ ions over 8 mm^2).

The samples indented to be used in XPS and Auger were coated with an additional layer of SiO_2 inside of the deposition chamber. This protective layer of about 2 nm was sputtered away during measurements. However, the protection was unsuccessful. O_2 and CO_2 diffused in through to the film, which was proven by XPS measurements showing Li_2O and Li_2CO_3 after etching. This is described below in Table 1 and discussed further in subsection “Chemical Identity ”.

The surface compositions (in atom %) were determined by considering the integrated peak areas of the detected elements and the respective sensitivity factors. Grazing incidence X-ray diffraction was performed on a BRUKER D8 DISCOVER using the Cu Kα, at angle of incidence of 1°. The scan speed was changed as necessary. Ellipsometry measurements were performed using SENTECH SENpro ellipsometer, using the included halogen lamp. Frequency measurements on a quartz crystal were performed in situ using an OpenQCM module at 10 MHz.

Results and Discussion

Structure and possible reaction mechanism

Immediately after deposition, the chamber was opened, and the thin films visibly reacted with air, becoming whiter. This was markedly visible on the glass slides covering the chamber (Figure 2). During deposition, and before opening the chamber, the white film is not visible (Figure 3).

Therefore, GIXRD was performed immediately after deposition. The GIXRD pattern of an as-deposited sample from the BuLi + H_2O process reveals clear peaks of LiH as shown in Figure 4. Upon annealing at 600 °C peaks of Li_2O appear as expected based on the reaction of LiH with oxygen from air.

Figure 2: Chamber cover after deposition. The shape of the chamber is outlined by the PTFE paste used for sealing. A white film can be seen on the glass slide.

Figure 3: Samples in chamber during deposition, immediately before being taken out of the chamber. The glass slide was held in place by an acryl block, immediately upon removal of the block the chamber unsealed and the films started reacting with air.

It cannot be ascertained that the composition of the as-deposited films is pure LiH, since the reaction of H_2O and BuLi classically produces LiOH, at least in the presence of water in excess. However, thermodynamic considerations demonstrate that in fact lithium hydride and the concomitant reaction byproduct butanol are more stable than lithium hydroxide (and butane). The Gibbs free energy of formation [14] of the possible reaction products is:

$$\mathrm{LiOH + BuH \rightleftharpoons LiH + BuOH},\ \Delta G^\circ = -152\ \mathrm{kJ/mol}.$$

In other words, the driving force for generating LiH from BuLi and H_2O is significantly larger than that for generating LiOH (unless a large excess of water is present to cause the subse-

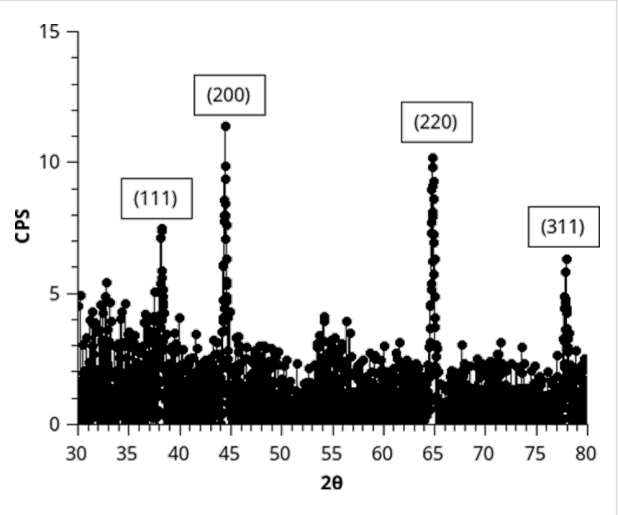

Figure 4: GIXRD of as-deposited samples with indexed reflections attributed to cubic LiH. GIXRD was performed at an incidence angle of 1°, and a scan speed 0.02° per 14.5 seconds.

quent reaction of the initially formed LiH under generation of H_2).

A likely reaction mechanism is sketched in Figure 5. The chemical identity of the surface alternates between hydride-terminated and butyl-terminated. While the water step releases butanol as a byproduct, the BuLi step results in a non-dissociative chemisorption of the precursor onto the surface.

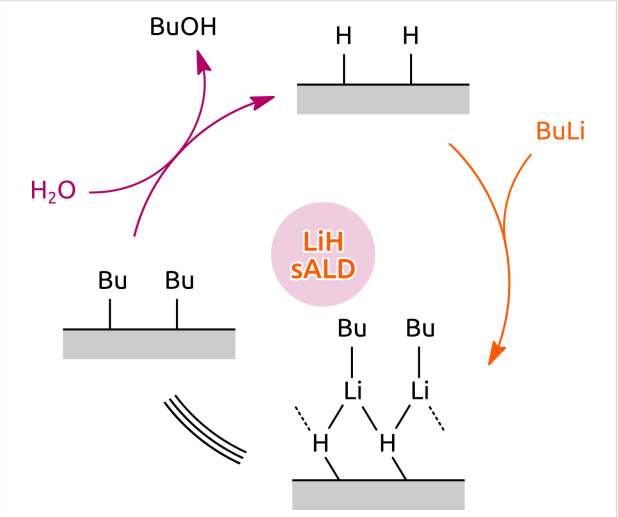

Figure 5: Possible mechanism of the surface reactions.

Chemical identity

The presence of LiH revealed through XRD needs to be confirmed by chemical analysis methods. Unambiguous analyses are rendered impossible by the air-sensitive nature of the deposit and the difficulty to identify the elements Li and H with techniques based on X-rays. In spite of this, the chemical nature of the film can be worked out from the presence of degradation products of LiH when combined with the XRD structural data. The exposure of LiH to ambient air generates two main degradation products [15,16] according to the reactions $LiH + H_2O \rightarrow Li_2O + 2H_2$ and $2LiH + CO_2 + 0.5O_2 \rightarrow Li_2CO_3 + H_2O$.

As expected, no LiH was measured on the surface by using Auger spectroscopy. However, the presence of Li_2O is shown in Figure 6. Because Auger spectroscopy is technically able to detect LiH [16], we assume that the LiH was degraded completely by the time of the measurement. XPS, which cannot detect LiH, was carried out complementary to Auger spectroscopy, to measure the presence of Li_2O and Li_2CO_3. XPS confirmed the presence of lithium on the surface and a Li 1s peak centred at 55.2 eV was detected (Figure 7a). This position of the Li 1s peak might correspond to Li_2CO_3[17] as well as to Li_2O [18]. The C 1s spectrum exhibits three peaks shown in Figure 7b. The peak centred at 285.1 eV corresponds to C–C/adventiteous carbon, the second peak centred at 286.6 eV corresponds to C–O, and the third peak centred at 289.4 eV corresponds to the CO_3 group [19]. These results are in agreement with the signals from the O 1s spectrum , shown in Figure 7c, with one peak at 531.9 eV (CO_3 group) and one signal at 533.6 eV (C–O). Additionally, there is also a third small signal at 530.1 eV, which might correspond to Li_2O [20]. This peak becomes more pronounced after the removal of the top 2 nm of the sample surface through Ar etching during XPS measurements (Table 1). After etching, also the stoichiometry of CO_3 becomes more clear, because signals from surface contaminations overlapping this signal in the C 1s spectrum, such as carboxyl groups, were removed.

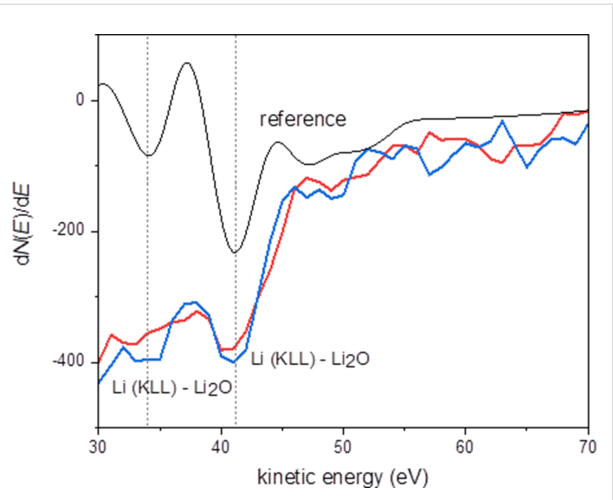

Figure 6: Derivative Auger spectra confirming the presence of Li_2O on the surface, acquired at two different areas of the sample (red and blue), shown together with the internal reference for Li_2O (black).

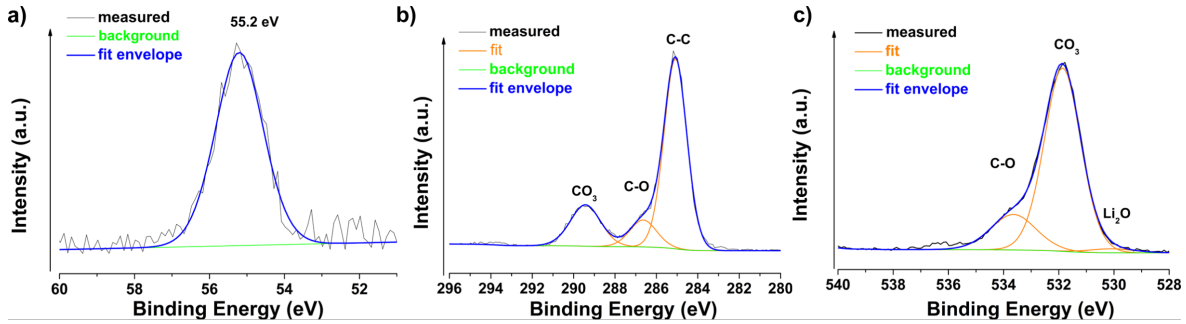

Figure 7: XPS spectra before Ar sputtering of a) Li 1s region, b) C 1s and c) O 1s region.

Table 1: Chemical composition of the sample surface as determined by XPS.

sample	surface chemical composition (atom %)		
	C 1s C–C/C–O/CO_3	O 1s Li_2O/CO_3/C–O	Li 1s
surface	37.3/6.2/10.8	0.6/22.3/5.3	17.4
after etching (approx. 2 nm)	19.2/2.8/9.5	4.3/31.5/1.6	31.0

Table 1 shows that Li occurs mostly as Li_2CO_3. When subtracting the signals of Li_2O (ca 2 atom % Li in Li_2O, calculated from the O 1s signal) and Li_2CO_3 (21 atom % Li in Li_2CO_3, calculated from O 1s signal) from the total Li content calculated from the Li 1s signal, there is a difference of ca. 8 atom %. Hence, there might be LiH present in the layer. While contamination with oxygen is possible during deposition, by leaks or improper drying of solutions, a contamination from carbon during deposition was only possible if small amounts of CO_2 leaked into the solvent vessels or the reaction chamber. The solvent itself acts as carrier and does not decompose. Decomposition products from the reaction between BuLi and diethyl ether could contaminate the films. This was avoided by always mixing fresh solutions before deposition. Therefore the carbon in the layer is assumed to come from the exposure of LiH films to CO_2 in the atmosphere. Together, Auger and XPS measurements showed that the LiH film degraded into a mixture of Li_2O and Li_2CO_3. Thus, when combined with the structural data obtained immediately after deposition, we can ascertain with high degree of confidence that the original film was indeed LiH.

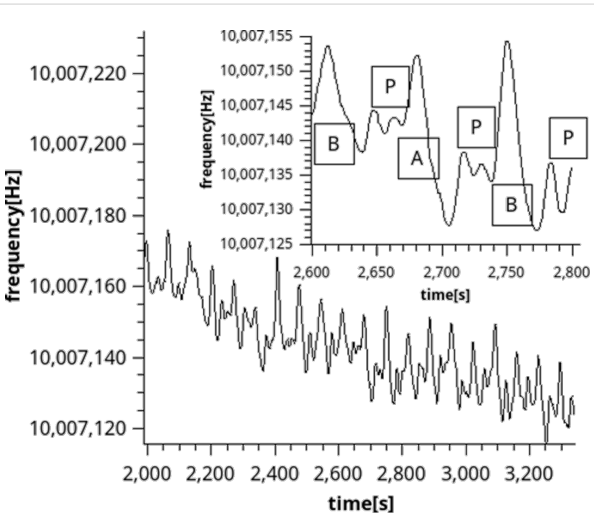

Figure 8: In situ QCM results, showing approximately 18 sALD cycles. The maxima and minima correspond to the timing of the sALD process. The inset shows the formation of small plateaus before the next peak. “A” corresponds to the BuLi flow, “B” corresponds to the water flow, and “P” corresponds to the purging.

Growth behaviour

QCM used during the deposition showed a linearly decreasing trend in frequency, clearly distinguishable from background noise (Figure 8). Moreover, the periodical changes also correspond to the changing cycles. The sharp increase in frequency during water cycles, marked “B” in the inset of Figure 8, is assumed to correspond to the relatively heavy butanol leaving the surface (see Figure 5). The plateau normally expected while using QCM to measure ALD reactions does not show clearly, possibly due to the connection of the QCM to the deposition chamber which causes a lag in the flow. However, a reasonable formation of plateaus, marked as “P” is shown in the inset of Figure 8. While longer purge times would lead to more pronounced plateaus, this would also mean an increased risk of contamination. In addition, the QCM was susceptible to leaks

and blowbacks, therefore capturing a longer cycle proved to be difficult. Despite contamination being an issue preventing the use of QCM for saturation measurements, valuable information was gained from shorter cycle runs. The QCM results were not converted from frequency to mass, due to the complexity of the QCM crystal resonating in a fluid. The standard approximations for gases do not apply, and since both the surface and the fluid repeatedly changed, a more complex simulation would be necessary to obtain all the parameters necessary for converting frequency to mass [21,22]. Therefore the frequency change is shown, indicating and increase in mass with decrease of frequency [21].

SEM images of the surface show clusters of crystals that grew possibly due to bubbles forming in the chamber shown in Figure 3 or the influence of air sensitivity. One such crystal is presented in Figure 9. The film covering the sample appears to be homogeneous and rough as seen in Figure 9.

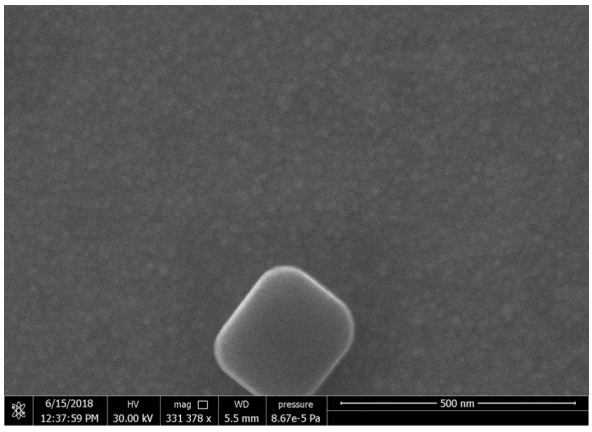

Figure 9: SEM of the Si/Pt sample surface after deposition and exposure to atmosphere. The large crystal seen is attributed to CVD growth in bubbles. The rough film is visible around the crystal.

Cross-sectional SEM was performed to estimate the film thickness as a reference for spectroscopic ellipsometry (Figure 10). Based on the SEM image, a Cauchy model was created with a constant thickness of 45 nm while all other parameters were fitted. This model was then used further, to enable ellipsometry measurements shortly after deposition. In this case, only the relative difference in thickness between samples could be measured, because the estimate from the cross-sectional SEM image was a rough estimate. Due to the relatively slow speed of the deposition and the high risk of contamination during long runs, only a few thick samples were prepared as cross sections. Spectroscopic ellipsometry measurements to determine the growth curve were performed directly after deposition (Figure 11).

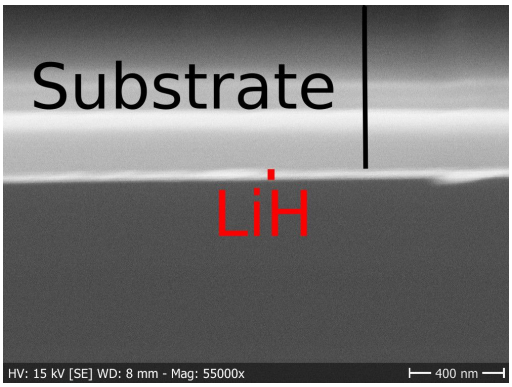

Figure 10: SEM of a Si sample cleaved after deposition. The film thickness was estimated to be roughly 45 nm.

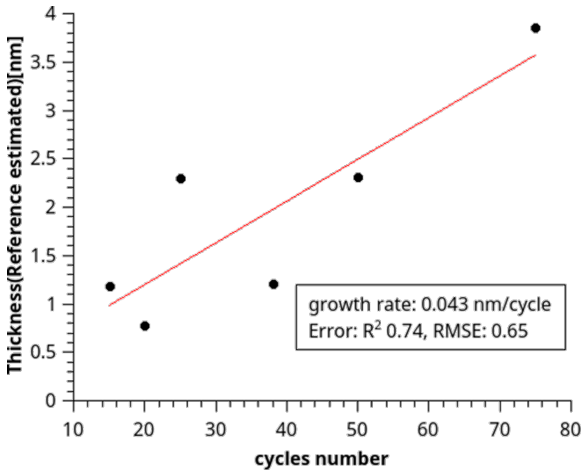

Figure 11: Growth curve obtained from spectroscopic ellipsometry. The thickness is relative to the SEM cross-section sample. The differences in thickness are correct.

The deviations from the fit, RMSE = 0.65, in Figure 11, are significant due to the instability of LiH films in air. For saturation this deviation causes the measurement to be indeterminate. In order to measure the saturation curve, further improvements of the sALD system are necessary, especially a construction of a glovebox-compatible sALD system. However, the growth rate (growth per cycle) of 0.43 Å/cycle is in line with expectations. Overall, the results indicate that an ALD process occurred with a definite growth per cycle, albeit its saturation has yet to be determined.

Discussion

The experiment indicates that the reaction between BuLi and water can indeed create LiH, in agreement with theoretical considerations concerning the formation of LiH under dry, stoi-

chiometric conditions. While a direct confirmation, through Auger spectroscopy measurements, of LiH would be desirable, the combination of structural data with the chemical identity of the degraded films has allowed us to be confident in claiming the film upon deposition was indeed LiH. Moreover, not only was it shown that the reaction produces LiH when used in the sALD deposition process, there are indications that the process is linear with respect to cycle number, according to the QCM measurements where the trend is a linear decrease in frequency. Ellipsometry measurements support the linearity of growth with cycle number as well, despite the larger error caused by the air sensitivity of the films. In addition, the films are crystalline as deposited, despite the fact that the deposition occurs at room temperature.

Conclusion

To conclude, we have, for the first time, deposited LiH thin films by the sequential flooding of a deposition chamber with precursor solutions, more precisely, by using BuLi as a simple and highly reactive precursor. Furthermore, the films were crystalline when deposited at room temperature, making further post-processing unnecessary.

The air sensitivity of this solid requires in situ materials characterization using methods such as spectroscopic ellipsometry, XPS and Auger spectroscopy. Further development of the process, especially more sophisticated chambers that would allow one to work in a glovebox are necessary to further characterize the LiH deposition process. In particular, the measurement of the saturation curve without contamination is necessary to determine the nature of the process. The development of such new sALD setup would open up the possibility to research new growth processes that are also difficult to perform because of air-sensitivity.

Despite the yet undetermined nature of the process, this novel deposition method of LiH opens up the possibilities for further studies of using sALD in battery applications. Furthermore, LiH is not only suitable as an electrode material, where in fact it boasts the highest lithium concentration after elemental Li, it is also extremely useful as a hydrogen-torage layer. Since sputtering of LiH is possible [23,24], but not conformal, the sALD growth of LiH enables research regarding applications in electrodes, hydrogen storage [25], fuel cells [26,27], and neutron shielding [28].

Acknowledgements

The author I.K. wishes to acknowledge the great help from, and the good spirit of the Bachmann group at FAU Erlangen. Also, we wish to acknowledge the financial support from the project VEGA 2/0136/18.

ORCID® iDs

Karol Fröhlich - https://orcid.org/0000-0002-9282-8942
Julien Bachmann - https://orcid.org/0000-0001-6480-6212

References

1. Nimisha, C. S.; Rao, K. Y.; Venkatesh, G.; Rao, G. M.; Munichandraiah, N. *Thin Solid Films* **2011,** *519,* 3401–3406. doi:10.1016/j.tsf.2011.01.087
2. Wen, L.; Zhou, M.; Wang, C.; Mi, Y.; Lei, Y. *Adv. Energy Mater.* **2016,** *6,* 1600468. doi:10.1002/aenm.201600468
3. Puurunen, R. L. *J. Appl. Phys.* **2005,** *97,* 121301. doi:10.1063/1.1940727
4. Pearse, A. J.; Schmitt, T. E.; Fuller, E. J.; El-Gabaly, F.; Lin, C.-F.; Gerasopoulos, K.; Kozen, A. C.; Talin, A. A.; Rubloff, G.; Gregorczyk, K. E. *Chem. Mater.* **2017,** *29,* 3740–3753. doi:10.1021/acs.chemmater.7b00805
5. George, S. M. *Chem. Rev.* **2010,** *110,* 111–131. doi:10.1021/cr900056b
6. Liu, C.; Kim, N.; Rubloff, G. W.; Lee, S. B. *Nanoscale* **2017,** *9,* 11566–11573. doi:10.1039/c7nr02151h
7. Nilsen, O.; Miikkulainen, V.; Gandrud, K. B.; Østreng, E.; Ruud, A.; Fjellvåg, H. *Phys. Status Solidi A* **2014,** *211,* 357–367. doi:10.1002/pssa.201330130
8. Kozen, A. C.; Pearse, A. J.; Lin, C.-F.; Noked, M.; Rubloff, G. W. *Chem. Mater.* **2015,** *27,* 5324–5331. doi:10.1021/acs.chemmater.5b01654
9. Nisula, M.; Shindo, Y.; Koga, H.; Karppinen, M. *Chem. Mater.* **2015,** *27,* 6987–6993. doi:10.1021/acs.chemmater.5b02199
10. Putkonen, M.; Aaltonen, T.; Alnes, M.; Sajavaara, T.; Nilsen, O.; Fjellvåg, H. *J. Mater. Chem.* **2009,** *19,* 8767–8771. doi:10.1039/b913466b
11. Larue, J. C. *Phys. Status Solidi A* **1971,** *6,* 143–151. doi:10.1002/pssa.2210060116
12. Wu, Y.; Döhler, D.; Barr, M.; Oks, E.; Wolf, M.; Santinacci, L.; Bachmann, J. *Nano Lett.* **2015,** *15,* 6379–6385. doi:10.1021/acs.nanolett.5b01424
13. Wietelmann, U.; Bauer, R. J. Lithium and Lithium Compounds. *Ullmann's Encyclopedia of Industrial Chemistry;* Wiley-VCH Verlag GmbH: Weinheim, Germany, 2000. doi:10.1002/14356007.a15_393
14. NIST. NIST Chemistry WebBook. https://webbook.nist.gov/ (accessed June 25, 2019).
15. Engbæk, J.; Nielsen, G.; Nielsen, J. H.; Chorkendorff, I. *Surf. Sci.* **2006,** *600,* 1468–1474. doi:10.1016/j.susc.2006.01.040
16. Tonks, J. P.; King, M. O.; Galloway, E. C.; Watts, J. F. *J. Nucl. Mater.* **2017,** *484,* 228–235. doi:10.1016/j.jnucmat.2016.12.008
17. NIST. NIST Lithium XPS data. https://srdata.nist.gov/xps/ (accessed June 25, 2019).
18. Zhuang, G.; Chen, Y.; Ross, P. N., Jr. *Surf. Sci.* **1998,** *418,* 139–149. doi:10.1016/s0039-6028(98)00710-9
19. *Avantage software 5.9904, XPS knowledge database;* ThermoFisher Scientific, 2018.
20. Crist, B. *Handbook of Monochromatic XPS Spectra;* Wiley: Weinheim, Germany, 1999.
21. Kanazawa, K. K.; Gordon, J. G. *Anal. Chem. (Washington, DC, U. S.)* **1985,** *57,* 1770–1771. doi:10.1021/ac00285a062
22. Tan, F.; Huang, X.-H. *Chin. Phys. Lett.* **2013,** *30,* 050701. doi:10.1088/0256-307x/30/5/050701
23. Oguchi, H.; Isobe, S.; Kuwano, H.; Shiraki, S.; Orimo, S.-i.; Hitosugi, T. *APL Mater.* **2015,** *3,* 096106. doi:10.1063/1.4931080

24. Thompson, G. B.; Allred, D. D. *J. X-Ray Sci. Technol.* **1997,** *7,* 159–170. doi:10.1006/jxra.1997.0258
25. Banger, S.; Nayak, V.; Verma, U. P. *J. Phys. Chem. Solids* **2018,** *115,* 6–17. doi:10.1016/j.jpcs.2017.11.027
26. Orimo, S.-i.; Nakamori, Y.; Eliseo, J. R.; Züttel, A.; Jensen, C. M. *Chem. Rev.* **2007,** *107,* 4111–4132. doi:10.1021/cr0501846
27. Sakintuna, B.; Lamari-Darkrim, F.; Hirscher, M. *Int. J. Hydrogen Energy* **2007,** *32,* 1121–1140. doi:10.1016/j.ijhydene.2006.11.022
28. Welch, F. H. *Nucl. Eng. Des.* **1974,** *26,* 444–460. doi:10.1016/0029-5493(74)90082-x

License and Terms